UNIVERSITY OF SOUTHAMPTON

SCHOOL OF CHEMISTRY

Investigation of chemisorption of oxygen on platinum nanoparticles with density functional theory calculations

by

Peter John Cherry

Thesis for the degree of Master of Philosophy

July 24, 2013

UNIVERSITY OF SOUTHAMPTON

SCHOOL OF CHEMISTRY

Master of Philosophy

Investigation of chemisorption of oxygen on platinum nanoparticles with density functional theory calculations by

Peter John Cherry

Abstract

Platinum nanoparticles are one of the most commonly used catalysts in proton exchange membrane fuel cells (PEMFCs). One of most important catalytic processes is the oxygen reduction reaction, and this is known to be affected by the size and structure of the platinum catalysts. Recent advances in the linear scaling DFT code ONETEP [1], have made it possible to investigate stages of the oxygen reduction reaction occuring on nanoparticles consisting of over a hundred atoms. In this thesis, these newly implemented techniques are tested and calibrated by comparing with similar calculations performed in plane-wave DFT code CASTEP [2]. Following this calibration, the chemisorption of atomic and molecular oxygen on different platinum structures was investigated through calculation of chemisorption energies, electron density differences, and local densities of states. Good qualitative agreement was found between the results obtained in this thesis, and those found in the available experimental and computational literature. Size effects, including variation in the strength of O-Pt binding, and the contraction of Pt-Pt bonds in smaller Pt_N and OPt_N nanoparticles relative to bulk, are observed and discussed with respect to their relevance to the oxygen reduction reaction.

Contents

List of Figures

List of Tables

Declaration of authorship

I, Peter John Cherry, declare that the thesis entitled “Investigation of chemisorption of oxygen on platinum nanoparticles with density functional theory calculations” and the work presented in the thesis are both my own, and have been generated by me as the result of my own original research. I confirm that:

- this work was done wholly or mainly while in candidature for a research degree at this University;
- where any part of this thesis has previously been submitted for a degree or any other qualification at this University or any other institution, this has been clearly stated;
- where I have consulted the published work of others, this is always clearly attributed;
- where I have quoted from the work of others, the source is always given. With the exception of such quotations, this thesis is entirely my own work;
- I have acknowledged all main sources of help;
- where the thesis is based on work done by myself jointly with others, I have made clear exactly what was done by others and what I have contributed myself.

Signed: . . . . . .

Date: . . . . . .

Acknowledgements

First I would like to thank my Supervisor, Dr. Chris-Kriton Skylaris, and my advisor, Professor Andrea Russell. I am also indebted to Dr. Misbah Sarwar, Dr. Glenn Jones, and Dr. David Thompsett, who have not only been a source of ideas and direction for the project, but also a source of motivation and encouragement. Professor John Dyke is deserving of many thanks for his help in the preparation and writing of this thesis. Alvaro, Chris, Stephen, Jacek, Karl, Max, Dr. Edmond Lee, Grant and Nawzat all have my gratitude for tolerating my presence in the office for the last 19 months. Finally, I would like to thank my family, without whose love and support this thesis would have not been possible.

None of this work would have been possible without the financial support of Johnson Matthey and the EPSRC, for which I am most grateful. I must also express my thanks to the isolutions team at Southampton, who have done an excellent job of maintaining and upgrading the computers and supercomputers necessary for this work to be completed.

Chapter 1

Introduction

A proton exchange membrane fuel cell (PEMFC) generates electrical energy through oxidation of hydrogen fuel. It is similar to a galvanic cell, with the exception that its reactants are supplied to it as fuel, rather than forming part of its construction[3]. The overall chemical reaction is:

$$2H_2 + O_2 \rightarrow 2H_2O. \tag{1.1}$$

In a PEMFC, this is separated into a reduction reaction occurring at the cathode, and an oxidation reaction occurring at the anode. The reaction occurring at the anode is the oxidation of hydrogen:

$$H_2 \rightarrow 2H^+ + 2e^-. \tag{1.2}$$

A rough schematic of a PEMFC is shown in Figure (1.1), below which the basic steps involved in its operation are outlined. There are many different ways of constructing the electrodes in a PEMFC [4]. This work focuses on the re-

actions occurring on the surface of platinum nanoparticles, supported on carbon electrodes. The support is often porous carbon black, but other carbon structures such as nanotubes and graphene have also been used [5]. A fuller discussion of possible kinds of carbon support can be found in reference [5]. The platinum nanoparticles are often bound to a carbon support using Nafion [6], but other materials such as polytetrafluoroethylene (Teflon [7]) are sometimes used. A more comprehensive discussion of electrode construction in PEMFCs can be found in reference [4].

The oxidation reaction at the anode occurs as follows:

$$\begin{aligned} 2Pt_s + H_2 &\rightarrow 2(Pt_s - H_{ads}) \\ (Pt_s - H_{ads}) &\rightarrow H^+ + e^- + Pt_s \end{aligned} \tag{1.3}$$

where Pt_s is a chemisorption site on the platinum catalyst, (Pt_s−H_{ads}) is atomic hydrogen chemisorbed on the platinum site. The basic mechanism of the reaction is as follows: On the platinum surface, the di-hydrogen molecule is split into two separate hydrogen atoms. These two hydrogen atoms will each be chemisorbed at different sites, Pt_s, on the platinum surface. The platinum-hydrogen bonds then break, and the hydrogen splits into ions and electrons. The hydrogen ions leave the platinum surface, and pass across the proton exchange membrane. The electrons transfer into the anode. This is typically a very fast reaction [8]. However, impurities in the hydrogen fuel may poison the platinum catalysts, and significantly reduce their effectiveness. Hydrogen fuel is often obtained by refining natural gas, and the refining process can fail to remove all the carbon monoxide. These CO molecules can bind to the surface of the platinum nanoparticle, reducing the number of available active sites [8].

The reaction which occurs at the cathode is the oxygen reduction reaction (ORR). This can occur by a number of different pathways. At low current densities, the oxygen reduction reaction is thought to occur by the following dissociative mechanism:

$$\begin{aligned} O_2 + 2Pt_s &\rightarrow 2(Pt_s - O_{ads}) \\ 2(Pt_s - O_{ads}) + 2H^+ + 2e^- &\rightarrow 2(Pt_s - OH_{ads}) \\ 2(Pt_s - OH_{ads}) + 2H^+ + 2e^- &\rightarrow 2H_2O + 2Pt_s \end{aligned} \tag{1.4}$$

$$\text{Net reaction: } O_2 + 4H^+ + 4e^- \rightarrow 2H_2O$$

An oxygen molecule is split into two atoms, each of which is chemisorbed on a separate site on the platinum catalyst. A hydrogen ion and an electron combine with a chemisorbed oxygen atom, resulting in a hydroxyl bonded to the Pt surface. A second hydrogen ion and electron combine with the chemisorbed hydroxyl to form H_2O, which then unbinds from the platinum surface.

The cell potential when there is no net current flow is called the equilibrium cell potential. It can be calculated from the reaction Gibbs free energy, $\Delta_r G$. If $\Delta_r G < 0$ the reaction is spontaneous, if $\Delta_r G > 0$ it is not. The equilibrium electrode potentials of the cathode, $\Delta U_{(0,c)}$, and anode, $\Delta U_{(0,a)}$, can be related to the reaction Gibbs free energy via [3]:

$$\Delta U_{(0,a)} = -\frac{\Delta_r G_a}{n_a F} \quad \text{and} \quad \Delta U_{(0,c)} = -\frac{\Delta_r G_c}{n_c F}. \tag{1.5}$$

Here, $\Delta_r G_a$ and $\Delta_r G_c$ are the reaction Gibbs free energies at the anode and cathode, n_a and n_c are the number of electrons involved in the reactions at the anode and cathode, and F is the Faraday constant. The total equilibrium cell potential, ΔU_0, is given by the difference between the reaction potentials at the two elec-

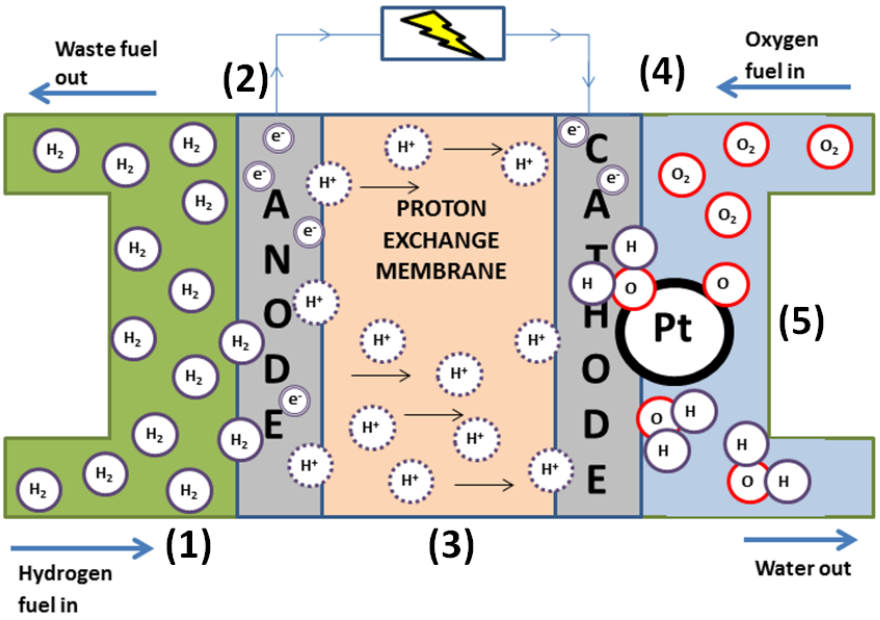

Figure 1.1: Schematic of a PEMFC. Its function can be summarized into the following steps. (1) Hydrogen fuel (H_2) comes in on the left and passes over the anode where it is ionized. (2) Electrons are drawn off round the top, and constitute the current which drives the load indicated by the lightning bolt in a box. (3) The hydrogen ions pass over the proton exchange membrane, usually made of Nafion [6], to the cathode. (4) On the right hand side the oxygen comes in. The O_2 molecules will be split, and individual oxygen atoms will be chemisorbed onto the surface of the Pt catalyst. (5) Hydrogen ions and electrons will then recombine with the oxygen on the surface of the platinum to form water, which will be drawn off as waste.

trodes [9], i.e.

$$\Delta U_0 = \Delta U_{(0,c)} - \Delta U_{(0,a)}. \tag{1.6}$$

The equilibrium cell potential for a hydrogen fuel cell operating at 25^{o}C is 1.229V [8]. However, experimental measurements can be >0.3V lower than this [10]. One cause of this is the oxidation of the platinum surface, which alters the electronic structure of the catalyst in a manner which reduces its efficiency [8]. Another problem is CO poisoning of the catalyst at the anode [10], which occurs due to impurities in the hydrogen fuel. The cell potential at non-zero current, ΔU_j, is

dependent on the net current density, j. The amount by which the cell potential varies is called the overpotential, η, and is defined by [3] [11]:

$$\eta = \Delta U_j - \Delta U_0 \tag{1.7}$$

The potential decreases with increasing current, and so the overpotential, η, is always negative. Roughly speaking, the overpotential is a measure of the amount of energy required to force the reaction to proceed at the rate required to obtain a current density, j. Finding catalysts and techniques which minimize the overpotential can help improve fuel cell efficiency.

It is desirable to have catalysts which maximize the number of electrons involved in the overall reactions. The greater the number of electrons involved in the reaction, the greater the associated current. An advantage of using platinum is that it catalyzes the 4-electron pathway for the ORR. Use of a carbon or other metal catalysts will cause other pathways, which involve fewer electrons to become more frequent [8]. This will result in a reduced current density, as well as production of hydrogen peroxide, which can damage the proton exchange membrane [9].

Accurate calculation of the current density, j, expected for a given system is beyond the reach of current computational techniques. However, a better understanding of the reactions outlined in equation (1.4) can help to inform experimental investigations and interpret experimental results. This report focuses on the ORR, as it is the rate limiting step [8]. For the ORR to occur on platinum by the 4-electron pathway outlined in equation (1.4), it is necessary that the platinum catalyst can split the oxygen molecule, i.e. it must be more energetically favorable for two oxygen atoms to bind to the platinum surface than it is for them to bind to one another on the surface. Chemisorption energies are difficult to measure

experimentally, so this is an area in which theoretical calculations are particularly valuable.

It is particularly important to understand how the oxygen binds to the platinum surface, as this is the first stage of the ORR as outlined in equation (1.4), and because both HO and CO bond to the platinum surface via the oxygen. This report focuses on the chemisorption energy of atomic oxygen on platinum. Consider the overall reaction:

$$\mathrm{Pt}_N + \mathrm{O}_2 \rightarrow \mathrm{OPt}_N\mathrm{O} \tag{1.8}$$

where $\mathrm{OPt}_N\mathrm{O}$ denotes adsorption of two oxygen atoms at two different sites on the surface of a platinum nanoparticle of N atoms. Calculation of the chemisorption energy requires three energies: 1) The energy, E_{Pt_N}, of the receptor (a Pt nanoparticle) 2) The energy, E_{O_2}, of the ligand (an O_2 triplet molecule) 3) The energy, E_{OPt_NO}, of the complex (2 oxygen atoms bound to the surface platinum nanoparticle). The chemisorption energy of molecular oxygen, $E_{(Mo.\ Oads)}$, is then calculated from:

$$2E_{(Mo.\ Oads)} = E_{OPt_NO} - E_{O_2} - E_{Pt}. \tag{1.9}$$

For technical reasons, it is often difficult to simulate multiple oxygen atoms chemisorbed on the same nanoparticle. Consequently, the following equation is often used in practice:

$$E_{(Mo.\ Oads)} \approx \frac{1}{2}(2E_{OPt_N} - E_{O_2} - 2E_{Pt}) = E_{OPt_N} - \frac{1}{2}E_{O_2} - E_{Pt_N}, \tag{1.10}$$

where E_{OPt_N} is the energy of a platinum nanoparticle with a single oxygen chemisorbed

upon it. The method summarized in eqn (1.10) is equivalent to assuming that the two oxygen atoms into which the molecular oxygen is split are chemisorbed on two different nanoparticles. A similar method is used to calculate the chemisorption energy of atomic oxygen, $E_{(At.\ Oads)}$:

$$E_{(At.\ Oads)} = E_{OPt_N} - E_O - E_{Pt_N}. \tag{1.11}$$

Understanding how the chemisorption energy of atomic oxygen varies with the size of the platinum nanoparticle could inform catalyst design. There is some disagreement in the literature as to the range over which size effects are most pronounced [12], but it is clear that they are prevalent in the <5nm range [9]. A possible cause of this is the greater number of undercoordinated sites on small nanoparticles [13]. The OH molecules can bind to these sites very strongly, making their removal difficult, and slowing this stage of the reaction [12]. However, this is at odds with the findings of Tian et al [14], who demonstrated the effectiveness of nanoparticle catalysts with a large number of stepped sites. Computational investigation of such surfaces could provide insight into the effect of surface morphology on binding energies.

A variety of different shapes of platinum catalysts have been tried [12]. Nanoparticles which are roughly spherical are found to be most stable [15], often resembling cuboctahedrons or isocahedrons. Such nanoparticles have facets resembling planes corresponding to planes with Miller indices (100) and (111). It has been shown experimentally that the active surface area of platinum nanoparticles is significantly lower than the total surface area [8]. This could be due to the platinum surface becoming less reactive when multiple oxygen atoms are chemisorbed upon it. Although high oxygen coverages have been investigated computationally

using semi-classical techniques [16], they have yet to be studied extensively using a first-principles approach. Examining the change in Pt-O binding energies at high oxygen coverages, and how this varies with particle size, may also shed light on the size dependence of the catalytic activity of platinum nanoparticles.

Apart from binding energies there are numerous other effects to consider, which may also help explain the correlation between catalytic activity and nanoparticle size. It is possible that the entire O_2 molecule may bind to the platinum. This can result in the formation of H_2O_2 instead of H_2O [8]. This is detrimental to the performance of a fuel cell, as if the ORR proceeds by the reaction pathway involving H_2O_2, only 2 (instead of 4) electrons are involved. Furthermore, H_2O_2 can damage the fuel cell membrane [9]. Examining the relevant binding energies at each of the stages of the ORR process may shed some light on the formation of H_2O_2, and how to prevent it. Computational investigation of why certain kinds of Pt catalyst seem particularly susceptible or resistant to poisoning from CO in the hydrogen fuel may also prove useful. It is possible to clean poisoned platinum nanoparticles by oxidizing the CO to form CO_2 [9]. An appropriate computational study could inform design of catalysts, and lead to catalysts which are easier to clean and are more resistant to poisoning.

One of the main barriers to extensive computational investigation is the size of the systems involved. A spherical platinum nanoparticle with a 3nm diameter is roughly 500 atoms large. To accurately describe the chemisorption of oxygen upon metal it is necessary to use a quantum mechanical approach. Density functional theory (DFT) calculations scale cubically with the size of the system [17]. Consequently, the simulation of systems of hundreds of atoms is usually computationally intractable. Furthermore, accurately describing metallic systems using

DFT is challenging, due to the degeneracy of molecular orbitals near the Fermi level. A consequence of this degeneracy is that thermal excitations can have a significant impact on the electronic structure. To account for the impact of these excitations the DFT code had to be extended to include effects of finite temperatures[1].

A method for performing finite temperature DFT has recently been implemented in ONETEP [1], a linear scaling DFT programme. This has made simulation of large metallic systems possible. In this report, this methodology is tested and calibrated for simulation of oxygen chemisorption on Pt_{13}. The validity of the method is tested by comparison with experimental measurements, and results obtained from similar calculations performed in CASTEP [2] on Pt_{13}, a cubic scaling DFT programme. Once tested and calibrated this method will be used to simulate oxygen chemisorbed on platinum nanoparticles of 13, 55 and 147 atoms ($\sim$0.5 nm, $\sim$1 nm and $\sim$1.6 nm in diameter respectively). These results will then be compared with results obtained in CASTEP simulations of atomic oxygen chemisorbed on extended platinum slabs, and the appearance of size effects will be commented upon.

[1] By another member of the Skylaris group; Alvaro Ruiz-Serrano.

Chapter 2

Aims

Finite temperature DFT is newly implemented, and must be extensively tested before it is used for practical calculations. To this end, ONETEP and CASTEP will both be used to simulate oxygen chemisorbed on Pt_{13}, and the results from these calculations will be compared.

Simulations of atomic oxygen chemisorbed at three different sites on infinite platinum slabs were performed in CASTEP. This served as a calibration study, in which some of the parameters to be used in future calculations were determined. It also provided chemisorption results with which later calculations of chemisorption of atomic oxygen on platinum would be compared. These results will be discussed and compared with computational and experimental studies in the literature.

ONETEP calculations have some input parameters not used in CASTEP calculations. Many of these parameters determine how the calculation is initialized, and the structure of the optimization procedure. To determine the appropriate ONETEP input parameters, ONETEP and CASTEP will be used to perform sim-

ulations of oxygen chemisorbed on Pt_{13}. The optimum ONETEP input parameters will be those which result in fast and stable convergence, whilst attaining strong agreement with the results obtained using CASTEP.

Once the implementation of the new methodology has been checked and the optimum input parameters have been identified, calculations of oxygen chemisorbed on cuboctahedral platinum nanoparticles of 13, 55 and 147 atoms will be performed. The chemisorption energy of atomic and molecular oxygen, the Pt-Pt and Pt-O bond lengths, and the Hirschfeld deformation densities will be calculated, and the variation in these quantities with nanoparticle size will be discussed.

Therefore, the aims of this work are as follows:

- Perform simulations of oxygen chemisorption at different sites on infinite Pt (111) slabs in CASTEP.
- Use ONETEP and CASTEP to simulate atomic oxygen chemisorbed upon a Pt_{13} cuboctahedral nanoparticle.
- Identify optimum ONETEP calculation parameters.
- Simulate atomic oxygen chemisorbed on Pt_{55} and Pt_{147} using ONETEP.
- Compare results of the calculations on nanoparticles and slabs with results found in the literature, and comment on the strength of agreement and the occurrence of size effects.

Chapter 3

Theoretical background and computational techniques

3.1 Quantum mechanics

3.1.1 Wavefunctions and the Schrödinger equation

To accurately describe microscopic particles it is necessary to use quantum mechanics. A key feature of quantum mechanics is wave-particle duality; particles may exhibit wave-like behavior, whilst waves might exhibit particle-like behavior. The wavelength, λ, that corresponds to a given particle is called the de Broglie wavelength. It is given by:

$$\lambda = \frac{h}{p} = \frac{h}{\sqrt{2Em}}. \tag{3.1}$$

Here, h is Planck's constant, E is the kinetic energy of the particle, m is the mass of the particle, and p is the momentum of the particle.

In quantum mechanics, every physical system, be it a single particle or a collection of particles, may be described by a wavefunction, $\Psi(\{\mathbf{r}\}, \{s\}, t)$. Here, $\{\mathbf{r}\}$ are the positions of the particles, $\{s\}$ are the spins of these particles, and t is the time. All physical observables associated with the system can be calculated by acting on the wavefunction with an operator. For example, a physical observable corresponding to a variable o, can be calculated for the system represented by the wavefunction $\Psi(\{\mathbf{r}\}, \{s\}, t)$, by acting on $\Psi(\{\mathbf{r}\}, \{s\}, t)$ with the operator, $\hat{O}$:

$$\hat{O}\Psi(\{\mathbf{r}\}, \{s\}, t) = o\Psi(\{\mathbf{r}\}, \{s\}, t). \tag{3.2}$$

Here, $\Psi(\{\mathbf{r}\}, \{s\}, t)$ is said to be an eigenfunction of $\hat{O}$, and o is the corresponding eigenvalue. The eigenvalues of a physical operator must be real, as physical variables do not have imaginary components. A consequence of this is that all physical operators must possess a mathematical property known as Hermiticity [18].

In quantum mechanics, Bra $\langle\Psi|$, -Ket $|\Psi\rangle$, notation is often used to represent physical states. The closure of the Bra-Ket; $\langle\Psi|\Psi\rangle$, indicates the inner product. A state, $|\Psi\rangle$, is said to be normalized if

$$\langle\Psi|\Psi\rangle = \int \Psi^*(\mathbf{r}, s, t)\Psi(\mathbf{r}, s, t)d\mathbf{r}\, ds\, dt\, = 1. \tag{3.3}$$

Two different states; $|\Psi_i\rangle$ and $|\Psi_j\rangle$ are orthogonal if

$$\langle\Psi_i|\Psi_j\rangle = A\delta_{ij}, \tag{3.4}$$

where δ_{ij} is the Kronecker delta function and A is some real constant. If $A = 1$, then the states are said to be orthonormal.

One of the postulates of quantum mechanics is that the mean value of measurements of o, will be equal to the expectation value, $\langle\hat{O}\rangle$, of the operator $\hat{O}$. The expectation value is defined to be [19]:

$$\langle\hat{O}\rangle = \frac{\langle\Psi|\hat{O}|\Psi\rangle}{\langle\Psi|\Psi\rangle}. \tag{3.5}$$

One of the most important equations in quantum mechanics is the Schrödinger equation [18]:

$$i\hbar\frac{\partial}{\partial t}\Psi(\{\mathbf{r}\},t) = \left(\frac{-\hbar^2}{2m}\nabla^2 + V(\mathbf{r},t)\right)\Psi(\{\mathbf{r}\},t) = (\hat{T}+\hat{V})\Psi(\{\mathbf{r}\},t) = \hat{H}\Psi(\{\mathbf{r}\},t), \tag{3.6}$$

where $\hbar = \frac{h}{2\pi}$, with h the Planck constant. ∇^2 is the square of the spatial differential operator, i.e. $\hat{\nabla}^2 = \left(\frac{\partial}{\partial x}\right)^2 + \left(\frac{\partial}{\partial y}\right)^2 + \left(\frac{\partial}{\partial z}\right)^2$. m is the mass of the particle, $V(\mathbf{r},t)$ is an external potential. $\hat{H}$, is the Hamiltonian operator; it is used to find the energy of the wavefunction. It can be split into two components: $\hat{V}$; the potential operator, and $\hat{T}$; the kinetic energy operator.

In many cases, the potential is either constant, or varies slowly with time, i.e. $V(\mathbf{r},t) = V(\mathbf{r})$. In such cases, the solutions to the Schrödinger equation will be of form [20]:

$$\Psi_n(\{\mathbf{r}\},t), = \exp\frac{iE_nt}{\hbar}\phi_n(\{\mathbf{r}\}), \tag{3.7}$$

where $\phi_n(\{\mathbf{r}\})$ are the solutions to the time-independent Schrödinger equation [20]:

$$E_n\phi_n(\{\mathbf{r}\}) = \left(\frac{-\hbar^2}{2m}\nabla^2 + V(\mathbf{r})\right)\phi_n(\{\mathbf{r}\}) = \hat{H}_{TI}\phi_n(\{\mathbf{r}\}), \tag{3.8}$$

and E_n is the energy of the nth eigenstate, $\phi_n(\{\mathbf{r}\})$, of the time-independent Hamiltonian, $\hat{H}_{TI}$. E_0 is the energy of the ground state, $\phi_0(\{\mathbf{r}\})$. These time-independent states are often referred to as stationary states.

3.1.2 Molecular wavefunctions and the Born-Oppenheimer approximation

The form of the time-independent Schrödinger equation for a molecular wavefunction is:

$$(\hat{T} + \hat{U}_{(e-e)} + \hat{U}_{(e-n)} + \hat{U}_{(n-n)})|\Psi_n\rangle = E_n|\Psi_n\rangle. \tag{3.9}$$

Here, E_n is the energy of the state, $|\Psi_n\rangle$, and $\{\mathbf{r}\}$ and $\{\mathbf{R}\}$ are coordinates of the electrons and nuclei. $\hat{T}$ is the non-relativistic kinetic energy operator given by

$$\hat{T} = \hat{T}_{elec} + \hat{T}_{nuc} = \sum_{i}^{N_e} \frac{-\hbar^2 \hat{\nabla}^2_{\mathbf{r}_i}}{2m_e} + \sum_{J}^{N_{nuc}} \frac{-\hbar^2 \hat{\nabla}^2_{\mathbf{R}_J}}{2m_{nuc}}. \tag{3.10}$$

m_e and m_{nuc} are the electron and nuclear masses, respectively. N_e and N_{nuc} are the number of nuclei and electrons in the system. $\hat{U}_{(e-e)}$ is the classical electron-electron interaction potential, and is given by

$$\hat{U}_{(e-e)} = \sum_{j}^{N_e} \sum_{i<j}^{N_e} \frac{e^2}{4\pi\epsilon_0 |\mathbf{r}_i - \mathbf{r}_j|}, \tag{3.11}$$

where e is the electron charge, $\mathbf{r}_i$ and $\mathbf{r}_j$ are the positions of the ith and jth electrons, and ϵ_0 is the vacuum permittivity. $\hat{U}_{(e-n)}$ is the electron-nuclear interaction

potential given by

$$\hat{U}_{(e-n)} = -\sum_{I}^{N_{nuc}} \sum_{j}^{N_{elec}} \frac{e^2 Z_I}{4\pi\epsilon_0 |\mathbf{R}_I - \mathbf{r}_j|}. \tag{3.12}$$

Here, Z_I is the atomic number of the Ith nucleus, and $\mathbf{R}_I$ is the position of the Ith nucleus. $\hat{U}_{(n-n)}$ is the nuclear-nuclear interaction potential given by

$$\hat{U}_{(n-n)} = \sum_{J}^{N_n} \sum_{I<J}^{N_n} \frac{e^2 Z_I Z_J}{4\pi\epsilon_0 |\mathbf{R}_I - \mathbf{R}_J|}. \tag{3.13}$$

The mass of the nuclei is much greater than that of the electrons, hence the nuclei will be moving much more slowly. It can be shown that it is possible to separate the wavefunction $\Psi(\{\mathbf{r}\}, \{\mathbf{R}\})$ into an electronic, $\varphi(\{\mathbf{r}\}; \{\mathbf{R}\})$, and nuclear, $\Theta(\{\mathbf{R}\})$, component:

$$\Psi(\{\mathbf{r}\}, \{\mathbf{R}\}) = \Theta(\{\mathbf{R}\})\varphi(\{\mathbf{r}\}; \{\mathbf{R}\}). \tag{3.14}$$

This is known as the Born-Oppenheimer approximation. It should be noted that the electronic component still depends parametrically on the nuclear positions. These two components can be found by solving two separate Schrödinger equations. The Schrödinger equation which must be solved to find the electronic component $\varphi(\{\mathbf{r}\}; \{\mathbf{R}\})$ is [21]:

$$E_e \varphi(\{\mathbf{r}\}; \{\mathbf{R}\}) = \tag{3.15}$$
$$\left[\sum_{i}^{N_e} \frac{-\hbar^2 \nabla^2_{\mathbf{r}_i}}{2m_e} + \sum_{j} \sum_{i<j}^{N_e} \frac{e^2}{4\pi\epsilon_0 |\mathbf{r}_i - \mathbf{r}_j|} + \sum_{I,j} \frac{e^2 Z_i}{4\pi\epsilon_0 |\mathbf{R}_I - \mathbf{r}_j|} \right] \varphi(\{\mathbf{r}\}; \{\mathbf{R}\}).$$

Here, E_e is the energy eigenvalue associated with the electronic component, $\varphi(\{\mathbf{r}\}; \{\mathbf{R}\})$,

of the wavefunction. The above equation is referred to as the electronic Schrödinger equation. In the solution of this equation, the nuclear positions are assumed to be fixed. The total energy of the nuclear wavefunction $\Theta(\mathbf{R})$, can then be calculated from [21]:

$$E_{B.O.}\Theta(\{\mathbf{R}\}) = \left(\sum_{J}^{N_{nuc}} \frac{-\hbar^2 \nabla^2_{\mathbf{R}_J}}{2m_{nuc}} + \sum_{J} \sum_{I<J}^{N_n} \frac{e^2 Z_I Z_J}{4\pi\epsilon_0 |\mathbf{R}_I - \mathbf{R}_J|} + E_e \right) \Theta(\mathbf{R}). \tag{3.16}$$

Here $E_{B.O.}$ is the total energy, the subscript is to indicate use of the Born-Oppenheimer approximation.

3.1.3 Electron density

Often it is convenient to represent a many electron wavefunction in terms of the charge density, $n(\mathbf{r})$, associated with that wavefunction. The single particle density matrix[1], $\rho(\mathbf{r}, \mathbf{r}')$, associated with an N-electron wavefunction, $\Psi(\mathbf{r}_1, .., \mathbf{r}_N)$, is defined by [22]

$$\rho(\mathbf{r}_1, \mathbf{r}'_1) = N_e \int \Psi(\mathbf{r}_1 \mathbf{r}_2 .... \mathbf{r}_N) \Psi^*(\mathbf{r}'_1 \mathbf{r}_2 .... \mathbf{r}_N) d\mathbf{r}_2 ... d\mathbf{r}_N. \tag{3.17}$$

The electron density, $n(\mathbf{r})$, is defined as the trace of the single particle density matrix [22]

$$n(\mathbf{r}_1) = \rho(\mathbf{r}_1, \mathbf{r}_1) = N_e \int \Psi(\mathbf{r}_1 \mathbf{r}_2 .... \mathbf{r}_N) \Psi^*(\mathbf{r}_1 \mathbf{r}_2 .... \mathbf{r}_N) d\mathbf{r}_2 ... d\mathbf{r}_N, \tag{3.18}$$

where N is the number of electrons. The charge density depends on only one variable, $\mathbf{r}_1$, regardless of how many electrons are in the original wavefunction.

[1] Spin has been neglected, and will be used from now on.

The requirement that a charge density corresponds to an N-electron wavefunction is known as the requirement of N-representability. The constraints which must be satisfied to ensure N-representability are [22]

$$n(\mathbf{r}) \geq 0, \int n(\mathbf{r})d\mathbf{r} = N_e \text{ and } \int |\nabla n(\mathbf{r})^{\frac{1}{2}}|^2 d\mathbf{r} = N_e. \tag{3.19}$$

A density which satisfies these constraints is said to be 'well-behaved'.

3.2 Density Functional Theory

3.2.1 The Hohenberg-Kohn theorems

In density functional theory (DFT), it is the charge density, $n(\mathbf{r})$, and not the N-electron wavefunction, which is used to describe the system. The main motivation for this is that $n(\mathbf{r})$, depends on 3 variables[2], whilst $\Psi(\mathbf{r}_1, .., \mathbf{r}_N)$ depends on $3N$ variables. The Hohenberg-Kohn existence theorem states that the electron density uniquely determines an N-electron wavefunction; this guarantees that the ground state density uniquely determines all the properties of the ground state of the system. To prove this, it is sufficient to show that the density uniquely determines the Hamiltonian of the system. This can be achieved by demonstrating the impossibility of two different Hamiltonians corresponding to the same density.

Consider two Hamiltonians, $\hat{H}$ and $\hat{H}'$, which differ only by the potential term, $v(\mathbf{r})$ and $v'(\mathbf{r})$. Suppose both these Hamiltonians correspond to the same ground-state density, $n_0(\mathbf{r})$. If this is true, then there are two different wavefunctions, $\Psi(\mathbf{r})$ and $\Psi'(\mathbf{r})$, which correspond to the same density, $n_0(\mathbf{r})$. If it is assumed the

[2] $\mathbf{r}$ is a position vector in physical space.

system is non-degenerate, then one of these wavefunctions, say $\Psi(\mathbf{r})$, will be the ground state, whilst the other, $\Psi'(\mathbf{r})$, must, according to the variational theorem, correspond to a state of higher energy, say ϵ_0'. This would imply that [22]:

$$\epsilon_0 < \langle\Psi'|\hat{H}'|\Psi'\rangle + \langle\Psi'|\hat{H} - \hat{H}'|\Psi'\rangle = \epsilon_0' + \int n(\mathbf{r})[v(\mathbf{r}) - v'(\mathbf{r})]d\mathbf{r}, \quad (3.20)$$

but this also implies that [22]:

$$\epsilon_0' < \langle\Psi|\hat{H}|\Psi\rangle + \langle\Psi|\hat{H}' - \hat{H}|\Psi\rangle = \epsilon_0 + \int n(\mathbf{r})[v'(\mathbf{r}) - v(\mathbf{r})]d\mathbf{r}. \quad (3.21)$$

These two equations may be summed to obtain the false statement:

$$\epsilon_0 + \epsilon_0' < \epsilon_0' + \epsilon_0. \quad (3.22)$$

Therefore, each ground state density, $n_0(\mathbf{r})$, uniquely determines a Hamiltonian, and hence uniquely determines the energy of the system.

Computational methods to calculate the charge density, $n(\mathbf{r})$, usually make use of the 2nd Hohenberg-Kohn theorem; the Hohenberg-Kohn variational principle. The standard variational principle states that for some trial wavefunction, $\Psi_{trial}(\mathbf{r})$ [20],

$$\langle\Psi_{trial}|\hat{H}|\Psi_{trial}\rangle \geq E_0, \quad (3.23)$$

where E_0 is the ground state energy and $\hat{H}$ is the exact Hamiltonian of the system. Therefore, if $n_0(\mathbf{r})$ uniquely determines a Hamiltonian, $\hat{H}$, then it must also uniquely determine the ground state wavefunction, $\Psi_0(\mathbf{r})$. It may be shown that

[23], two functionals, $E_v[n]$ and $F[n]$, may be defined such that

$$E_v[n] = F[n] + \int n(\mathbf{r})v(\mathbf{r})d\mathbf{r} = \langle\Psi|\hat{H}|\Psi\rangle = E. \tag{3.24}$$

Furthermore, $E_v[n]$ and $F[n]$ will satisfy

$$E[n_{guess}] \geq E[n_0] = E_0. \quad \text{and} \quad F[n_{guess}] \geq F[n_0] = F_0. \tag{3.25}$$

Here n_{guess} is some well-behaved charge density. This is referred to as the Hohenberg-Kohn variational theorem [22]. It is very useful, as it means that the ground state density, $n_0(\mathbf{r})$, will minimize the functional $E[n]$, subject to the constraint of conservation of the number of electrons. Finding the density which satisfies the above equation plays a central role in many computational implementations of DFT. The functional $F[n]$ is universal [22], i.e. it has the same form for all charge densities. Unfortunately, the exact form of $F[n]$ remains unknown.

3.2.2 Kohn-Sham Theory

One of the reasons DFT is widely used is that it enables us to avoid direct calculation of an N-electron wavefunction. There are a number of different formulations of DFT. This report focuses on the extension to orbital free DFT developed by Kohn and Sham [24], hereafter referred to as Kohn-Sham DFT or KS-DFT.

Consider a charge density, $n(\mathbf{r})$, which corresponds to some N-particle wavefunction. The insight of Kohn-Sham DFT is that there will be a system of N, non-interacting electrons, which corresponds to the same charge density $n(\mathbf{r})$. Each of the electrons in the non-interacting system will be described by a single particle

molecular orbital wavefunction $\psi_i(\mathbf{r})$. The charge density $n(\mathbf{r})$ can be calculated from these single particle wavefunctions:

$$n(\mathbf{r}) = \sum_{i}^{N} f_i \psi_i^*(\mathbf{r}) \psi_i(\mathbf{r}). \tag{3.26}$$

The corresponding single particle density matrix operator, $\hat{\rho}$, is [22]:

$$\hat{\rho} = \sum_{i}^{N} f_i |\psi_i\rangle\langle\psi_i|, \tag{3.27}$$

which may be spatially represented as [22]:

$$\rho(\mathbf{r}', \mathbf{r}) = \sum_{i}^{N} f_i \psi_i(\mathbf{r}') \psi_i^*(\mathbf{r}). \tag{3.28}$$

Here, f_i is the occupancy of the molecular orbital $\psi_i(\mathbf{r})$. What makes this insight remarkable is that the non-interacting system is a fictitious mathematical construction, but it can still be used to obtain all the properties of the ground state of the system. An important constraint placed upon these orbitals is that they are normalized and orthogonal to one another, i.e.

$$\langle\psi_i|\psi_j\rangle = \delta_{ij}. \tag{3.29}$$

The Hamiltonian for the non-interacting system can be expressed as a sum of single particle operators, and will be much less complicated than the Hamiltonian for the interacting system. The total energy, $E[n]$, of the non-interacting system can then be written, as:

$$E[n] = T_{ni}[n] + V_{ne}[n] + U_H[n] + E_{xc}[n] =$$

$$\sum_{i}^{N_e}\left(\langle\psi_i|-\frac{1}{2}\nabla^2|\psi_i\rangle-\langle\psi_i|\sum_{j}^{N_{nuc}}\frac{Z_j}{|\mathbf{r}_i-\mathbf{r}_i|}|\psi_i\rangle\right)+\sum_{i}^{N}\langle\psi_i|\frac{1}{2}\int\frac{n(\mathbf{r})}{|\mathbf{r}-\mathbf{r}'|}d\mathbf{r}'|\psi_i\rangle+E_{xc}[n], \tag{3.30}$$

where atomic units have been used in the above, and will be from now on in this thesis. $T_{ni}[n]$ is the kinetic energy for the non-interacting system, and $V_{ne}[n]$ is the contribution to the energy from the nuclear-electron interaction in the non-interacting system. $U_H[n]$ is the Coulomb energy of the non-interacting system. $E_{xc}[n]$ is the exchange-correlation term, which is accounts for the exchange and correlation effects, as well as all the complexities which arise due to the approximation of the interacting system with a non-interacting one (such as corrections to the kinetic energy and additional electron-electron interaction terms).

Instead of attempting to find the charge density directly, it is possible to instead focus on finding the orbitals, $\psi_i(\mathbf{r})$. These orbitals will satisfy the equation [17]

$$\hat{h}_i^{KS}|\psi_i\rangle=\epsilon_i|\psi_i\rangle, \tag{3.31}$$

where the Kohn-Sham one-electron Hamiltonian, $\hat{h}_i^{KS}$, is defined as

$$\hat{h}_i^{KS}=-\frac{1}{2}\hat{\nabla}_i^2-\sum_{j}^{N_{nuc}}\frac{Z_j}{|\mathbf{R}_j-\mathbf{r}_i|}+\frac{1}{2}\int\frac{n(\mathbf{r})}{|\mathbf{r}_i-\mathbf{r}|}d\mathbf{r}+\hat{V}_{xc}. \tag{3.32}$$

Here, $\hat{V}_{xc}$ is the exchange correlation potential. The exchange correlation potential functional, $\hat{V}_{xc}[n]$, can be related to the exchange correlation energy by [17]

$$V_{xc}[n]=\frac{\delta E_{xc}[n]}{\delta n}. \tag{3.33}$$

It should be noted that this is not a normal derivative but a functional derivative, a fuller discussion of which can be found in [22]. By making use of the Hohenberg-

Kohn variational principle it is possible to calculate the ground state density by finding the set $\{\psi_i(\mathbf{r}_i)\}$ of non-interacting orbitals which correspond to the density, $n(\mathbf{r})$, which minimizes the energy defined in equation (3.30)[17].

3.2.3 Mermin's extension of orbital free DFT to finite temperatures

A finite temperature formulation of DFT was developed by Mermin in 1965 [25]. The proof of the Hohenberg-Kohn existence theorem given in section 3.2.1 depends on the fact that the energy functional, $E[n]$, is of form

$$E[n] = \int v(\mathbf{r})n(\mathbf{r})d\mathbf{r} + X[n]. \tag{3.34}$$

Here, $v(\mathbf{r})$ is the external potential, whilst $X[n]$ is a functional which accounts for all other contributions to the energy. To extend DFT to finite temperatures it is necessary to show that there exists a universal functional, $F[n]$, such that:

$$\Omega[n] = \int v(\mathbf{r})n(\mathbf{r})d\mathbf{r} + F[n]. \tag{3.35}$$

Here $\Omega[n]$ determines the free energy, and is minimized and equal to the grand potential when $n(\mathbf{r})$ is equal to the equilibrium ground state density in the presence of an external potential, $v(\mathbf{r})$. To satisfy this criterion it is necessary that $F[n]$ be independent of the external potential, $v(\mathbf{r})$. It is also necessary that $F[n]$ accounts for all the entropic contributions to the energy. An expression for $F[n]$ can be found in reference [22].

It is shown in reference [25] that it is possible to derive a finite temperature equiv-

alent of the Hohenberg-Kohn variational principle:

$$\Omega[n] \geq \Omega[n_0]. \tag{3.36}$$

From this is it possible to show that the external potential, $v(\mathbf{r})$, is uniquely determined by the ground state density [25]. It is also possible to derive a Kohn-Sham formulation of finite temperature DFT [22].

3.2.4 Exchange-correlation functionals

The exchange-correlation functional (xc-functional) must account for all contributions to the energy not accounted for by the first three terms in equation (3.30). One cause of these extra contributions are the properties of electron wavefunctions which are not apparent from the electron density. Electrons are also indistinguishable from one another. Electrons also have a spin of $\frac{1}{2}$, therefore, they are Fermions [18]. One consequence of this is that electron wavefunctions are anti-symmetric under interchange of particle position and spin. Contributions to the energy arising from this antisymmetry requirement are referred to as exchange effects [26].

There are numerous other quantum mechanical effects associated with electron interactions which must be accounted for by the xc-functional. These include correlation effects, removal of the self-interaction contributions, and the difference in the kinetic energy between the interacting and non-interacting system [26].

The exact form of the xc-functional, $E_{xc}[n]$, is not known. Even determining an approximate form is very challenging, and attempts to do so depend on a mix of theoretical analysis and numerical fitting. There are two main kinds of xc-

functionals; local density approximation (LDA) and generalized gradient approximation (GGA).

An LDA xc-functional is calculated from the value of the charge density at every point in the distribution, but ignores the spatial gradient of the charge density. An LDA functional, $E_{xc}^{LDA}[n]$, is of form [17]:

$$E_{xc}^{LDA}[n] = \int n(\mathbf{r})\epsilon_{xc}^{LDA}(n(\mathbf{r}))d\mathbf{r} \tag{3.37}$$

Here, $\epsilon_{xc}^{LDA}(n(\mathbf{r}))$, is the exchange-correlation energy density, which is a function of the charge density at a given point. $\epsilon_{xc}(n(\mathbf{r}))$ is usually split into exchange and correlation components, i.e. $\epsilon_{xc}(n(\mathbf{r})) = \epsilon_x(n(\mathbf{r})) + \epsilon_c(n(\mathbf{r}))$. There is an analytic expression for the exchange component [27]:

$$\epsilon_x(n(\mathbf{r})) = -\frac{3}{4}\left(\frac{3}{\pi}\right)^{\frac{1}{3}} n(\mathbf{r}). \tag{3.38}$$

The correlation component, $\epsilon_c(n(\mathbf{r}))$, must be determined using numerical methods, and a variety of different approaches exist [28][29][30][31].

A GGA based xc-functional is similar to an LDA functional, but with additional terms which are dependent upon the spatial gradient of $n(\mathbf{r})$. A GGA xc-functional, $E_{xc}^{GGA}[n]$, has the form:

$$E_{xc}^{GGA}[n] = \int n(\mathbf{r})\epsilon_{xc}^{GGA}(n(\mathbf{r}), \nabla n(\mathbf{r}))d\mathbf{r}. \tag{3.39}$$

Here, $\epsilon_{xc}^{GGA}(n, \nabla n)$, is the exchange correlation energy density, which is a function of the charge density, and the spatial gradient of the density. In the vast majority of cases, GGA functionals are more accurate [32]. Changing the xc-functional can

have a significant effect on the results of a calculation, and selecting an appropriate one is important.

Two xc-functionals were considered in this work; the Perdew-Wang 1991 functional (PW91) [33], and a revised version of the Perdew, Burke and Ernzerhof functional (RPBE) [34]. These were selected largely due to their predominance in the literature. Both functionals are based on the first principles generalized gradient approximation (GGA). LDA functionals have been shown to be poor at capturing the behavior of systems with delocalized electrons (such as metals) [35], and so were not used for the calculations discussed in this report.

There are many other kinds of functionals not mentioned here. Hybrid functionals incorporate a component of exact exchange, which is calculated directly from the Kohn-Sham orbitals (as opposed to from the density). One of the most well known examples of a hybrid functional is the B3-LYP (Becke, 3-parameter-Lee-Yang-Parr) [36]. There are also meta-hybrid GGA functionals, details of which can be found in references [37] and [38].

Perdew-Wang 1991 functional

The PW91 xc-functional was derived by consideration of a system of slowly varying electron density. In essence, it is a numerical fit to a second order expansion of the density-gradient for the exchange-correlation hole for such a system. One of the main drawbacks of PW91 is the complexity of the mathematical form of the functional; whilst it provides a good numerical fit, it cannot be decomposed into separate parts, each of which correspond to a specific aspect of the physical interactions being modelled. Not only does this make the functional hard to interpret, but means that simple phenomena, such as the response to perturbation of

a linear electron gas, are actually better modelled by more primitive LSD (Local Spin Density) based functionals which make larger approximations [35].

Nonetheless, there are a wealth of results obtained from use of the PW91 functional, making it a good choice for performing calibration studies. The mathematical expression for the PW91 can be found in [33].

Revised Perdew, Burke and Ernzerhof functional

In reference [35] Perdew, Burke and Ernzerhof derived a GGA functional intended to be the successor to the PW91 functional. The PBE functional was then revised by Hammer, Hansen and Nørskov to obtain the RPBE functional [34] . An advantage of the RPBE functional is that, unlike the PW91 functional, it always satisfies the Lieb-Oxford criterion (a lower bound on the exchange-correlation energy [39]).

3.2.5 Basis Sets

A wavefunction, $\psi_j(\mathbf{r})$, can be expressed as a linear combination of other functions:

$$\psi_j(\mathbf{r}) = \sum_{\alpha}^{N_{basis}} \chi_\alpha(\mathbf{r}) M_j^\alpha. \tag{3.40}$$

The set of functions, $\{\chi_\alpha(\mathbf{r})\}$, in terms of which $\psi_j(\mathbf{r})$ is described is called the basis set. N_{basis} is the number of functions in the basis set. The set of coefficients $\{M_j^\alpha\}$ define $\psi_j(\mathbf{r})$ in this basis set. The expression for the density can now be

written as:

$$n(\mathbf{r}) = \sum_{j}^{N_{orb}} f_j \psi_j(\mathbf{r}) \psi_j^*(\mathbf{r}) = \sum_{j}^{N_{orb}} \sum_{\beta}^{N_{basis}} \sum_{\alpha}^{N_{basis}} \chi_\alpha(\mathbf{r}) M_j^\alpha M_j^{\dagger\beta} \chi_\beta(\mathbf{r}). \tag{3.41}$$

Here, N_{orb} is the number of orbitals, $\psi_j(\mathbf{r})$. Plane waves are often used as the basis set. To be able to perfectly describe any $\psi_j(\mathbf{r})$, the basis set would need to be infinitely large. Computational cost scales cubically with the size of the basis set, so a finite basis set must be used. The two key factors which affect the accuracy of the description of the system in this basis set are i) The size of the basis set, i.e. the number of $\chi_\alpha(\mathbf{r})$ in the set, and ii) How suitable the functions in the basis set are for describing the system (e.g. do they share the same limiting behavior, such as vanishing when $r \to \infty$).

Plane waves are suitable for describing wavefunctions associated with periodic systems (consider Bloch's theorem [40]), and so are well suited for large crystalline structures. CASTEP uses a plane wave basis set, with $\psi_{j\mathbf{k}}(\mathbf{r})$ expressed in a form similar to:

$$\psi_{j\mathbf{k}}(\mathbf{r}) = \sum_{|\mathbf{G}|=0}^{|\mathbf{G}_{max}|} c_{\mathbf{k}}(\mathbf{G}) e^{-i(\mathbf{k}+\mathbf{G})\cdot\mathbf{r}}. \tag{3.42}$$

Here, $\{c_{j\mathbf{k}}(\mathbf{G})\}$ are the set of coefficients which represent $\psi_{j\mathbf{k}}(\mathbf{r})$ in the plane-wave basis, $\mathbf{k}$ is a point in the Brillouin zone, $|\mathbf{G}_{max}|$ the wavevector cut-off, and $\mathbf{G}$ is the wave vector. The size of the basis is determined by the value of $|(\mathbf{k}+\mathbf{G})|$, which is related to the energy of a wave in the basis set by

$$E = \frac{\hbar^2 |\mathbf{k}+\mathbf{G}|^2}{2m}, \tag{3.43}$$

where m is the mass of the particle in question. Therefore, setting the value of $|\mathbf{G}_{max}|$ is equivalent to setting the maximum energy, E_{max}, of the plane waves

included in the basis set. Increasing E_{max} increases the number of functions in the basis set, and hence the descriptive power of the basis set. In effect, this makes it possible to control the accuracy of a calculation through variation of a single parameter. This parameter, E_{max}, is often referred to as the kinetic energy cut-off or KE cut-off.

The Kohn-Sham orbitals are eigenvectors of the Kohn-Sham Hamiltonian. This means that when the Hamiltonian and the Kohn-Sham orbitals are represented in the same space, the matrix of coefficients, $M_{\alpha i}$, which represent the Kohn-Sham orbitals will form a unitary rotation which diagonalizes the Hamiltonian, i.e.

$$H^{\alpha\beta} = \sum_{i}^{N_{orbs}} M_i^{\alpha} \epsilon_i M_i^{\beta} \quad \text{and} \quad \sum_{\alpha,\beta}^{N_{basis}} M_i^{\alpha} H_{\alpha\beta} M_i^{\beta} = \epsilon_i. \tag{3.44}$$

Here, $H^{\alpha\beta}$ is the Kohn-Sham Hamiltonian defined in the space of $\{\chi_\alpha(\mathbf{r})\}$. It is possible to determine the Kohn-Sham orbitals by finding the matrix, with elements M_i^{α}, which diagonalizes the Hamiltonian. The computational cost of diagonalizing a dense matrix scales cubically with the dimensionality of the matrix [17]. Full diagonalization of the Hamiltonian can be avoided by use of one of a number of more computationally efficient methods (please see reference [41] for a summary). However, even if full diagonalization is avoided, the Kohn-Sham orbitals are still required to be orthogonal to to one another. Orthogonalization of the Kohn-Sham orbitals is a cubic scaling process, hence so too are most computational implementations of DFT [17].

3.2.6 Pseudo-potentials

The electrons close to the core of the atom (hereafter referred to as core electrons) play a relatively small role in chemical bonding [42]. The interactions between the core electrons and the valence electrons can be adequately described using a fixed potential. This is called the pseudo-potential approximation. The radius within which all electrons are defined as core electrons is called the pseudo-potential core radius. Orbitals calculated using the pseudo-potential approximation are referred to as pseudo-orbitals.

Making the pseudo-potential approximation greatly reduces the dimensionality of the problem; instead of having N KS-orbitals (where N is the number of electrons in the system), there are $(N - N_{core})$ KS-orbitals, where N_{core} is the number of core-electrons. Given that the computational cost of multiplication of dense matrices scales cubically with the dimensionality of the matrices (which is linearly proportional to the number of KS-orbitals), this is a particularly worthwhile saving.

Many different types of pseudo-potential exist. The pseudo-potentials discussed here are norm-conserving pseudo-potentials, and meet the following requirements [43]:

1) Outside the cut-off radius, the pseudo-orbital and orbital should be equal.
2) The eigenvalues of the pseudo-orbital and orbital should be equal.
3) There must be no discontinuity at the cut-off radius, either in the pseudo-orbital or its first or second order derivatives.
4) The pseudo-orbitals must not have any nodes inside the cut-off radius.

Inside the cut-off radius the pseudo-orbitals and real orbitals will inevitably differ. However, because both orbitals must be normalized, their charge densities integrated over the region within the cut-off radius will be equal. This condition is referred to as norm-conservation. Vanderbilt developed ultrasoft pseudo-potentials, which are not norm-conserving [44]. Their main characteristic is that they can work effectively in calculations which use basis sets with much lower kinetic energy cut-offs. A full discussion of them can be found in reference [44].

In an all-electron calculation, the valence-electron wavefunctions must oscillate rapidly in the region surrounding the core. This is to maintain orthogonality between the valence and core-electron wavefunctions. Accurately describing such functions is computationally expensive as it requires a large basis set (i.e. a high KE-cut-off). In the pseudo-potential approximation there are no core orbitals with which the valence wavefunctions must be orthogonal. Consequently, the valence-electron wavefunctions can be smooth over the core region. This does mean that the description of the valence wave-function in the core region is extremely poor. However, provided the aforementioned constraints are satisfied, this will not impair the overall accuracy of the calculation.

A pseudo-potential, $V_{pspot}(\mathbf{r}, \mathbf{r}')$, is often split into a local, $V_{loc}(\mathbf{r})$, and a non-local component , $V_{non-local}(\mathbf{r}, \mathbf{r}')$, i.e.

$$V_{pspot}(\mathbf{r}, \mathbf{r}') = V_{loc}(\mathbf{r}) + V_{non-local}(\mathbf{r}, \mathbf{r}'). \tag{3.45}$$

Kleinman and Bylander developed a simplified form of the non-local component [45], which is:

$$\hat{V}_{non-local} = \sum_{lm} \frac{|\theta_{lm}\delta V_l\rangle\langle\delta V_l\theta_{lm}|}{\langle\theta_{lm}|\delta V_l|\theta_{lm}\rangle}. \tag{3.46}$$

Here, θ_{lm} is the pseudo-orbital associated with angular momentum quantum number l, and magnetic quantum number m. δV_l is defined by

$$\delta V_l = V_{l,non-local} - V_{loc}, \tag{3.47}$$

where $V_{l,non-local}$ is the non-local component of the pseudo-potential associated with angular momentum l.

3.3 ONETEP

3.3.1 Non-orthogonal generalized Wannier functions

In ONETEP, the Kohn-Sham orbitals are described in terms of a set of non-orthogonal localized Wannier functions (NGWFs), $\phi_\alpha(\mathbf{r})$ [46]:

$$\psi_i(\mathbf{r}) = \sum_{\alpha}^{N_\alpha} \phi_\alpha(\mathbf{r}) M_i^\alpha. \tag{3.48}$$

Here, N_α is the number of NGWFs used to describe the wavefunction $\phi_\alpha(\mathbf{r})$. These NGWFs are centred upon the centres of the atoms within the system. However, the NGWFs are themselves defined in terms of a basis set of psinc functions [46]. This set of psinc functions is a unitary rotation of a set of plane waves [47]. The psincs are defined on a regular grid of points. Figure 3.1 shows a 2D psinc function. The expression for an NGWF described in terms of psincs is:

$$\phi_\alpha(\mathbf{r}) = \sum_{k}^{N_{ps}} D_k(\mathbf{r}) C_{k,\alpha}. \tag{3.49}$$

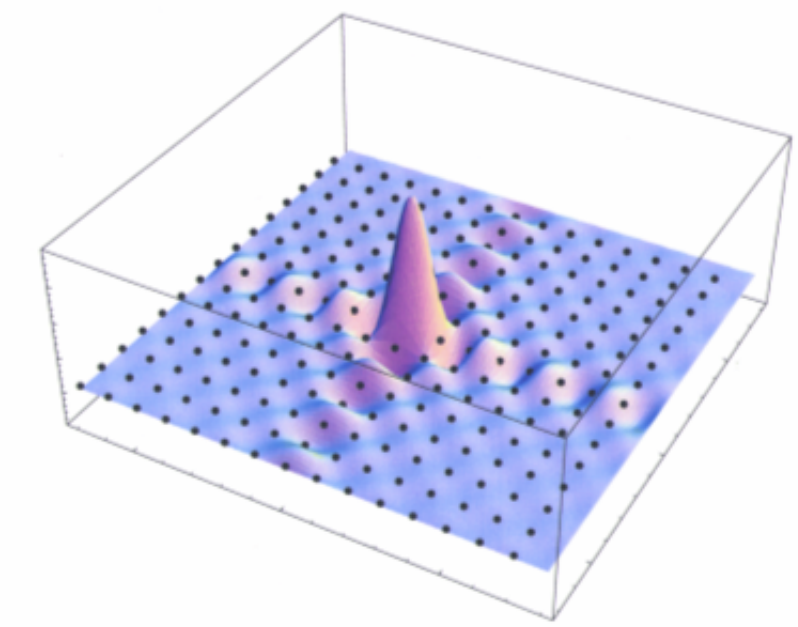

Figure 3.1: A depiction of a psinc function. Image from [46].

Here, N_{ps} are the number of psincs, the $\{C_{k,\alpha}\}$ are the coefficients which define ϕ_α in terms of the psinc $\{D_k(\mathbf{r})\}$ centred on point k (see Figure 3.2). In ONETEP, the coefficients $\{C_{k,\alpha}\}$ are optimized during the calculation. The NGWFs are localized. Therefore, all coefficients, $C_{k,\alpha}$, which correspond to psincs, the centres of which are outside the localization sphere of the NGWF, $\phi_\alpha(\mathbf{r})$, are known to be zero, and need not be optimized. Consequently, it is possible to attain the level of accuracy associated with plane wave basis sets, whilst reaping the computational benefits associated with basis sets comprised of localized functions. The expression for the density in ONETEP is:

$$\rho(\mathbf{r}) = \sum_{\beta}^{N_{basis}} \sum_{\alpha}^{N_{basis}} \phi_\alpha(\mathbf{r}) K^{\alpha\beta} \phi_\beta(\mathbf{r}), \tag{3.50}$$

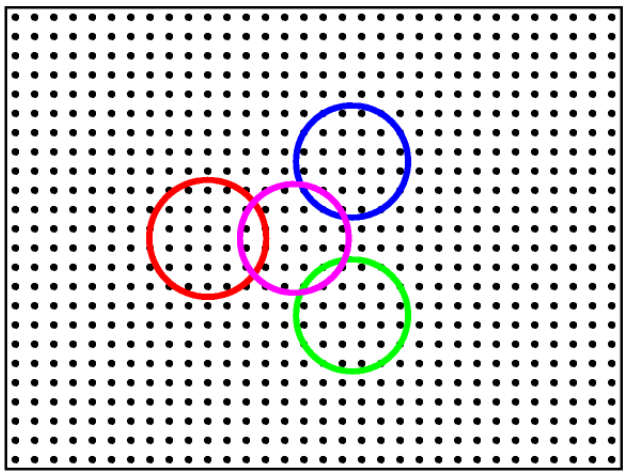

Figure 3.2: A depiction of 3 overlapping NGWFs on a grid of points. Image from [46].

where $K^{\alpha\beta}$ is referred to as the density kernel. It is defined by

$$K^{\alpha\beta} = \sum_{i}^{N} M_{i}^{\alpha} f_i M_{\ i}^{\beta}. \tag{3.51}$$

Here, f_i is the occupancy of ith orbital, $\Psi_i(\mathbf{r})$. ONETEP truncates the NGWFs to improve computational efficiency. This means that $\phi_\alpha(\mathbf{r})$ is equal set to zero outside a spherical volume of radius r_{cut} centred on a given point r_α, i.e.

$$\phi_\alpha(\mathbf{r}) = \begin{cases} \phi_\alpha(\mathbf{r}) & \text{if } (|\mathbf{r}_\alpha - \mathbf{r}|) \leq r_{cut} \\ 0 & \text{if } (|\mathbf{r}_\alpha - \mathbf{r}|) > r_{cut} \end{cases}. \tag{3.52}$$

The computational cost of calculations in ONETEP scales more favourably with system size than it does standard in plane-wave codes [1]. In insulating materials it is possible to apply the principle of the near-sightedness of electronic matter, which states that the interaction between electrons centred on atoms a long way apart is negligible [48]. Therefore, when the Hamiltonian is represented in a space defined by localized functions, e.g. the NGWFs, it can be accurately represented

by a sparse matrix. It is possible to find the Kohn-Sham orbitals by diagonalizing the Hamiltonian (see (3.44)), but this can be avoided in ONETEP through use of sparse matrix algebra techniques [1]. Additionally, the kernel is made sparse by omitting those elements which correspond to NGWFs whose centres are far apart. Consequently, the computational cost of ONETEP calculations scales more favorably with system size than it does in many other programs. It should be noted that the principle of near-sightedness does not apply in systems, such as metals, in which the electron wavefunctions are more delocalized. As a result, other techniques must be used in ONETEP calculations on metallic systems, and these are discussed in section 3.4.

3.3.2 Structure of a ONETEP calculation

The use of a set of NGWFs makes the basic structure of a ONETEP calculation quite different to one carried out in more traditional codes such as CASTEP [2] or NWChem [49]. In such programs, there is one main loop, in which the coefficients M_i^α in (3.48) are found. However, in ONETEP, there are two loops (see Figure 3.3). In the inner loop the kernel, $K^{\alpha\beta}$, is optimized, and this loop is similar to the single loop in CASTEP or NWChem. In the outer loop, the coefficients, $\{C_{k,\alpha}\}$, which define the NGWFs in terms of psincs are optimized. At the start of a ONETEP calculation the NGWFs are initialized. Pseudo-atomic orbitals are a good initial guess for the form of the NGWFs [50][51]. These are functions which closely resemble the atomic orbitals associated with the atom upon which the NGWF is centred. It is possible to specify the atomic orbitals to which the NGWFs are initialized, as well as the occupancy of these initial orbitals.

The only atomic orbitals which *have* to be described are those which are occupied

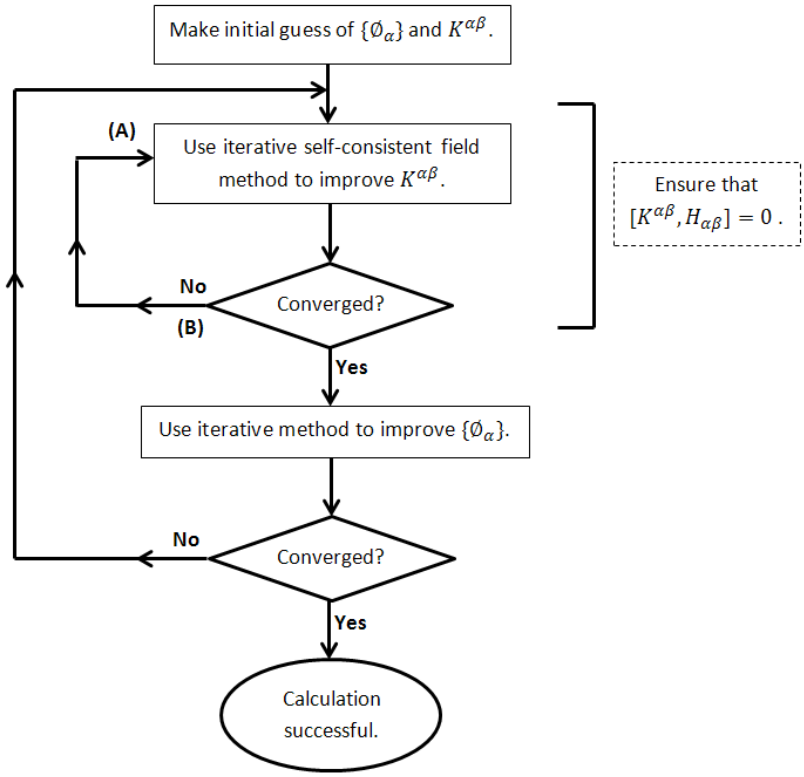

Figure 3.3: An outline of the two optimization loop method used in a ONETEP calculation. This schematic is a duplication of that found in [23].

in the isolated atom, and which are not counted as core by the pseudo-potential. This bare minimum number of functions is called a single-zeta set*[3]. For an oxygen atom this would consist of 4 functions; 1 for describing the 2s orbital, and 3 functions for describing the 2p orbitals. Larger sets are sometimes used, this increases the expressive capability in the initial stages of a calculation, and can improve convergence. An example of a larger set is a double zeta set. This is similar to a single zeta set, but it uses twice as many functions, two for describing each orbital. Sometimes functions for describing higher, formally unoccupied orbitals are also included.

Following initialization of the NGWFs it is possible to make an initial estimate of the density. This estimate will be calculated directly from the overlap of the atomic orbitals. The density is then used to construct the initial Hamiltonian. This Hamiltonian is then used to find a new density kernel, which can be used to calculate the charge density, and this charge density is used to construct a new Hamiltonian, and the cycle repeats. This occurs in the inner loop of Figure 3.3. The inner loop repeats until the kernel constructs a density which minimizes $E[n]$, and which satisfies the constraints relevant to that calculation [23]. The calculation then proceeds to the outer loop of Figure 3.3, where new NGWFs, which minimize $E[n]$, are calculated.

[3]The term single-zeta basis set is more common, but as the NGWFs are optimized during the calculation, and are themselves described in terms of a basis set comprised of psincs, referring to the NGWFs as the basis can be misleading.

3.4 DFT calculations on metallic systems

Accurate description of metallic systems using DFT can be challenging [52], and it is necessary to use different techniques to those employed in a standard ONETEP calculation.

3.4.1 Use of finite temperature DFT for metallic systems

Metallic systems have no band gap, i.e. the energies of orbitals near the Fermi-level are degenerate. In order to describe such systems accurately it is necessary to use a finite temperature formulation of DFT. The first reason for this is the need to account for thermal excitations. In cases where there is a large[4] band gap, thermal excitations do not need to be accounted for, as they will not significantly effect the electronic structure of the system. However, if there is no band gap these thermal excitations will be important, and it is necessary to use a finite temperature formulation of DFT.

A second reason for use of finite temperature DFT is associated with determination of the occupancies. In zero temperature formulations of DFT the Kohn-Sham orbitals have integer occupancies determined by the Aufbau principle. If there are N electrons, then it is the N states with the lowest energy which are occupied. This can be a problem for systems with no band gap: Consider two degenerate orbitals, $\psi_1(\mathbf{r})$ and $\psi_2(\mathbf{r})$, both of which have the same energy eigenvalue $\epsilon_1 = \epsilon_2 = \epsilon_F$, where ϵ_F is the Fermi energy. One of these orbitals will be fully occupied, whilst the other will be unoccupied. If the occupancies, f_1 and f_2, of the orbitals, $\psi_1(\mathbf{r})$ and $\psi_2(\mathbf{r})$, are determined solely by the Aufbau principle, then it is not possible to

[4]Large relative to the size of the thermal excitations.

determine which of the two degenerate orbitals should be occupied[5]. However, if $\psi_1(\mathbf{r}) \neq \psi_2(\mathbf{r})$, then the charge density may differ depending on which orbital is occupied. Partial occupancies provide a solution to this. By assigning each orbital the same fractional occupancy, i.e. $f_1 = f_2$, it is possible to specify that each of these two orbitals have an equal probability of being occupied.

If integer occupancies are used when attempting to describe a system with no band gap, then the minimization procedure is likely to destabilize. In the early stages of a calculation, the Kohn-Sham orbitals, and their energies, can change significantly. Consequently, if an orbital is close to the Fermi level, its occupancy may change between successive iterations. This change can result in a disproportionately large change in the charge density, causing the calculation to destabilize. Use of partial occupancies does not prevent the occupancies of orbitals from changing, but enables occupancies to change by fractional amounts, thus reducing the extent of the destabilization.

3.4.2 Pulay mixing

Pulay density mixing [53] is a computational technique used to help stabilize convergence of calculations[6]. In the implementation of Pulay density mixing in ONETEP, the input density kernel, $K_{in}^{\alpha\beta}$, (which enters at point (A) in Figure 3.3) is calculated from a combination of the output density kernels, $K_{in}^{\alpha\beta}$, (which were output at point (B) in Figure 3.3) generated on previous iterations. The contribution of an output density kernel, $K_{p,out}^{\alpha\beta}$, generated on iteration p, to the input

[5] In practical calculations, one of the orbitals will be set to be occupied, as due to computational noise, it is rare two energies are ever identical.

[6] Pulay mixing is a general purpose technique, and not specific to finite temperature DFT, but the two techniques are often used in tandem when performing calculations on metallic systems.

density kernel, $K^{\alpha\beta}_{q,in}$, on iteration, q, is determined by the self consistency of $K^{\alpha\beta}_{p,out}$. An output kernel, $K^{\alpha\beta}_{p,out}$, is said to be self consistent if it is similar to the output kernel generated on the previous iteration, i.e. $K^{\alpha\beta}_{p,out}$ is self consistent if $K^{\alpha\beta}_{p,out} \approx K^{\alpha\beta}_{(p-1),out}$. Pulay mixing can help to stabilize convergence. However, it is not a direct energy minimization technique, and it does not guarantee that the energy (or free energy) will always decrease between successive iterations. Consequently, some calculations can still become unstable. In these cases, a direct energy minimization technique, such as ensemble DFT [54], should be used.

3.4.3 Ensemble DFT

In a finite temperature DFT calculation the quantity to be minimized is the free energy. When written in ONETEP notation, the free energy, $A[T;\{\phi_\alpha\},K^{\alpha\beta}]$, is given by:

$$A[T;\{\phi_\alpha\},K^{\alpha\beta}] = \sum_{\alpha,\beta} K^{\alpha\beta}\langle\phi_\alpha(\mathbf{r})|\hat{T}+\hat{V}_{ext}|\phi_\beta(\mathbf{r})\rangle + U_H[n] + V_{XC}[n] - TS[K^{\alpha\beta}]. \tag{3.53}$$

Here, T is the temperature, and $S[K^{\alpha\beta}]$ is the entropic contribution to the free energy. There is a unique ground state density which corresponds to the minimized free energy. However, there may be difficulties in finding this minimum. If some of the Kohn-Sham orbitals are degenerate, then there will be multiple different sets of Kohn-Sham orbitals which correspond to the same density.

This is problematic when using computational methods to solve the Kohn-Sham equations. For a minimization algorithm to work effectively the representation of the molecular orbitals must remain constant between iterations, i.e. rotations of

the orbitals between successive iterations must be prevented. This was one of the factors which motivated Marzari, Vanderbilt and Payne to develop a method called ensemble DFT (EDFT) [54]. In EDFT, the occupancies of the Kohn-Sham orbitals are treated as a new degree of freedom. The free energy of the system is then minimized variationally with respect to the occupancies. Taking this approach greatly increases the stability of the calculation.

The implementation of Mermin's finite temperature DFT in ONETEP is inspired by the EDFT method developed by Marzari, Vanderbilt and Payne [54]. The minimization procedure of a ONETEP calculation which utilizes EDFT is outlined in a flow chart in Figure 3.4, and was developed by Alvaro Ruiz-Serrano, a member of the Skylaris group.

As seen earlier, in ONETEP, the charge density is given by:

$$n(\mathbf{r}) = \sum_i f_i \psi_i^*(\mathbf{r})\psi_i(\mathbf{r}) = \phi_{\ \alpha}(\mathbf{r}) K^{\alpha\beta} \phi_\beta(\mathbf{r}). \tag{3.54}$$

Here, the f_i are equal to the diagonal elements of the ground state density matrix ρ_0 discussed in the previous section. In the above equation, and from now on in this thesis, there is an implicit summation over repeated Greek indices.

The density kernel, $K^{\alpha\beta}$, will be diagonal when represented in the space of the Kohn-Sham orbitals. The diagonal elements, f_i, are often interpreted as the probability of the ith Kohn-Sham orbital being occupied. The occupancies of the Kohn-Sham orbitals are calculated using the Fermi-Dirac distribution [18]:

$$f_i = (1 + e^{\frac{-(\mu-\epsilon_i)}{k_B T}})^{-1}, \tag{3.55}$$

where μ is the chemical potential. In order to calculate the occupancies it is nec-

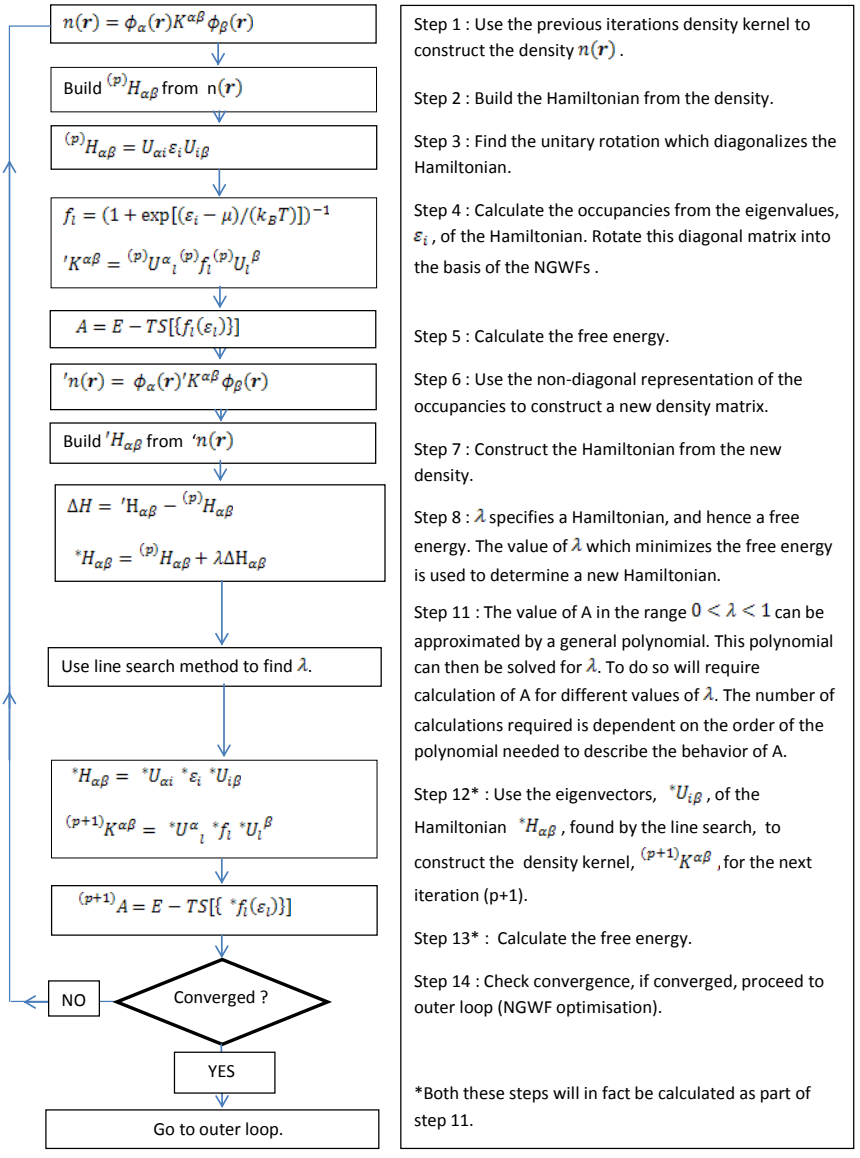

Step 1 : Use the previous iterations density kernel to construct the density $n(\boldsymbol{r})$.

Step 2 : Build the Hamiltonian from the density.

Step 3 : Find the unitary rotation which diagonalizes the Hamiltonian.

Step 4 : Calculate the occupancies from the eigenvalues, ε_i , of the Hamiltonian. Rotate this diagonal matrix into the basis of the NGWFs .

Step 5 : Calculate the free energy.

Step 6 : Use the non-diagonal representation of the occupancies to construct a new density matrix.

Step 7 : Construct the Hamiltonian from the new density.

Step 8 : λ specifies a Hamiltonian, and hence a free energy. The value of λ which minimizes the free energy is used to determine a new Hamiltonian.

Step 11 : The value of A in the range $0 < \lambda < 1$ can be approximated by a general polynomial. This polynomial can then be solved for λ. To do so will require calculation of A for different values of λ. The number of calculations required is dependent on the order of the polynomial needed to describe the behavior of A.

Step 12* : Use the eigenvectors, ${}^{*}U_{i\beta}$, of the Hamiltonian ${}^{*}H_{\alpha\beta}$, found by the line search, to construct the density kernel, ${}^{(p+1)}K^{\alpha\beta}$, for the next iteration (p+1).

Step 13* : Calculate the free energy.

Step 14 : Check convergence, if converged, proceed to outer loop (NGWF optimisation).

*Both these steps will in fact be calculated as part of step 11.

Figure 3.4: Structure of ONETEP inner loop for ensemble DFT, as developed by Alvaro Ruiz-Serrano.

essary to know the energies of the Kohn-Sham orbitals.

An EDFT calculation in ONETEP involves two loops. In an inner loop, the kernel which minimizes the free energy, $A[T;\{\phi_i\},K^{\alpha\beta}]$, as defined in (3.53), is calculated. This is achieved through use of an iterative line search in the space of Hamiltonians. To see how the inner loop minimization procedure works in an EDFT calculation, please refer to Figure 3.4, which describes the inner loop of a ONETEP calculation, which was outlined earlier in Figure 3.3. At the end of the inner loop, the kernel $K^{\alpha\beta}$ (and hence the occupancies, $\{f_i\}$, of the Kohn-Sham orbitals $\{\psi_i(\mathbf{r})\}$, and their representation $\{M_i^\alpha\}$ in the space of the NGWFs) which minimizes the free energy is known. This kernel is then used to define a functional, $G[T;\{\phi_\alpha\}]$, which satisfies:

$$G[T;\{\phi_\alpha\}] := \min_{K^{\alpha\beta}} A[T;\{\phi_\alpha\},K^{\alpha\beta}]. \tag{3.56}$$

$G[T;\{\phi_\alpha\}]$ is independent of the occupancies. In the outer loop, a line search procedure is used to variationally minimize $G[T;\{\phi_\alpha\}]$ with respect to the NGWFs. The two-loop process is then repeated until self-consistency is achieved, and the $\{\phi_\alpha\}$ and $K^{\alpha\beta}$ which minimize $A[T;\{\phi_\alpha\},K^{\alpha\beta}]$ are found.

Chapter 4

Calculations of chemisorption of atomic oxygen on platinum slabs and nanoparticles

The methodology to carry out finite temperature calculations on metals was newly implemented in ONETEP. Consequently, it was necessary to calibrate and test the code, and determine the optimum calculation parameters, before ONETEP could be utilised to investigate oxygen chemisorption on large platinum nanoparticles. This testing and calibration was performed by simulating chemisorption of atomic oxygen on a cuboctohedral Pt_{13} nanoparticle, and comparing the computed chemisorption energies and computed bond lengths with results found in the literature. The optimum calculation parameters are those which give results which agree with the literature, whilst enabling fast and stable calculations.

This calibration study was split into two stages. In the first stage the optimum xc-functional, kinetic energy cut-off and pseudo-potential type were identified.

These tests were performed in CASTEP, as at the time, the EDFT method had not been implemented in ONETEP. The findings will be transferable to ONETEP calculations, for when correctly calibrated, the results of ONETEP and CASTEP calculations should be equivalent. The second stage of the study was to identify the appropriate NGWF radii, and the pseudo-atomic orbitals to which the NGWFs should be initialized. This stage was carried out using ONETEP.

4.1 Calibration Stage 1 : KE cut-off, pseudo-potentials and xc-functionals

4.1.1 Motivation for study

Atomic oxygen chemisorbed on infinite platinum slabs was simulated in CASTEP. This system has been extensively investigated in the literature, making it a good choice for a calibration study. Three different aspects of the calculation were calibrated; xc-functionals, the KE cut-off and the pseudo-potential.

It is necessary to test different xc-functionals; the complexity of the interactions they are attempting to model means it is difficult to determine which functional will be most appropriate without actually testing them in calculations. Two different xc-functionals were tested: The PW91 and RPBE xc-functionals (for details, please see section 3.2.4), both of these are GGA functionals. The PW91 functional was used largely due to its predominance in the literature; the wealth of results which have been obtained using it make it a good choice for a calibration study. The RPBE functional was developed more recently, and has been shown to be significantly more accurate than other functionals in calculations of chemisorp-

tion energies of oxygen on metals [34].

There are a wide variety of pseudo-potentials available for any given element. Ideally, the xc-functional used to generate the pseudo-potentials should be the one used in the calculation. Unfortunately, a relevant pseudo-potential could not be found or generated for use with the PW91 or RPBE xc-functionals, and pseudo-potentials generated using the PBE xc-functional had to be used. This should not introduce significant error, for as explained in section 3.2.4, the PW91 and RPBE xc-functionals have much in common with the PBE xc-functional. Another aspect in which pseudo-potentials may vary is whether they account for relativistic effects, which are particularly important when describing systems involving heavy elements such as platinum. Pseudo-potentials which account for scalar relativistic effects were used, details of this can be found in reference [55].

Many pseudo-potentials specify the kinetic energy cut-off which must be used if fine accuracy is to be obtained. Typically, ultrasoft pseudo-potentials have lower KE-cut-off requirements than norm conserving pseudo-potentials[1][44]. Consequently, different ranges of cut-offs were used for the two kinds of pseudo-potentials investigated; 340 eV, 500 eV and 650 eV for calculations with the ultrasoft pseudo-potentials, and 950 eV, 1200 eV and 1500 eV for calculations with norm-conserving pseudo-potentials.

The chemisorption energies, $E_{(At.\ Oads)}$ and $E_{(Mo.\ Oads)}$, of atomic and molecular oxygen were calculated using the following equations:

$$E_{(Mo.\ Oads)} = E_{OPt_N} - \frac{1}{2}E_{O_2} - E_{Pt_N}, \tag{4.1}$$

[1]This is one of the main advantages to using them.

$$E_{(At.\ Oads)} = E_{OPt_N} - E_O - E_{Pt_N}. \tag{4.2}$$

For context and justification of the above equations please refer to the Introduction. Use of the above equations to determine $E_{(At.\ Oads)}$ and $E_{(Mo.\ Oads.)}$ requires calculation of the energies of four different systems: 1) A bare platinum slab, E_{Pt_N}, 2) an oxygen atom chemisorbed upon this platinum slab, E_{OPt_N}, 3) an isolated oxygen atom E_O, 4) an oxygen molecule in its ground triplet state E_{O_2}.

Bulk platinum has a face-centred-cubic (FCC) structure [56]. The surface of the platinum slab was chosen to be the plane with Miller indices (111). This surface resembles the facets of the cuboctohedral platinum nanoparticles used for catalysis [57].

In CASTEP and ONETEP calculations it is necessary that the system being investigated is defined inside a simulation cell. The simulations make use of periodic boundary conditions. This means that for any function, $f(\mathbf{r})$, where $\mathbf{r}$ is any point in the simulation cell, it is the case that $f(\mathbf{r}) = f(\mathbf{r} + \mathbf{A})$, where $\mathbf{A}$ is one of the vectors used to define the simulation cell. Atoms in neighbouring simulation cells will interact if there is not sufficient space between them. Sometimes this effect is desired; simulation of periodic systems, such as infinite platinum slabs, only require a small simulation cell containing a very small number of atoms. However, this can prove problematic if interaction between periodic images is not desired. To prevent these interactions, a large gap between the system being investigated and the edge of the simulation cell is often required. This increases the size of the cell, and hence the computational cost of the calculation. To prevent interactions between neighbouring images in the direction normal to the surface of the platinum slab, it was necessary to have a 20 Å gap between the surface of the slab and

the top of the simulation cell (see Figure 4.2).

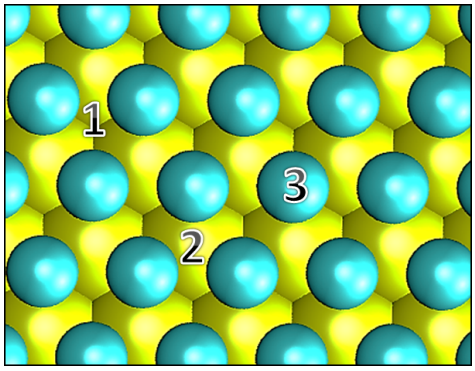

Figure 4.1: A top down view of the platinum slab. Both teal and yellow circles correspond to platinum atoms. The teal circles are the top layer of Pt atoms, the yellow circles are the second layer. Different numbers correspond to adsorption sites:1) FCC, 2)HCP, 3)TOP.

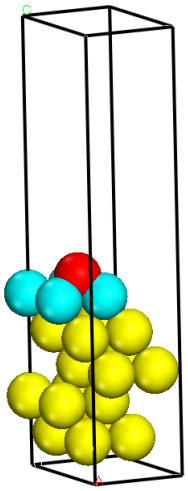

Figure 4.2: The CASTEP simulation cell used for calculation of oxygen adsorption at the FCC site. As in fig(4.1) both teal and yellow spheres correspond to platinum atoms. The red sphere is the oxygen atom.

The size of the simulation cell will have an effect on the size of the basis set used. A larger basis set will result in a better description of the system, and hence a lower energy (due to the variational principle). It is important that all the calculations used to acquire the values necessary for determination of the chemisorption energy are performed using the same basis set. Therefore, it is essential that the simulation cell is the same size in every calculation.

4.1.2 Construction of simulation cell and calculation procedure

The simulation cell for modelling the platinum slab was constructed from a platinum unit cell. The lattice parameter of platinum is measured experimentally to be 3.92 Å at 293.15K [58]. Lattice parameters obtained from computational

calculations are dependent on the calculation parameters used, particularly the pseudo-potential and xc-functional. To ensure consistency, it was necessary to calculate a platinum lattice parameter specific to each set of calculation parameters, i.e. a different lattice parameter for each combination of pseudo-potential, xc-functional and KE-cutoff. This was achieved by using the experimental lattice parameter to construct a platinum unit cell, and then using a CASTEP calculation, with the relevant parameters, to optimize the geometry of this unit cell. The difference between the optimized and experimental lattice parameter was relatively small (usually an expansion of $<$0.05 Å; a change of $<$2%). Nonetheless, a high level of consistency is important if the different calculation parameters are to be accurately compared. This optimized unit cell was then used to construct a $2\times2\times1$ platinum slab (see Figure 4.2). A vacuum layer directly above the surface of the platinum slab of 20 Å was used to ensure periodic images (in the vertical direction) did not interact.

The calculation procedure was provided by Dr. Misbah Sarwar of Johnson Matthey P.L.C.. This procedure was used to calculate chemisorption energies for all combinations of the above described pseudo-potential, kinetic energy cut-off and xc-functional.

The calculations in CASTEP were finite temperature calculations using a density smearing and kernel mixing approach as outlined in [59]. A Gaussian smearing scheme with a smearing width of 0.2 eV was used to determine the values of the partial occupancies. This corresponds to an electronic temperature of 2320.8 K. Pulay mixing [60] was used to aid convergence of the calculation. This technique has been shown to greatly improve convergence in calculations on metallic systems [59]. A Monkhorst-Pack reduced 5x5x1 k-point grid [61] was used in the

calculations (with 16 actual k-points).

The procedure used to obtain the energies; E_{OPt_N}, E_{Pt_N}, E_O and E_{O_2} as defined in equation (4.2) and (4.1), necessary for the calculation of the oxygen chemisorption was as follows.

- The positions of the top 3 layers atoms in the bare platinum slab were optimized in CASTEP, and the value of E_{Pt_N} was obtained, (see equations (4.1) and (4.2)).

- An oxygen atom was then placed at the FCC, HCP or ATOP chemisorption site ('1', '2' and '3' in Figure 4.1) on the optimized platinum slab.

- The positions of the top 3 layers of platinum atoms, as well as that of the oxygen, were then optimized, and the value of E_{OPt_N} was obtained (see equations (4.1) and (4.2)).

- A single point energy calculation on a single oxygen atom was then performed, and the value of E_O was obtained (see equation (4.2)).

- A geometry optimization calculation was performed on an O_2 molecule in a triplet state, and the value of E_{O_2} was obtained (see equation (4.1)).

4.1.3 Results of Calibration study

The results obtained from the calibration study are included in Tables 4.1 and 4.2.

Table 4.1: Computed chemisorption energies for atomic oxygen on a Pt(111) slab. The relative energies are the chemisorption energies w.r.t. the energy of chemisorption at the FCC site. The relative energies are the same for both $E_{(At.\ Oads)}$ and $E_{(Mo.\ Oads)}$. These results were obtained from CASTEP calculations using a RPBE functional.

	Adsorption site	Ultrasoft pseudo-potential			Norm-conserving pseudo-potential		
Basis set cut off (eV)		340	500	650	950	1200	1500
$E_{(At.\ Oads)}$ (eV) see eqn. (4.2)	FCC	-3.39	-3.43	-3.44	-3.64	-3.64	-3.64
	HCP	-2.98	-3.02	-3.02	-3.19	-3.18	-3.17
	ATOP	-1.97	-2.02	-2.01	-2.29	-2.29	-2.29
$E_{(Mo.\ Oads)}$ (eV) see eqn. (4.1)	FCC	-0.78	-0.79	-0.79	-0.85	-0.85	-0.85
	HCP	-0.37	-0.37	-0.37	-0.39	-0.39	-0.39
	ATOP	0.64	0.63	0.64	0.50	0.50	0.50
Relative Energies (eV)	HCP	0.41	0.41	0.42	0.46	0.47	0.46
	ATOP	1.42	1.41	1.43	1.36	1.36	1.35

Table 4.2: Computed chemisorption energies for atomic oxygen on a Pt(111) slab. The relative energies are the chemisorption energies w.r.t. the energy of chemisorption at the FCC site. The relative energies are the same for both $E_{(At.\ Oads)}$ and $E_{(Mo.\ Oads)}$. These results were obtained from CASTEP calculations using an PW91 xc-functional.

	Adsorption site	Ultrasoft pseudo-potential			Norm-conserving pseudo-potential		
Basis set cut off (eV)		340	500	650	950	1200	1500
$E_{(At.\ Oads)}$ (eV) see eqn. (4.2)	FCC	-3.60	-3.93	-3.86	-3.78	-4.09	-4.09
	HCP	-3.17	-3.50	-3.43	-3.30	-3.62	-3.62
	ATOP	-2.03	-2.34	-2.28	-2.27	-2.58	-2.58
$E_{(Mo.\ Oads)}$ (eV) see eqn. (4.1)	FCC	-0.96	-1.13	-1.06	-1.15	-1.15	-1.15
	HCP	-0.53	-0.70	-0.63	-0.68	-0.68	-0.68
	ATOP	0.61	0.45	0.52	0.36	0.36	0.36
Relative energies (eV)	HCP	0.43	0.43	0.43	0.47	0.47	0.47
	ATOP	1.58	1.58	1.58	1.51	1.51	1.51

4.1.4 Conclusions from calibration stage 1

The above results clearly show that the two hollow sites, the FCC and HCP, are the most energetically favorable sites for chemisorption of atomic and molecular

oxygen, with the FCC site being slightly preferable. This is in agreement with the both the computational [62] and experimental [63] literature. The ATOP site is much less favorable, and this is also in agreement with other computational studies [64]. Furthermore, near perfect agreement was found with results obtained from similar calculations performed by Dr. Misbah Sarwar of Johnson Matthey P.L.C.. This agreement provides reassurance that the method is functioning correctly.

The purpose of this study is to identify which kinetic energy cut-off and exchange functional were to be used in later ONETEP calculations. As the size of the basis set increases, so too does the precision of the calculation (see section 3.2.5). Consequently, it is expected that as the kinetic energy cut-off (and hence the size of the basis set) is increased, the results of calculations will converge to a lower total energy. However, the computational cost of the calculation scales cubically with the size of the basis set. Therefore, the optimum kinetic energy cut-off is the lowest cut-off which yields acceptable results.

The convergence of results with increasing kinetic energy cut-off is observed in the results shown in Tables 4.1 and 4.2. Calculations which use the PW91 functional and a cut off of $<$650 eV are particularly affected by an increase in cut-off. It is noticeable that the convergence of chemisorption energies appears to occur sooner for the RPBE functional than for the PW91 xc-functional. Increasing the cut off beyond 950 eV did not appear to have a significant effect, regardless of the xc-functional. However, calculations using a cut-off of $>$950 eV used a different type of pseudo-potential to those using a cut-off of 650 eV or less. Different types of pseudo-potentials are affected differently by changes in kinetic cut-off energy, and consequently the results obtained from these calculations should not

be compared.

In any case, it is clear that when using an RPBE xc-functional and the norm-conserving pseudo-potential, increasing the kinetic energy cut-off beyond 950 eV does not improve the accuracy of the calculations. It was also found that calculations using the RPBE functional appeared to take fewer iterations to converge. Hence it was decided that use of an RPBE xc-functional, with a cut off of 950 eV and a norm-conserving pseudo-potential, was the best choice for investigated chemisorption of atomic oxygen on platinum. This selection enabled accurate results to be obtained, without needlessly increasing the computational cost.

4.2 Calibration Stage 2 : NGWF radii and initialization

Correctly calibrated ONETEP calculations are theoretically equivalent to similar CASTEP calculations. Therefore, the results of calibration stage 1 can inform ONETEP calculations. Before moving onto larger systems it was necessary to determine the NGWF cut-off radii and the initial electronic configuration which resulted in fast, accurate and stable calculations.

As stated in section 3.3, the number of NGWFs, and the functions to which they are initialized, can have a major impact in the speed and stability of the calculation. By considering the Fermi-Dirac distribution, described in equation (3.55), it is apparent that when using finite temperature DFT, more than N_e Kohn-Sham orbitals will have non-zero occupancies, where N_e is the number of electrons. To accurately describe a system there must be at least as many NGWFs as there

are Kohn-Sham orbitals with non-zero occupancies. Consequently, it is necessary to use a larger than minimal set of NGWFs when performing finite temperature calculations.

The NGWFs are initialized to resemble atomic orbitals (hereafter called PAOs, see section (3.3.2)). For platinum, three different initial PAO configurations were trialed: "5d9 6s1" (6 NGWFs), "5d9 6s1|P" (9 NGWFs) and "5d9 6s1 6p0|P" (16 NGWFs). For oxygen, two different configurations were trialled "2s2 2p4" (4 NGWFs), and "2s2 2p4|P" (9 NGWFs). The number follwing specification of the orbital type denotes the occupancies of those orbitals. The "|P" means that the set of orbitals with the next angular momentum up were obtained through the polarization method described in reference [65] [2].

It is easiest to understand this notation by considering a specific example. In a closed-shell calculation, a "5d9 6s1|P" set includes 5 NGWFs to describe the 5d orbitals, which initially have an occupancy of 9; 1 NGWF to describe the 6s orbital, which initially has a occupancy of 1; 3 NGWFs to describe the 6p orbitals, which are initially unoccupied. It is not necessary to initialize NGWFs to describe the core orbitals described by the pseudo-potential. A fuller description of the generation of PAOs in ONETEP can be found in reference [66].

Determining the number and configuration of these PAOs which enables a reliable description of the system, whilst resulting in a fast and stable calculation is an important stage of this calibration study.

[2]The oxygen configuration "2s2 2p4|P" indicates that a 2p orbital is polarized to obtain a 2d orbital. This seems strange at first, as the magnitude of angular momentum quantum number should always be less than the principal quantum number, i.e. $l < n$. However, the purpose of the initialization is to provide a good starting point for the NGWF optimization. The NGWFs will change over the course of the calculation, and so an unusual initialization does not mean the final result will be unphysical.

The second component of this calibration study is the investigation of the impact of varying the NGWF-cut-off radius, discussed in section 3.3. Studies performed with other DFT codes, notably SIESTA [65], have found that varying the cut-off radius can have a significant effect on the convergence of calculations[3] [67]. Studies which utilized ONETEP in the calculation of optical adsorption spectra of the polymer poly(para-phenylene), and a metal-free phthalocyanine molecule, found that a large 12 Bohr cut-off radius was necessary [68]. Based on this, it was decided that three NGWF cut-off radii would be tested; 8, 9 and 12 Bohr. Increasing the size of the cut-off radius will generally stabilize the calculation, but it will also increase the computational cost. Therefore, the smallest radius which results in smooth convergence and acceptable results was chosen.

4.2.1 Calculation procedure

To determine the optimum NGWF radii and initialization, a variety of different combinations of the above parameters were used to perform simulations of atomic oxygen chemisorbed at the HCP site on the (111) facet of a Pt_{13} nanoparticle (see Figure 4.3). Chemisorption energies of atomic and molecular oxygen were calculated through use of equations (4.2) and (4.1). Densities of states, O-Pt and Pt-Pt bond-lengths were also calculated. These results were then compared to similar calculations performed in CASTEP.

Five different calculations were performed:

- A geometry optimization on the isolated Pt_{13} nanoparticle to obtain the value of E_{Pt_N} as defined in equation (4.2).

[3] It should be noted that in SIESTA there is no optimization of the localized functions. Consequently, the effect of varying the cut-off radii is expected to be more pronounced.

- A geometry optimization on the OPt_{13} complex, with the oxygen on the (111) facet, to obtain a value of E_{OPt_N} as defined in equation (4.2).

- A geometry optimization on the OPt_{13} complex, with the oxygen on the (100) facet, to obtain another value of E_OPt_N as defined in equation (4.2).

- A geometry optimization on an O_2 molecule, in a triplet state, to obtain the value of E_{O_2} as defined in equation (4.1).

- A single point energy calculation on an isolated oxygen atom to obtain the value of E_O as defined in equation (4.2).

The chemisorption energy of atomic oxygen on a given facet was determined using equation (4.2), and the value of E_{OPt_N} obtained from the appropriate calculation. The basic parameters of the ONETEP calculations were very similar to those used in the CASTEP calculations. A brief summary of the parameters is included in Table 4.3.

There are a few noticeable differences between the parameters used in the previous section, and those used here. The most significant of these is that both ONETEP and CASTEP made use of ensemble DFT, as opposed to the Pulay density mixing technique mentioned in the previous section. The electronic temperature was also lower (1160.45 K); this should result in a more accurate description of the system. The Fermi-Dirac distribution was used to calculate the occupancies. This is because it is physically reasonable, and because the entropic term, $S[K^{\alpha\beta}]$, in the free energy (see equation 3.53) is known analytically when the occupancies are determined using the Fermi-Dirac distribution, whereas an analytic expression for the entropy functional is not known if the occupancies are determined using a Gaussian based technique [59].

There was also a slight difference in the kinetic energy cut-off between the two calculations. The use of a psinc basis set in ONETEP necessitates that all the FFT boxes be exactly an odd number of wavelengths across. This meant that a higher kinetic energy cut-off of 1067 eV had to be used in ONETEP, whilst a lower value of 950 eV was used in CASTEP. This discrepancy should not prevent the results from being compared; it is known from the first stage of the calibration study that increasing the kinetic energy cut-off beyond 950 eV did not affect the results significantly.

The Pt_{13}, and all other platinum cuboctohedrals mentioned in this report, were constructed by cutting from a large cube of bulk platinum, constructed from a unit cell with lattice parameter 3.92 Å, which was obtained from experimental investigations of bulk platinum at 293.15K [58]. In the case of the bulk slabs (section 4.1.2) it was important to optimize the lattice parameter for the xc-functional, pseudopotential, and cutoff being used. This was for two reasons. First, the purpose of the slab calculations was to compare different sets of calculation parameters, therefore the lattice constant used must be equally suited for us in calculations with each set of parameters. Second, the geometry of the slab was not fully optimized. In the case of platinum nanoparticles, only one set of calculation parameters were used, and the geometry of the entire system was optimized; in theory, the geometry which results from a full geometry optimization calculation is independent of the input geometry (and hence independent of the lattice parameter of the bulk platinum from which the nanoparticle was cut).

Initially, geometry optimizations performed using molecular dynamics programme DL_POLY [69] were used to generate input structures for ONETEP and CASTEP calculations. However, these structures were usually noticeably asymmetric. This

asymmetry cannot be attributed to Jahn-Teller distortion [19], as these structures were obtained using classical forcefields. Therefore, this distortion is likely due to poor optimization. Calculations which made use of these asymmetric structures invariably took longer to converge than those which used structures obtained by cutting straight from bulk platinum. Consequently, it was decided not to use this method to generate input structures for calculations on larger systems.

4.2.2 Results

Values for the chemisorption energy of atomic oxygen on a Pt_{13} cuboctohedral nanoparticle, $E_{(At.\ Oads)}$, obtained using equation (4.2) and the results of ONETEP calculations performed with a variety of starting parameters are included in Table 4.4. A value obtained for, $E_{(At.\ Oads)}$, obtained from the results of similar calculations performed in CASTEP is included in Table 4.5, and will serve as a benchmark result for this calibration study.

Table 4.3: Parameters common to ONETEP and CASTEP calculations.

Electronic temperature	1160.4519 K
Exchange functional	RPBE
Size of simulation cell	55 Bohr (cubic)
k-points (CASTEP only)	1
Force convergence tolerance	0.002 Ha/Bohr

Conclusions

Results obtained from ONETEP calculations using 8 Bohr NGWFs (see Table 4.4) showed poor agreement with CASTEP (see Table 4.5). However, little improvement was seen by increasing the cut-off radius beyond 9 Bohr. Calculations using an NGWF cut-off radius of 9 Bohr converged more quickly than those using

Table 4.4: Computed chemisorption energies of oxygen on the (111) facet of Pt_{13} calculated in ONETEP using ensemble DFT. The value of $E_{(At.\ Oads)}$ was calculated using equation (4.2).

NGWF radii (Bohr)	Atomic orbital configuration	$E_{Pt_{13}O}$ (eV)	$E_{(At.\ Oads)}$ (eV)
12	Pt(5d9 6s1|P) O(2s2 2p4|P)	-9809.68	-6.07
12	Pt(5d9 6s1|P) O(2s2 2p4 3s0|P)	-9809.64	-6.03
9	Pt(5d9 6s1|P) O(2s2 2p4|P)	-9809.67	-6.06
9	Pt(5d9 6s1|P) O(2s2 2p4)	-9809.65	-6.04
9	Pt(5d9 6s1) O(2s2 2p4|P)	-9806.84	-6.54
8	Pt(5d9 6s1 6p0|P) O(2s2 2p4)	–9809.12	-7.36
8	Pt(5d9 6s1|P) O(2s2 2p4|P)	-9808.89	-7.51
8	Pt(5d9 6s1|P) O(2s2 2p4)	-9808.86	-6.71

Table 4.5: Computed chemisorption energy of oxygen on the (111) facet of Pt_{13} calculated in CASTEP using Fermi-Dirac kernel smearing with Pulay mixing. The value of $E_{(At.\ Oads)}$ was calculated using 4.2.

Number of bands	$E_{Pt_{13}O}$ (eV)	$E_{(At.Oads)}$ (eV)
129	-9810.17	-5.97

NGWFs with radii of 8-Bohr or 12-Bohr. The individual iterations of the 8-Bohr calculations were fast, but a large number was required before the calculation would converge. The 12-Bohr calculations did not need any more iterations than the 9 Bohr calculations, but the computational time required for each one of these iterations was significantly larger. Consequently, an NGWF cut-off radius of 9 Bohr was used in subsequent ONETEP calculations.

The "5d9 6s1 6p0|P" configuration of NGWFs on platinum did not yield significantly different results than the "5d9 6s1|P" configuration. However, calculations performed using the "5d9 6s1|P" configuration did yield significantly better results than the "5d9 6s1" configuration. Little change was observed as a result of increasing the number of NGWFs on oxygen from 4 to 9. Consequently, an initial PAO configuration of "5d9 6s1|P" on platinum and "2s2 2p4" on oxygen was used

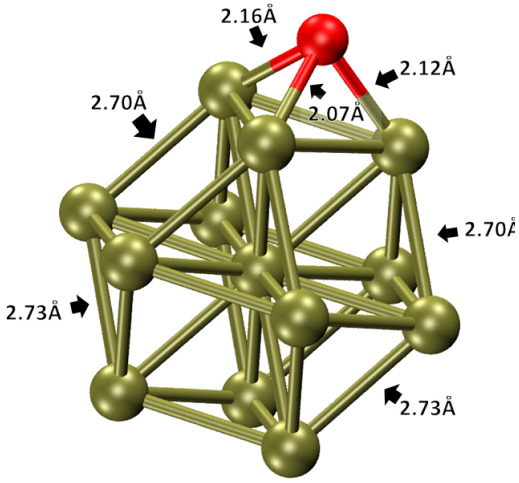

Figure 4.3: A Pt_{13} cuboctohedral with atomic oxygen chemisorbed at the HCP hollow site. The bond lengths in the figure were obtained by a geometry optimization calculation performed in ONETEP.

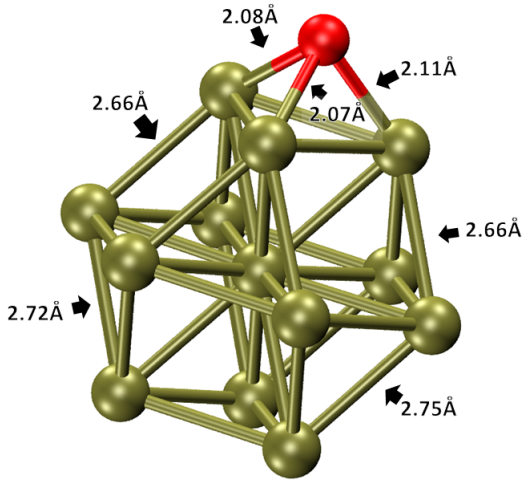

Figure 4.4: A Pt_{13} cuboctohedral with atomic oxygen chemisorbed at the HCP hollow site. The bondlengths in the figure were obtained by a geometry optimization calculation performed in CASTEP.

in subsequent ONETEP calculations.

4.2.3 Validation of ONETEP methodology using CASTEP

Before larger structures could be investigated, it was necessary to ensure that there was good agreement between CASTEP calculations, and ONETEP calculations using the above defined parameters.

4.2.4 Agreement between geometries

It was necessary to check that there was agreement between the structures resulting from geometry optimization calculations performed in ONETEP and CASTEP. The structures resulting from geometry optimizations of OPt_{13} with O chemisorbed

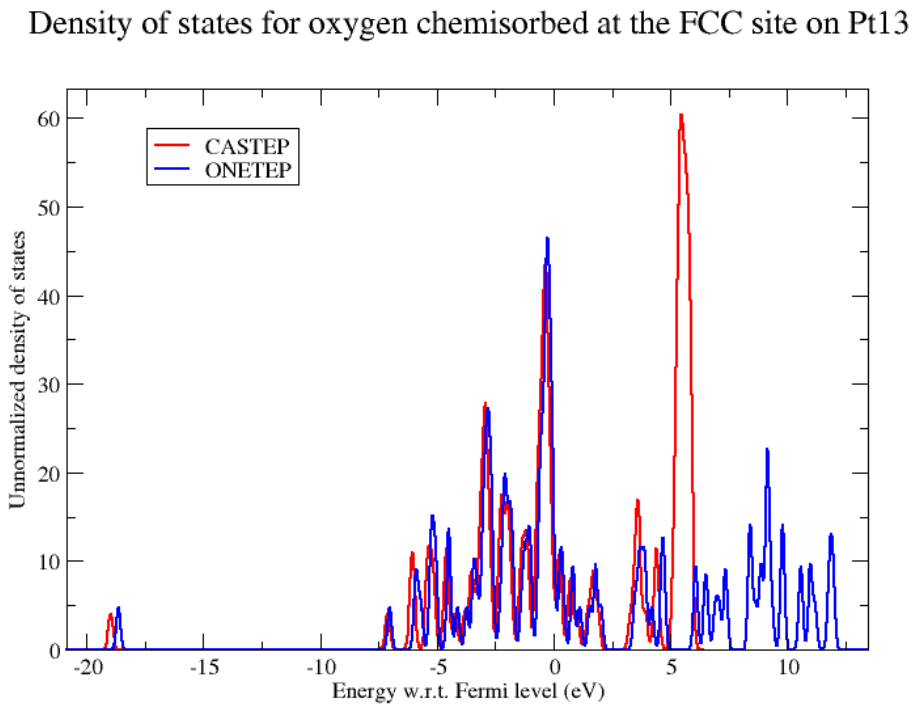

Figure 4.5: Comparison density of states obtained in ONETEP and CASTEP DOS. The ONETEP results were obtained using an initial PAO configuration "Pt-5d9,6s|P O-2s2,2p4" with 9 Bohr NGWF radii.

at the FCC site, performed in ONETEP and CASTEP are shown in Figures 4.3 and 4.4. It is apparent that for the most part there is reasonable agreement between the two geometries; all bond lengths except one agree to within 0.05 Å. CASTEP and ONETEP both yielded structures in which the Pt-Pt bond lengths are noticeably shorter than the bulk Pt-Pt bond length of 2.77 Å. Furthermore, both geometries show that the Pt-Pt bonds in the layer nearest the chemisorbed oxygen are significantly shorter than those in the layer furthest away. For example, in the geometry obtained using CASTEP the Pt-Pt bond length in the layer immediately below the chemisorption site is on average 0.08 Å shorter than those bonds in the layer fur-

ther away[4]. In summary, there is good agreement between the structures obtained from geometry optimizations performed in ONETEP and CASTEP.

4.2.5 Agreement between densities of states

Densities of states (D.O.S.) were also calculated from the charge densities obtained from ONETEP and CASTEP (see Figure 4.5). The D.O.S. provides an indication of how many electronic states are available at a given energy level, and provides insight into the electronic structure of a system. It can be calculated through use of the following formula:

$$G(\epsilon) = \sum_i \Upsilon(\epsilon_i, \epsilon)\langle\psi_i|\psi_i\rangle, \tag{4.3}$$

where $G(\epsilon)$ is the value of the density of states at energy ϵ, $|\psi_i\rangle$ is the ith Kohn-Sham orbital with energy ϵ_i, and $\Upsilon(\epsilon_i, \epsilon)$ is a smearing function. Strictly speaking, $\Upsilon_(\epsilon_i)$ should be a delta function, so that $G(\epsilon_i, \epsilon) = 0$ if $\epsilon \notin \{\epsilon_i\}$. However, the plot of such a density of states function would be difficult to read. Consequently, in the case of the above plot (and most other D.O.S. plots), $\Upsilon(\epsilon_i, \epsilon)$ is a Gaussian function of form:

$$\Upsilon(\epsilon_i, \epsilon) = \exp\left[-\frac{(\epsilon - \epsilon_i)^2}{k_B T}\right], \tag{4.4}$$

where k_B is the Boltzmann constant and T is the temperature. As the units of $k_B T$ are units of energy, often the magnitude of the smearing is expressed as an energy. For example, 0.1 eV is commonly used and corresponds to a temperature of 1160.4 K. Inspection of equation (4.4) reveals that the larger the value of the

[4]This average was calculated from all Pt-Pt bonds on the lower layer, not just those depicted in in Figures 4.3 and 4.4.

denominator, the greater the smearing. The value of k_BT is often referred to as the smearing width.

From Figure 4.5 it is clear that the densities of states obtained using ONETEP and CASTEP agree well at energies less than 3 eV above the Fermi energy, but poorly at higher energies. This is because the Kohn-Sham orbitals which contribute most to the charge density are those with high occupancies ($f_i \approx 1$). If a Kohn-Sham orbital has a low occupancy ($f_i \approx 0$) then it will contribute little or nothing to the charge density. Determination of the Kohn-Sham orbitals relies upon the fact that the Kohn-Sham orbitals correspond to the charge density which minimizes the energy. If a Kohn-Sham orbital has a low occupancy (i.e. is high in energy), then the energy will be largely independent of the form of this orbital. A consequence of this is that the high-energy, low occupancy states are often poorly described [68]. Therefore, the disagreement, at high energies, between the D.O.S. obtained from ONETEP and CASTEP does not indicate a significant difference in the ground state charge density obtained in these two calculations. That the D.O.S. agree well at energies below the Fermi-level is what is most important with regards to checking the consistency of results obtained from ONETEP and CASTEP calculations.

4.2.6 Re-validation with a different pseudo-potential

Investigation of larger nanoparticles initially proved very difficult; calculations were significantly slower than expected. In an attempt to speed up and improve convergence of calculations different calculation starting parameters were investigated. Different electronic temperatures, strengths of kinetic energy precondi-

tioning[5], initial structures, polarizations of the nanoparticles and kinetic energy cut-offs were all tried. However, none of these investigations significantly improved the speed or stability of calculations.

Eventually it was discovered that using different pseudo-potentials for platinum and oxygen enabled calculations to converge significantly faster. The new pseudopotentials had been generated by the Rappe group [71]. The improvement was a surprise, as the new, Rappe pseudo-potentials were very similar to the older, Ming-Hsien-Lee pseudo-potentials used in previous calculations; both pairs of pseudo-potentials were generated using the OPIUM [72] software for use with the PBE xc-functional. A possible explanation is that the Rappe pseudo-potentials were generated with a newer version of OPIUM, which was able to produce pseudo-potentials which can account better for non-local effects [73]. Unfortunately, this cannot be ascertained, as the version of OPIUM used to generate the pseudo-potentials is not specified in the pseudo-potential files.

Use of a different pseudo-potential can have a significant effect on the results of a calculation. Consequently it was necessary to perform a brief re-validation of EDFT in ONETEP. This was done by using CASTEP and ONETEP to calculate the chemisorption energy of atomic oxygen at the hollow sites on the (111) and (100) facets of a Pt_{13} nanoparticle. These calculations used the method described earlier in section 4.2.1, and the parameters described in the calibration summary, section 4.3.

The optimized geometries obtained from these ONETEP calculations were used as inputs for geometry optimization calculations which were performed in CASTEP. If the interatomic forces in an optimized structure are calculated to be the same in

[5] See [70] for more details.

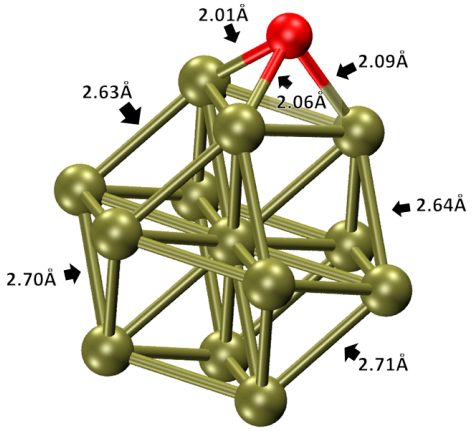

Figure 4.6: A Pt_{13} cuboctohedral with atomic oxygen chemisorbed at the FCC hollow site on the (111) facet. The bond lengths in the figure were obtained by a geometry optimization calculation performed in ONETEP.

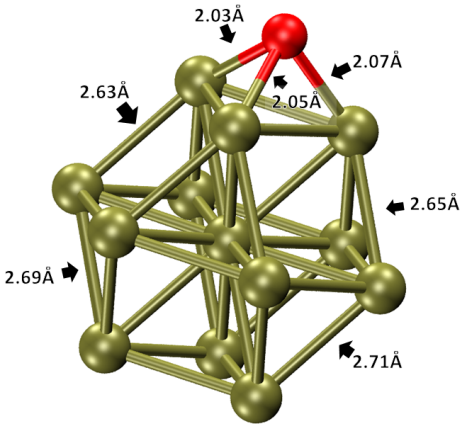

Figure 4.7: A Pt_{13} cuboctohedral with atomic oxygen chemisorbed at the FCC hollow site on the (111) facet. The bond lengths in the figure were obtained by a geometry optimization calculation performed in CASTEP.

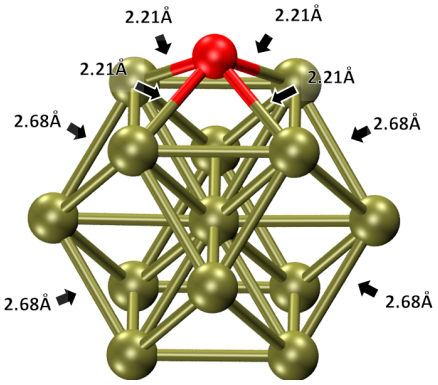

Figure 4.8: A Pt_{13} cuboctohedral with atomic oxygen chemisorbed at the hollow site on the (100) facet. The bond lengths in the figure were obtained by a geometry optimization calculation performed in ONETEP.

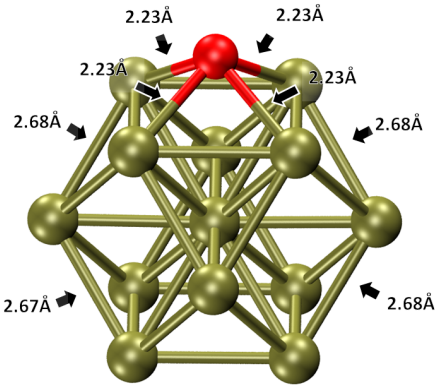

Figure 4.9: A Pt_{13} cuboctohedral with atomic oxygen chemisorbed at the hollow site on the (100 facet). The bond lengths in the figure were obtained by a geometry optimization calculation performed in CASTEP.

ONETEP and CASTEP, then the geometry optimization in CASTEP would converge after a single point energy calculation, as CASTEP would be effectively

starting with a pre-optimized geometry. This did not happen exactly, and the geometry in CASTEP changed very slightly. The optimized geometries obtained using ONETEP and CASTEP with the new pseudo-potential can be seen in Figures (4.6), (4.7), (4.8) and (4.9).

The chemisorption energies of atomic oxygen are shown in Table 4.6, and were obtained through use of equation (4.2). The agreement between CASTEP and

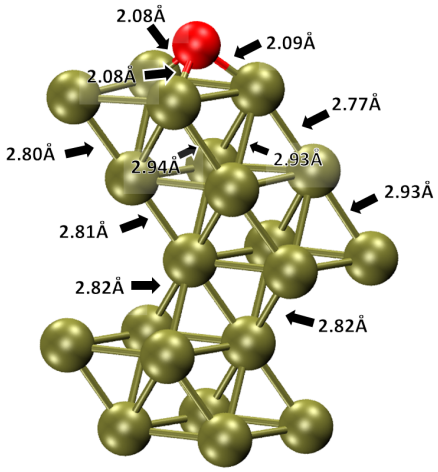

Figure 4.10: An oxygen atom chemisorbed on the FCC site on a (111) surface of a platinum slab. The structure was determined using CASTEP.

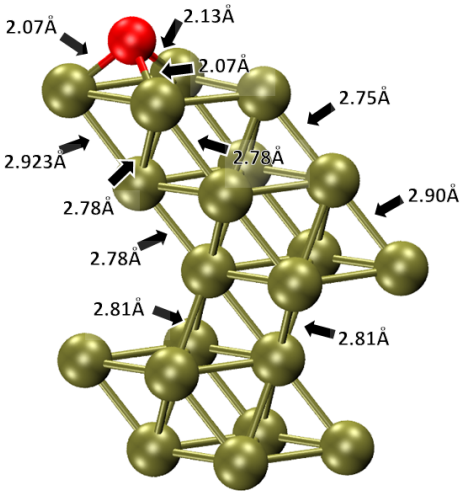

Figure 4.11: An oxygen atom chemisorbed on the HCP site on a the (111) surface of a platinum slab. The structure was determined using CASTEP.

Table 4.6: Chemisorption energy of atomic oxygen at the hollow sites on the (111) and (100) facets of a Pt_{13} nanoparticle. Calculated using equation (4.2) and results obtained from simulations in in ONETEP and CASTEP.

Program	$E_{(At.\ Oads)}(100)$ facet (eV)	$E_{(At.\ Oads)}$ (111) facet (eV)
CASTEP	-6.32	-4.56
ONETEP	-6.30	-4.60

ONETEP with the new pseudo-potentials is much improved, in terms of structure and chemisorption energies. It is likely this is because the new Rappe pseudo-potential enables a more accurate description of the system.

It was also necessary to re-run the calculations of atomic and molecular oxygen chemisorption on the (111) surface of a platinum slab. Asides from the change in the pseudopotentials, these parameters and method used in these calcualtions was identical to those specified in section 4.1. These calculations were run using the parameters specified in Table 4.3, with Pulay mixing, and the Rappe pseudo-potential. The resulting structures can be seen in Figures 4.10 and 4.11, and the chemisorption energies can be found in Table 4.7. It was interesting to

	Site	Chemisorption energy (eV)		
Pseudopotential	-	Ming-Hsien-Lee	Rappe	Difference
$E_{(At.\ Oads)}$ (eV) see eqn. (4.2)	FCC	-3.64	-5.25	-1.61
	HCP	-3.19	-4.80	-1.61
	ATOP	-2.29	-3.91	-1.62
$E_{(Mo.\ Oads)}$ (eV) see eqn. (4.1)	FCC	-0.85	-0.90	-0.05
	HCP	-0.39	-0.45	-0.06
	ATOP	0.50	0.45	-0.05
Relative chemisorption energies (eV)	HCP	0.46	0.45	-0.01
	ATOP	1.36	1.35	-0.01

Table 4.7: Comparison of computed chemisorption energies for atomic oxygen on Pt(111) obtained using two different sets of input parameters. One set used Ming-Hsien-Lee pseudo-potentials with Gaussian smearing of 0.2 eV (see Table 4.1.3). The other set used Rappe pseudo-potentials, and Fermi smearing with a smearing width of 0.1 eV. Both sets of calculations used an RPBE xc-functional and a 950 eV KE-cut-off. The chemisorption energies were calculated from the results of CASTEP calculations. The relative chemisorption energies are calculated with respect to the FCC site, and are the same for both $E_{(Mo.\ Oads)}$ and $E_{(At.\ Oads)}$. The "Difference" column contains the chemisorption energies obtained using the Rappe pseudo-potential minus those obtained using the Ming-Hsien-Lee pseudo-potential.

note that the calculated chemisorption energy is significantly greater in magnitude when using the Rappe pseudo-potential. However, given the different pseudo-potential and temperature used, as well as a different method of calculating the occupancies, some changes are expected. Significantly, the relative chemisorption energies agreed very well, showing that calculations using these two different

sets of parameters were consistent in the relative strengths of oxygen-platinum binding at different chemisorption sites. This indicates that same qualitative behaviour would be observed, regardless of which set of calculation parameters and pseudo-potential were used, e.g. in both cases, the FCC site was the most energetically favourable chemisorption, followed by the HCP and finally the ATOP site. It should be noted that the difference results obtained using the Rappe and Ming-Hsien-Lee pseudopotentials is smaller for chemisorption of molecular oxygen than it is for chemisorption of atomic oxygen. This indicates a difference in oxygen-oxygen bond strength[6] predicted by calculations using the Rappe and Ming-Hsien-Lee pseudo-potentials. Overall, agreement between the results obtained using the two pseudo-potentials was considered sufficiently good that the first stage of the calibration study, in which the basis set cut-off and xc-functional were determined, did not need to be repeated with the Rappe pseudo-potential.

4.3 Calibration Summary

Following the calibration studies it was decided that the initial parameters to be used in all future calculations of atomic and molecular oxygen chemisorption on platinum are as follows:

- Kinetic energy cut-off : 1067 eV.
- Exchange correlation functional : RPBE.
- Norm conserving pseudo-potentials generated by the Rappe group.

[6]Calculations using the two pseudo-potentials predict different values of $(E_{O_2} - 2E_O)$, where E_{O_2} is the energy of molecular oxygen, and E_O is the energy of atomic oxygen.

- NGWF radii : 9 Bohr.
- Initial PAO configuration on oxygen : “2s2, 2p4”.
- Initial PAO configuration on platinum : “5d9, 6s1|P”.
- Electronic temperature : 1160.45 K .
- The Fermi-Dirac distribution will be used to determine the occupancies of the Kohn-Sham orbitals.

4.4 Investigation of chemisorption of atomic oxygen on Pt_{13}, Pt_{55} and Pt_{147}

Following the calibration of the ONETEP input parameters, an investigation into chemisorption of atomic and molecular oxygen on larger cuboctohedrals was embarked upon. Although there is a wealth of literature concerning *ab initio* computational investigations of oxygen chemisorption on clusters of 55 atoms or less [74][75][76][77][78], only recently have computational investigations begun to probe larger sizes [52][79]. Consequently, the finite size effects relating to chemisorption of oxygen on platinum nanoparticles have not been well explored.

Chemisorption energies were calculated for chemisorption of atomic oxygen on platinum nanoparticles of Pt_{13}, Pt_{55} and Pt_{147} atoms. It was expected that the binding energy of atomic and molecular oxygen would become more positive as the clusters became larger [13], as there are fewer under-coordinated platinum atoms. For this reason it is expected that binding will be strongest at those sites

nearest the edge of a facet. How O-Pt and Pt-Pt bond lengths vary with the size of the nanoparticle was also investigated; the Pt-Pt bonds in small nanoparticles are significantly shorter than those observed in the bulk, an effect which is expected to become less apparent as the nanoparticle size increases. The charge transfer, and charge density deformation resulting from oxygen chemisorption was also investigated. Density of states (D.O.S.) and localized densities of states (L.D.O.S.) were also calculated, in order to gain insight into the energetics of those molecular orbitals which play the largest role in O-Pt bonding.

4.4.1 Calculation procedure

Unless otherwise specified, the calculations all used the procedure described in section 4.2.1, and the parameters specified in section 4.3.

The geometry optimization calculation of Pt_{55} proved difficult to converge, and a slightly non-standard optimization method had to be used. To understand the reasoning behind the tactic employed a brief discussion of geometry optimization calculations is necessary. A geometry optimization can be split into two main components; an inner loop in which a single point energy calculation is performed[7], and an outer loop in which the positions of the atoms are changed so as to minimize the net force on each atom. The forces between the atoms are determined from the outcome of the single point energy calculation in the inner loop described in [80]. Therefore, the accuracy of the single point energy calculation in the inner loop determines the accuracy of the calculation of forces between atoms[8]. If the geometry steps taken in the outer loop are to be effective, then

[7] In ONETEP, a single point energy calculation has two loops by itself, so there are three nested loops in a geometry optimization in ONETEP.

[8] The expression for the force in terms of the charge density is accurate, but if the charge density

the error in the interatomic forces must be small compared to the magnitude of these forces. In the initial stages of the geometry optimization net force on each atom is large. While this force is large, the single point energy calculations in the inner loop can be relatively inaccurate, without having a significant negative impact on the geometry optimization procedure. However, as the geometry optimization proceeds, and the net force on each atom reduces, more accurate single point energy calculations are required.

The geometry optimization calculation of Pt_{55} was set up so that the precision of the single point energy calculations increased as the geometry optimization progressed; from relatively imprecise in the initial stages, to very precise in the later ones. This was achieved by fixing the number of iterations in the inner and outer loops of the ONETEP single point energy calculation to a relatively low number, but reusing the NGWFs and Hamiltonian between geometry steps (by default, the NGWFs would be reset periodically). Taking this approach greatly reduced the computational cost of the calculations. However, even with this approach it was necessary to use a looser force convergence tolerance of $|\mathbf{F}| < 0.005$ Ha/Bohr, where $|\mathbf{F}|$ is the average value of the magnitude of the force on an atom in the system.

Problems with the geometry optimization were also encountered in calculations involving Pt_{147}. Initially, an attempt was made to optimized the positions of all the platinum atoms. However, $|\mathbf{F}|$ never converged to less than 0.03 Ha/Bohr (1.54 eV/Å), despite a very large number of iterations. This was thought to be too large for reliable structural information to be obtained. Furthermore, the value of $|\mathbf{F}|$ on the 100th geometry step was not significantly lower than the value of $|\mathbf{F}|$ on the

is inaccurate, so is the force.

1st step, which indicates that geometry optimization procedure was not resulting in a structure that was significantly more energetically favorable.

Initially, it was thought that this was the result of the geometry optimizer struggling to deal with so many degrees of freedom. Consequently, it was decided that only the 9 platinum atoms nearest the oxygen atom would be optimized, whilst the other 138 platinum atoms were held fixed. These calculations never converged, but an interesting effect was observed in the early stages of geometry optimization; the Pt-Pt bonds associated with those atoms whose positions were being optimized began to contract, both in systems with and without the chemisorbed oxygen (hence this was not a consequence of Pt-O binding). It is likely that this distortion is due to finite size effects which result in variation in the Pt-Pt bond lengths in platinum nanoparticles. The Pt_{147} nanoparticle was constructed using the Pt-Pt bond length appropriate for bulk platinum (see discussion in section 4.2.1). However, geometry optimization calculations on Pt_{13} and Pt_{55} showed significant finite size effects; the Pt-Pt bond-length was not uniform throughout the nanoparticles, and the Pt-Pt bond length differed significantly from that of bulk platinum. In the Pt_{147} nanoparticle, the positions of the majority of platinum atoms were fixed to the bulk value, so the effect of the finite size of the nanoparticle on the Pt-Pt bond length could only be observed in the small fraction of unfixed platinum atoms. The distortion made the structure slightly asymmetrical, even when the oxygen was not present. This would have a negative impact on the accuracy of the calculations, as this asymmetry is a consequence of constraints on the calculation, rather than of physical properties of the system.

It is possible that this distortion could be due to and experimental lattice parameter being used (see section 4.2.1), as opposed to one which was optimized for the

specific calculation parameters. However, the variation in the Pt-Pt bond length observed in the Pt_{55} nanoparticle (see Figure 4.16) were significantly greater than the discrepancy between the optimized and unoptimized lattice parameters. Furthermore, the effect of optimizing the lattice parameter for specific calculation parameters was usually a slight expansion, whereas the distortion described above was a contraction. Consequently, it is likely that the distortion described above would have occured even had an optimized lattice parameter been used. Nonetheless, use of a lattice parameter optimized for these specific calculation parameters may have improved the accuracy and convergence of the calculation.

Most importantly, the calculations with the majority of the Pt atoms fixed did not converge to within a reasonable tolerance within a reasonable number of iterations. Consequently, it was decided that it was best to fix the positions of all the platinum atoms, and only optimize the position of the oxygen atom. A similar approach had been adopted by Nørskov et al for calculations on similar platinum systems (see references in [13] and [79]). In the calculations described in this thesis, the Pt_{147} cuboctohedral was constructed by cutting from bulk platinum, with a lattice parameter of 3.92 Å, obtained from experimental measurements of bulk platinum at 293.15 K [58]. It was also only possible to converge the geometries to within a force tolerance of $|\mathbf{F}| < 0.005$ Ha/Bohr. Although this will have an impact on the accuracy of the computed chemisorption energies, the effect on the platinum-oxygen charge transfer and density deformation will be less pronounced, and so these calculations can still be used to gain qualitative insight into interactions of atomic oxygen with platinum nanoparticles.

4.4.2 Chemisorption energies

Tables 4.8, 4.9, and 4.10 include computed chemisorption energies and associated platinum-oxygen charge transfer for chemisorption of atomic oxygen on different sites on the the surfaces of cuboctohedrons Pt_{13}, Pt_{55}, and Pt_{147}. Figure 4.12 shows how the chemisorption energies of atomic oxygen at the HCP and FCC sites varies with the size of the nanoparticle, and compares these values for that obtained for chemisorption of atomic oxygen on a Pt(111) surface. Investigation of chemisorption of oxygen on platinum slabs had revealed that the ATOP site was unfavorable, and consequently chemisorption of atomic and molecular oxygen at this site was not investigated. The free energies used to obtain these chemisorption energies were from calculations which had been converged to within a tolerance threshold of 1.5×10^{-3} eV.

Table 4.8: Computed chemisorption energies, $E_{(At.\ Oads)}$ and $E_{(Mo.\ Oads)}$, for atomic and molecular oxygen at hollow sites on the (111) and (100) facet of a cuboctohedral Pt_{13} nanoparticle, obtained using equations (4.2) and (4.1), and results obtained from ONETEP calculations. The value for the charge transfer was obtained through Hirschfeld analysis (see equation (4.13)).

Chemisorption site	$E_{(At.\ Oads)}$ (eV)	$E_{(Mo.\ Oads)}$ (eV)	Charge transfer from Pt_{13} to O (e)
HCP (111) facet	-6.30	-1.67	-0.19
Hollow (100) facet	-4.56	-0.07	-0.17

Table 4.9: Computed chemisorption energies, $E_{(At.\ Oads)}$ and $E_{(Mo.\ Oads)}$, for atomic and molecular oxygen at hollow sites on the (111) and (100) facet of a cuboctohedral Pt_{55} nanoparticle, obtained using equations (4.2) and (4.1), and results obtained from ONETEP calculations. The value for the charge transfer was obtained through Hirschfeld analysis (see equation (4.13)).

Chemisorption site	$E_{(At.\ Oads)}$ (eV)	$E_{(Mo.\ Oads)}$(eV)	Charge transfer from Pt_{55} to O (e)
FCC (111) facet	-5.28	-0.65	-0.18
HCP (111) facet	-5.60	-0.97	—
Hollow (100) facet	-5.50	-0.88	-0.17

Table 4.10: Computed chemisorption energies, $E_{(At.\ Oads)}$ and $E_{(Mo.\ Oads)}$, for atomic and molecular oxygen at hollow sites on the (111) and (100) facet of a cuboctohedral Pt_{147} nanoparticle, obtained using equations (4.2) and (4.1), and results obtained from ONETEP calculations. The value for the charge transfer was obtained through Hirschfeld analysis (see equation (4.13)).

Chemisorption site	$E_{(At.\ Oads)}$ (eV)	$E_{(Mo.\ Oads)}$ (eV)	Charge transfer from Pt_{147} to O (e)
FCC (111) facet	-3.55	1.08	-0.22
HCP (111) facet	-4.27	0.36	-0.20
Hollow (100) facet	-4.83	-0.19	-0.18

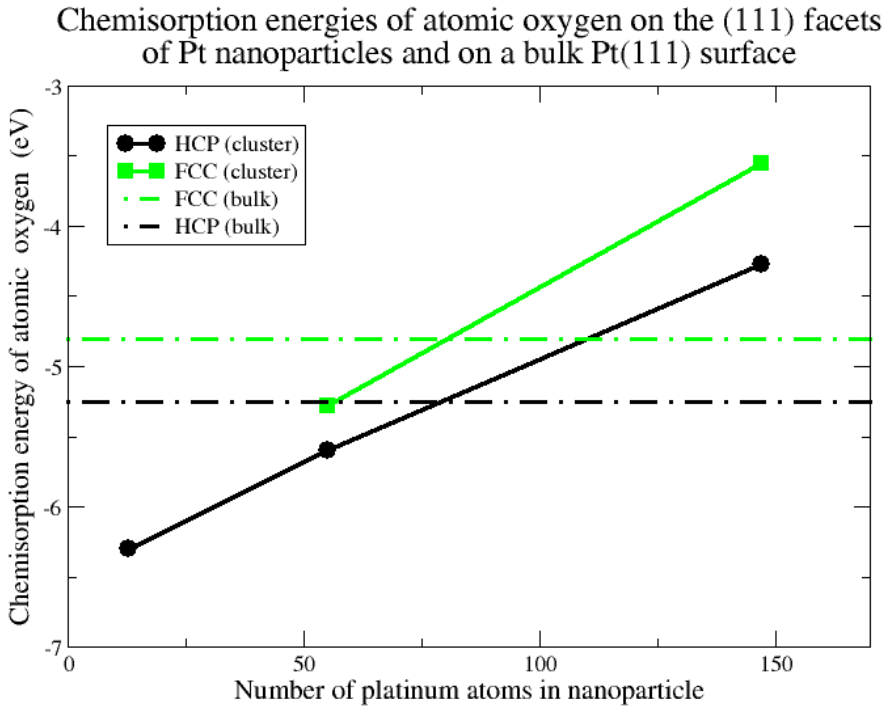

Figure 4.12: The effect of the variation in Pt nanoparticle size on the computed chemisorption energy of atomic oxygen at HCP and FCC sites, and comparison of chemisorption energy of atomic oxygen on the (111) facets of Pt nanoparticles with the chemisorption energy of atomic oxygen on a bulk Pt(111) surface. The lines with symbols upon them correspond to results for chemisorption on nanoparticles (data from tables 4.8, 4.9 and 4.10), whilst the dashed horizontal lines correspond to results for chemisorption on the bulk surface (data from Table 4.7).

.

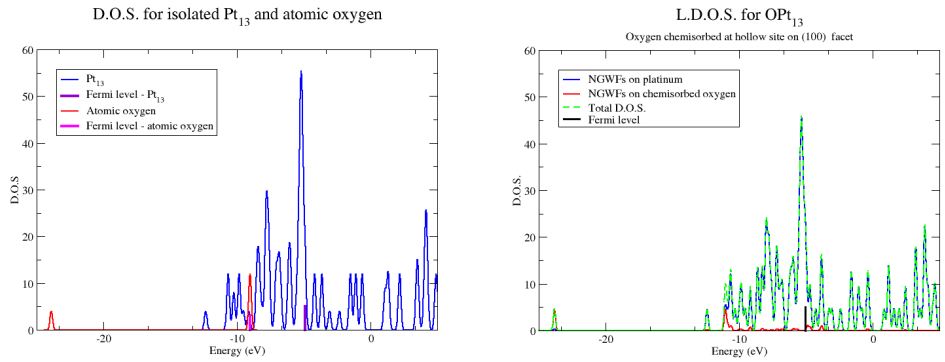

Figure 4.13: The densities of states for an isolated Pt_{13} nanoparticle and isolated oxygen atom (left), and the localized density of states for the oxygen atom and Pt_{13} nanoparticle when the oxygen atom is chemisorbed on the hollow site on the (100) facet of the Pt_{13} nanoparticle.

4.4.3 Densities of states

Densities of states (D.O.S.) and localized densities of states (L.D.O.S.) were also calculated. The L.D.O.S. are calculated by projecting the Kohn-Sham orbitals onto those NGWFs centred on a given atom (or set of atoms), and then calculating the D.O.S. from these projected orbitals. Comparison between the D.O.S of the isolated receptor and ligand, with their L.D.O.S. when they are bound together, provides insight as to how the electronic structure of the two components is affected by binding.

4.4.4 Optimized geometries

The following diagrams show structures of the nanoparticles with bond lengths obtained through geometry optimizations performed in ONETEP. It should be noted that only the position of the oxygen was optimized in the calculations performed on Pt_{147}. Therefore, the values of the Pt-O bond lengths are not expected

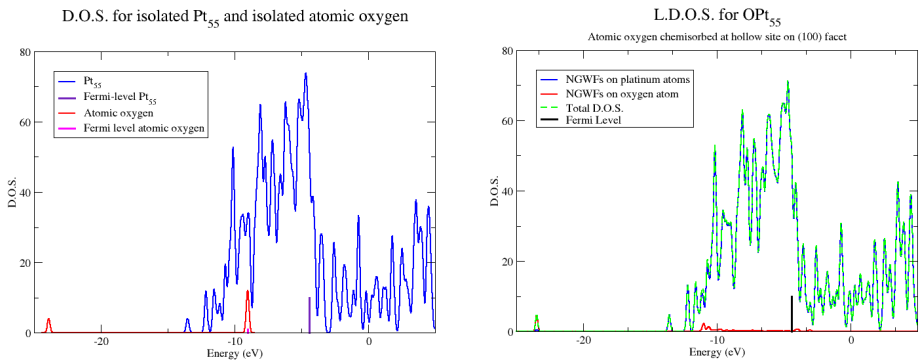

Figure 4.14: The densities of states for an isolated Pt_{55} nanoparticle and isolated oxygen atom (left), and the localized density of states for the oxygen atom and Pt_{55} nanoparticle when the oxygen atom is chemisorbed on the hollow site on the (100) facet of the Pt_{13} nanoparticle.

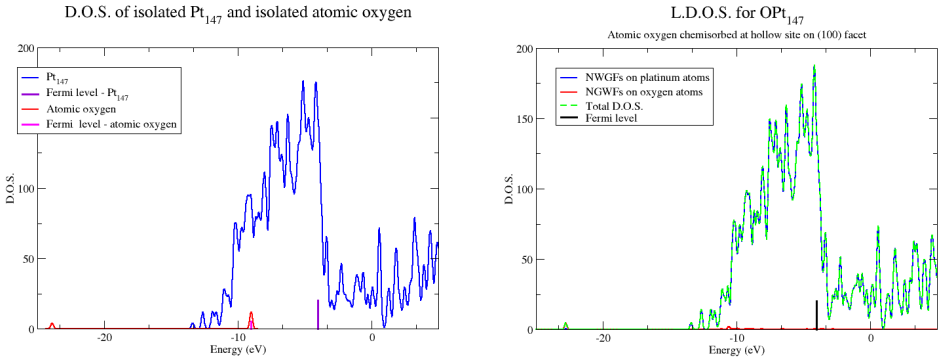

Figure 4.15: The densities of states for an isolated Pt_{147} nanoparticle and isolated Oxygen atom (left), and the localized density of states for the oxygen atom and Pt_{147} nanoparticle when the oxygen atom is chemisorbed on the hollow site on the (100) facet of the Pt_{13} nanoparticle.

to be accurate, as no distortion of the nanoparticle surface was possible.

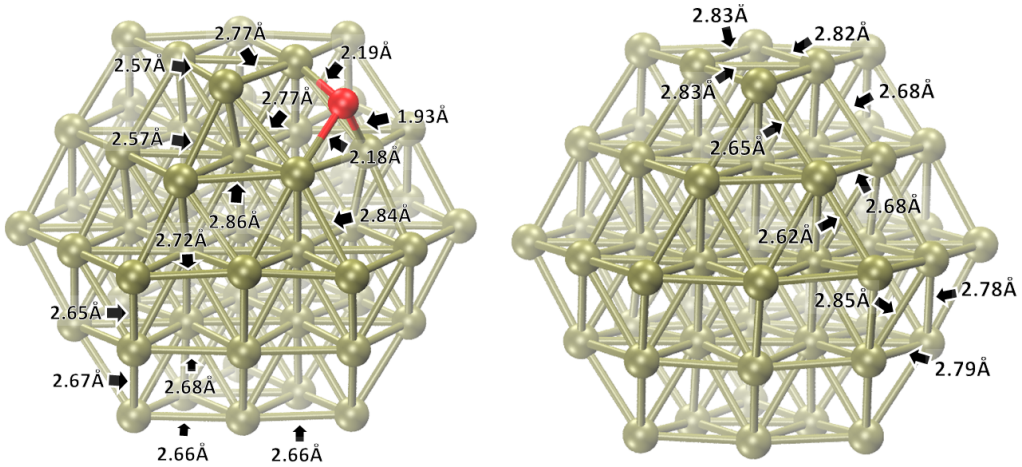

Figure 4.16: Optimized structures of a bare Pt_{55} nanoparticle (left), and a Pt_{55} nanoparticle (green) with oxygen (red) chemisorbed at the hollow site on the (100) facet. These geometries were obtained using ONETEP

.

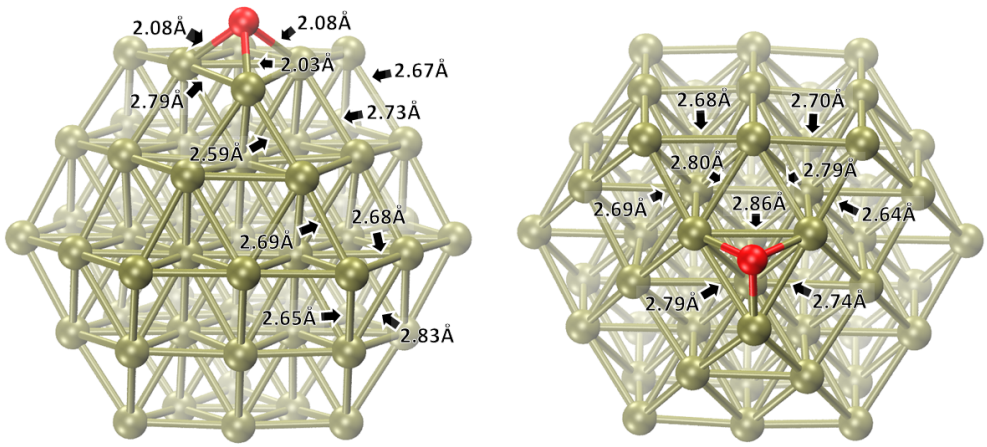

Figure 4.17: Optimized structure of a Pt_{55} nanoparticle (green) with oxygen (red) chemisorbed at the HCP site on the (111) facet. This geometry was obtained using ONETEP

.

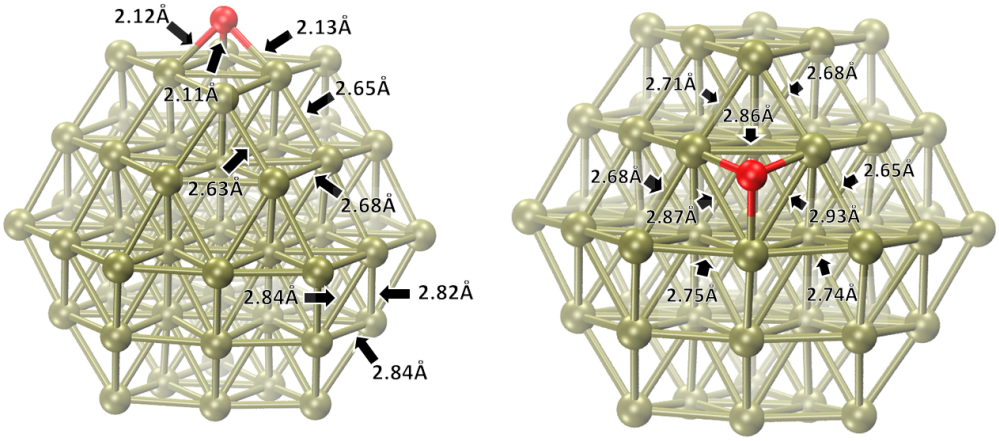

Figure 4.18: Optimized structure of a Pt_{55} nanoparticle (green) with oxygen (red) chemisorbed at the FCC site on the (111) facet. This geometry was obtained using ONETEP.

.

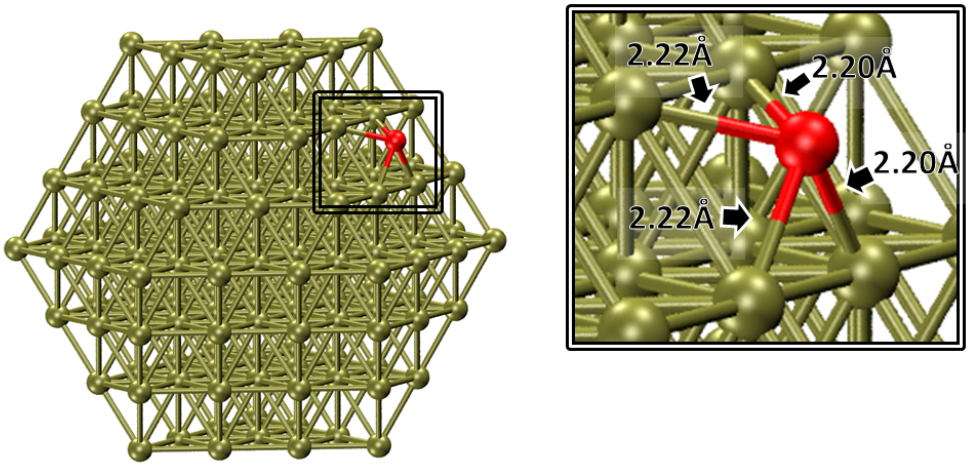

Figure 4.19: A Pt_{147} nanoparticle (green) with oxygen (red) chemisorbed at the hollow site on the (100) facet. Only the position of the oxygen was optimized. This geometry was obtained using ONETEP.

.

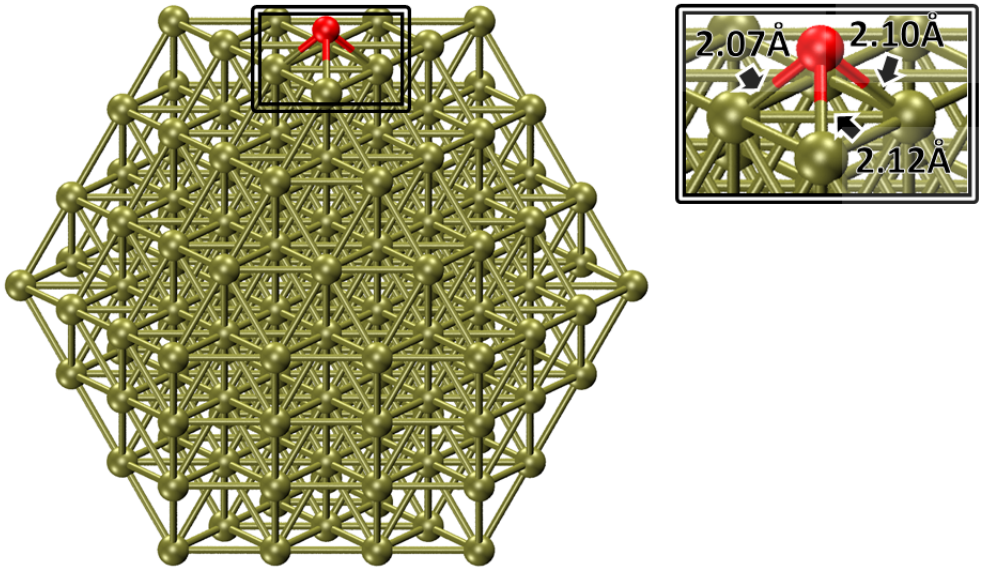

Figure 4.20: A Pt_{147} nanoparticle (green) with oxygen (red) chemisorbed at the HCP site on the (111) facet. Only the position of the oxygen was optimized. This geometry was obtained using ONETEP.

.

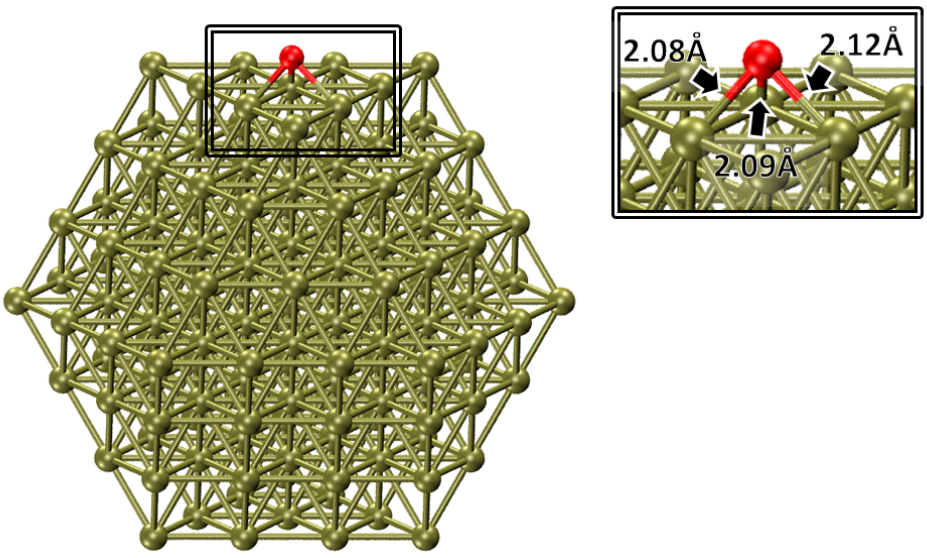

Figure 4.21: A Pt_{147} nanoparticle (green) with oxygen (red) chemisorbed at the FCC site on the (111) facet. Only the position of the oxygen was optimized. This geometry was obtained using ONETEP.

.

4.4.5 Hirschfeld density analysis

Hirschfeld density analysis [81] is a technique used to gain qualitative insight into the transfer of charge density associated with the formation of chemical bonds. All values for charge transfer presented so far in this report were obtained through use of Hirschfeld analysis.

Analysis of a simple system, composed of a ligand bound to receptor, requires three electron densities:

- The isolated ligand, $L_{isolated}(\boldsymbol{r})$.
- The isolated receptor $R_{isolated}(\boldsymbol{r})$.
- The complex, $C(\boldsymbol{r})$.

In most cases, the most energetically favourable geometry for the ligand when it is bound in the complex will be different to the most energetically favourable geometry for the ligand when it is not in the complex. The density of the isolated ligand, $L_{isolated}(\boldsymbol{r})$, is calculated using the geometry the ligand has when it is bound in the complex[9]. Similarly, the density of the isolated receptor is calculated for the geometry the receptor has when it is bound in the complex. This is necessary, as it is important that the geometry of the components of the system are kept consistent if the charge decomposition is to be calculated correctly. The first step is to calculate the electron density of the promolecule, $P(\boldsymbol{r})$:

$$P(\boldsymbol{r}_i) = R_{isolated}(\boldsymbol{r}_i) + L_{isolated}(\boldsymbol{r}_i) \; . \tag{4.5}$$

Here $\boldsymbol{r}_i$ is a point on the real space grid on which the charge density is represented.

[9]The geometry of the isolated ligand is obtained by taking the optimized geometry of the complex, and deleting all atoms not in the ligand.

The electron density of the promolecule is the superposition of the densities of the unbound components of the system. It is the density of a system where the ligand and receptor are in same geometry as when they are bound together in the complex, but do not interact at all, i.e. it is the overlap of the sum of the densities of the isolated components, $L_{isolated}(\boldsymbol{r})$ and $R_{isolated}(\boldsymbol{r})$ of the system.

The deformation density of the entire system, $C_{Deform}(\boldsymbol{r}_i)$, is given by:

$$C_{Deform}(\boldsymbol{r}_i) = C(\boldsymbol{r}_i) - P(\boldsymbol{r}_i) \; . \tag{4.6}$$

This is the difference between the density of the system where the ligand and receptor interact, and the density of the system where they do not.

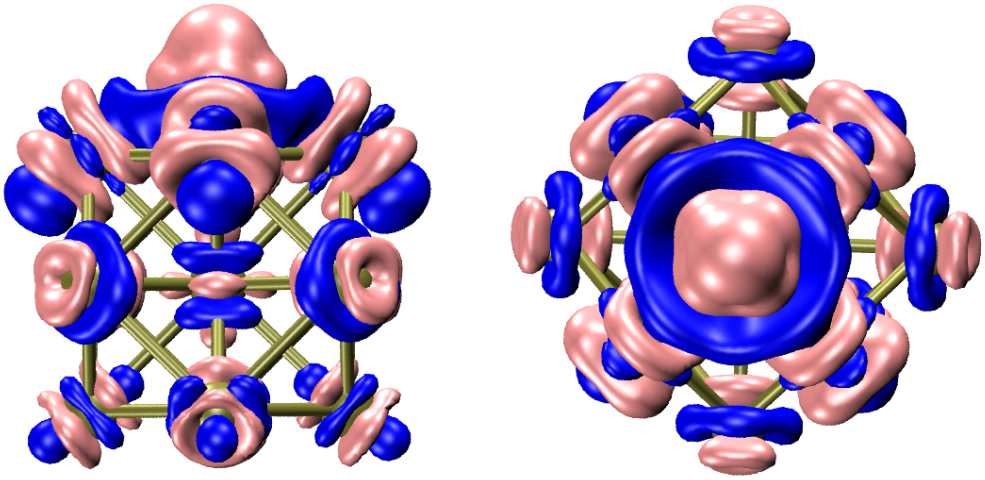

Figure 4.22: Deformation density for an oxygen atom chemisorbed at the hollow site on the (100) facet of a Pt_{13} nanoparticle. The value on the pink and blue isosurfaces are +0.02 and -0.02 electrons per $Å^3$ respectively.

.

To gain more insight into the binding it is useful to calculate the Hirschfeld deformation densities of individual components. From the promolecule density the

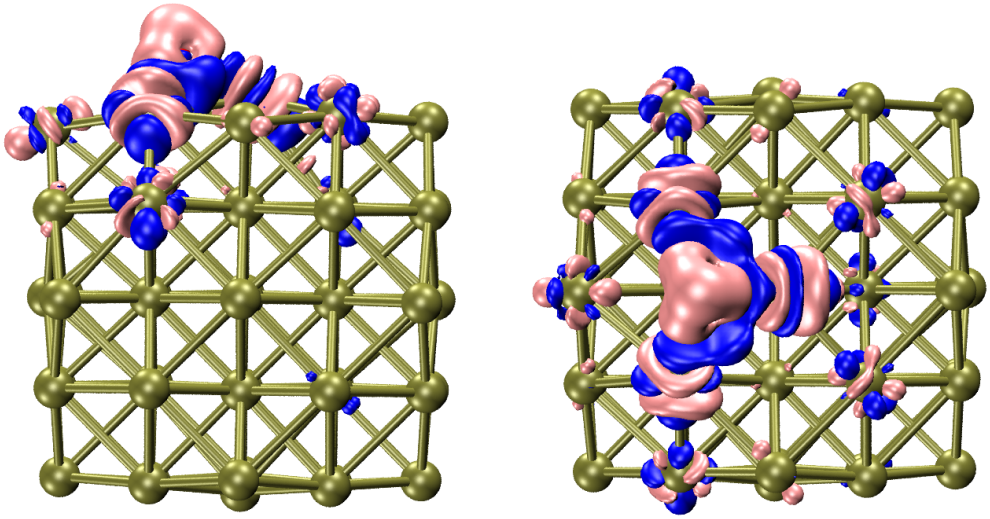

Figure 4.23: Deformation density for an oxygen atom chemisorbed at the hollow site on the (100) facet of a Pt_{55} nanoparticle. The value on the pink and blue isosurfaces are +0.02 and -0.02 electrons per $Å^3$ respectively.

.

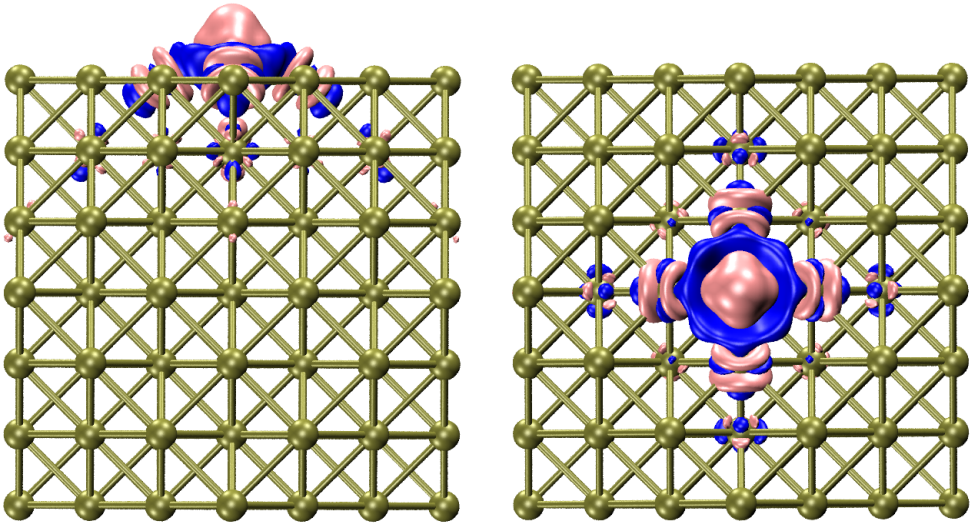

Figure 4.24: Deformation density for an oxygen atom chemisorbed at the hollow site on the (100) facet of a Pt_{147} nanoparticle. The value on the pink and blue isosurfaces are +0.02 and -0.02 electrons per $Å^3$ respectively.

.

following weighting is calculated:

$$L_{weight}(\boldsymbol{r}_i) = \frac{L_{isolated}(\boldsymbol{r}_i)}{P(\boldsymbol{r}_i)} \ , \tag{4.7}$$

$$R_{weight}(\boldsymbol{r}_i) = \frac{R_{isolated}(\boldsymbol{r}_i)}{P(\boldsymbol{r}_i)} \ . \tag{4.8}$$

These weightings determine what fraction of the density at a given point in space should be associated to the ligand, $L_{weight}(\boldsymbol{r}_i)$, and to the receptor, $R_{weight}(\boldsymbol{r}_i)$.

These weightings are then used to calculate the Hirschfeld densities of the receptor, $R_{Hirschfeld}(\boldsymbol{r})$, and ligand, $L_{Hirschfeld}(\boldsymbol{r})$:

$$L_{Hirschfeld}(\boldsymbol{r}_i) = L_{weight}(\boldsymbol{r}_i)C(\boldsymbol{r}_i) \ , \tag{4.9}$$

$$R_{Hirschfeld}(\boldsymbol{r}_i) = R_{weight}(\boldsymbol{r}_i)C(\boldsymbol{r}_i) \ . \tag{4.10}$$

The Hirschfeld density of the ligand $L_{Hirschfeld}(\boldsymbol{r}_i)$ is the electron density associated with the ligand when it is in the complex. This assumes that how the density at a given point in space is distributed between the receptor and ligand does not change when the two bind together, even though the total density does.

The Hirschfeld density can be used to calculated the Hirschfeld deformation density for the ligand $L_{HD}(\boldsymbol{r})$ and receptor $R_{HD}(\boldsymbol{r})$.

$$L_{HD}(\boldsymbol{r}_i) = L_{Hirschfeld}(\boldsymbol{r}_i) - L_{isolated}(\boldsymbol{r}_i) \tag{4.11}$$

$$R_{HD}(\boldsymbol{r}_i) = R_{Hirschfeld}(\boldsymbol{r}_i) - R_{isolated}(\boldsymbol{r}_i) \tag{4.12}$$

The Hirschfeld deformation densities show how the amount of electronic density associated with the ligand and receptor changes when the two are bound together in the complex. A qualitative idea of the charge transfer, δQ, can be obtained by integrating the Hirschfeld deformation density associated with a component over the simulation cell. For example, the charge transferred from the receptor to the

ligand, $\delta Q_{receptor}$, is given by

$$\delta Q_{receptor} = \sum_{i}^{N_{grid}} w R_{HD}(\boldsymbol{r}_i), \tag{4.13}$$

where N_{grid} is the number of points on the grid upon which the density is represented, and w is the weighting of each grid point (typically defined as $w = \frac{V}{N_{grid}}$, where V is the volume of the simulation cell). The values of the charge transfer seen in the tables included earlier in this report were all obtained using this method.

The deformation density is useful for investigating charge screening. Examination of the extent of density deformation associated with chemisorption of an oxygen atom can provide an indication of how the electronic structure of the platinum nanoparticle is altered following chemisorption, and how the reactivity may decrease as successive oxygen atoms are chemisorbed.

In Figures 4.22, 4.23 and 4.24, the extensive deformation to the electron density is consistent with formation of a chemical bond. It should be noted that the deformation to the density is not limited to those platinum atoms with which the oxygen atom is directly bonded, suggesting the electronic structure of the entire cluster plays a role in bonding.

Chapter 5

Discussion

The most significant finding of this study is that the energy of atomic oxygen chemisorption decreases as the size of the nanoparticle increases. This agrees well with a similar computational study carried out by Li et al [79], who investigated the chemisorption energy of atomic oxygen on cuboctohedral platinum nanoparticles using DFT calculations performed using the GPAW [82] software package. It also agrees well with conclusions from experimental investigations. For example, in reference [83] X-ray photoelectron spectroscopy (XPS) was used to determine the core-binding energies of platinum atoms in various sizes of nanoparticle, and from this data, conclusions about relative strengths of O-Pt binding to these nanoparticles was drawn. The conclusion drawn in this thesis and in the two aforementioned studies is consistent with the hypothesis that small nanoparticles make poor catalysts due to overly strong binding between the platinum nanoparticle and the intermediates in the ORR [12].

The chemisorption energies of atomic oxygen obtained in this study agree, for the most part, to within 1 eV with those obtained in the computational DFT studies

included in references [79] and [84]. The latter of these studies utilized VASP [85], a plane-wave DFT code. This level of consistency between studies is reasonable given the size of the disagreement relative to the size of the chemisorption energies ($\sim$-4.5eV), the agreement in the relative chemisorption energies at different sites, and the fact that in neither study were the positions of the platinum atoms optimized. Chemisorption of atomic oxygen at the hollow sites on both the (100) and (111) facets was found to be energetically favoured. This is consistent with numerous experimental studies, such as that described in reference [86], in which a rotating disk electrode technique is used to study the catalytic activity of different platinum surfaces.

For the most part it has not been possible to directly compare numerical results obtained in this study with those found in the literature. One reason for this is the lack of precise quantitative calculations which have been performed previously on systems of this size. Another reason is that in those studies which do exist, there is significant variation in the techniques used (e.g. the method of calculating the occupancies [77], and whether the platinum structure is optimized [79]), the conditions of the system (e.g. the temperature [79]), and whether a support is used (e.g. graphene supports are often included [87]). However, good qualitative agreement with existing studies is achieved, and the chemisorption energies of atomic oxygen calculated in this study fall within the range of values ($\sim$1-6eV) reported in the literature[1].

An unexpected finding was that the chemisorption energies for molecular oxygen on the (111) facet of the Pt_{147} nanoparticle were positive. A positive chemisorption energy indicates that chemisorption of molecular oxygen on the hollow sites

[1]This is still a very large range, but acceptable given the aforementioned variations in the calculations.

of the (111) facet is not energetically favoured, and that this facet of the Pt nanoparticle would only play a limited role in the first step of the ORR described in equation (1.4). However, this conclusion is contrary to much evidence in the literature. For example, it would disagree with the experimental study described in reference [88], in which the activity of different surfaces is investigated using the rotating ring disk electrode (RRDE) technique. It also disagrees with results from computational investigations, such as those described in reference [89], which was performed using DFT software packages Gaussian 98 [90] and VASP. An explanation for this disagreement is that strength of the oxygen binding to the Pt_{147} is probably underestimated by the calculations described in this thesis, as the position of the Pt-atoms in the OPt_{147} complex were not optimized. Consequently, the Pt-atoms are unable to move into the positions most energetically favoured for Pt-O binding. Therefore, the final geometry of the OPt_{147} complex will not be the most energetically favoured, resulting a more positive energy for the complex, and a more positive chemisorption energy.

It was observed that the most favoured site for chemisorption of atomic or molecular oxygen varied with the size of the nanoparticle. The HCP site was the most favoured site on Pt_{13} and Pt_{55}, whilst the hollow site on the (100) facet was the most favoured site on Pt_{147}. It is interesting to note that the chemisorption energy at the HCP site was consistently more negative (and hence more favoured energetically) than the FCC site. This is consistent with results of a similar computational DFT study performed by Han et al [84]. This is in disagreement with results for bulk slab systems obtained in the calibration study in this thesis (see Table 4.1). It also disagrees with other computational DFT studies, such as that described in reference [62], and experimental studies, such as that described in reference [63], in which the oxygen-platinum binding was investigated using temperature

programmed desorption. The HCP site may be energetically favoured be due to edge effects. If a site is on the edge of a facet, then the Pt-atoms at that site will be under-coordinated. Therefore, the oxygen atom will bind more strongly at this site. On Pt_{55} and Pt_{147}, the HCP site at which the oxygen was chemisorbed is on the edge of the (111) facet, and consequently binding to this site is very strong. Conversely, for both Pt_{55} and Pt_{147}, the FCC site investigated is near or at the centre of the (111) facet, so the binding of oxygen to this site is comparatively weak. This strong binding to under-coordinated sites is commented upon in experimental studies, e.g. in reference [91] the electronic structure of platinum nanoparticles is investigated using XPS. Similar findings of numerous other experimental studies are discussed in the review in reference [92]. These findings are corroborated by computational studies of oxygen chemisorption on platinum included in reference [93], which make use of computational implementations of DFT.

The geometry optimization calculations revealed that the cuboctohedral Pt_{13} and Pt_{55} nanoparticles cut directly from the bulk were not the most energetically favoured. In the unoptimized structure of Pt_{13} and Pt_{55} every Pt-Pt bond was 2.77 Å, but the structures of both Pt_{13} and Pt_{55} changed significantly following geometry optimization. The bond lengths in Pt_{13} all contract by nearly 0.1Å. However, the overall structure remains very nearly symmetrical.

The optimized structure of the Pt_{55} exhibits both contraction and expansion of Pt-Pt bonds from their bulk value of 2.77 Å; the (111) facets bulge outwards slightly and have longer Pt-Pt bond lengths of $\sim$2.85 Å. Meanwhile, the (100) facets appear to remain flat and contract slightly, having Pt-Pt bond lengths of $\sim$2.68 Å. Contraction of the interlayer separation in metals slabs whose surfaces resemble the (100) and (111) planes is well known [94]. The contraction and expansion ob-

served in nanoparticle structures following optimization was significantly greater than similar effects observed in the optimized geometries of the bare Pt (111) slabs (for which the magnitude of the change in bond lengths was $<$0.05 Å). A possible reason that the effects are more pronounced in nanoparticles is that a greater fraction of the atoms are at edge and surface sites, and hence relatively unconstrained (42 of the atoms in Pt_{55} are on the surface of the nanoparticle). Huang et al have commented upon a similar effect observed in electron diffraction experiments on gold clusters [95], where bonds below both the (111) and (100) facets contract, but those bonds associated with the (100) facet contract much more than those below the (111) facet. It is possible that for Pt_{55}, the large contraction ($\sim$0.13 Å) of the bonds on the (100) facet causes a slight expansion ($\sim$0.06 Å) of those bonds associated with the (111) facet, in order to stabilize the structure. It is also interesting to note that in Figure 4.16, the Pt-Pt bond lengths on similar (111) facets are not identical. Breaking the symmetry of an octahedral structure can lower the energy (the Jahn-Teller effect [19]), but without more extensive investigation it is not possible to be certain that this is the effect responsible.

There was deformation of the structure of the Pt_{55} nanoparticle following oxygen chemisorption. Bonds between Pt-atoms at the chemisorption site tended to expand, whilst the Pt-Pt bonds between atoms adjacent to the chemisorption site tended to contract. This can be seen by comparing the optimized structure of the bare nanoparticle, Pt_{55}, shown in Figure 4.16, with the optimized structures of OPt_{55}, depicted in Figures 4.16, 4.17 and 4.18. The structural deformation was limited to those few atoms in the immediate vicinity (nearest and next nearest neighbours) of the chemisorbed oxygen atom, and inspection of Figures 4.16, 4.17 and 4.18 reveals that there was little to no change in the Pt-Pt bond lengths on the nanoparticle facets not adjacent to the facet upon which the oxygen atom

was chemisorbed. Even in the immediate vicinity of the chemisorbed oxygen, the expansion or contraction in the Pt-Pt bonds rarely exceeded 0.1 Å. It is hard to precisely determine the impact this will have had on chemisorption energies, but a recent study [96] of oxygen chemisorption using plane-wave DFT code VASP indicate that relaxation of the nanoparticle structure can alter the chemisorption energy of atomic oxygen by as much as 30%. Consequently, the chemisorption energies of atomic oxygen obtained for the Pt_{147} nanoparticles may be inaccurate, as the geometry of Pt_{147} was not optimized in the work included in this thesis. Experimental evidence suggests that the dissolution of platinum nanoparticles into the solvent during can take place, affecting their stability as catalysts [91]. Therefore, investigation of the structural stability of platinum nanoparticles is important, as nanoparticles with less stable structures are more likely to dissolve.

It is interesting to note that the deformation of the structure of the Pt(111) slab following chemisorption of atomic oxygen was greater than that observed in the platinum nanoparticles[2]. This is probably a consequence of two things; 1) the constraints on the structure of the slab 2) the oxygen coverage was comparatively high; one oxygen atom for every 4 surface platinum atoms. At high coverages lateral interactions [97] [98] between chemisorbed oxygen atoms become important, and can have a significant impact on how the platinum surface deforms. These lateral interactions can also affect the energies of chemisorption at different sites. Furthermore, in the calibration study on platinum slabs the Pt:O ratio was 20:1, as opposed to 55:1 as in the case of OPt_{55}. It is also noticeable that the Pt-Pt bonds in the slab expand following chemisorption of the oxygen atom. However, unlike in the nanoparticles, no other Pt-Pt bonds appear to contract to compensate. This is

[2]This is surprising, as the relaxation seen in the *bare* nanoparticles was much greater than that seen in the *bare* slabs.

likely due to the structural stability afforded by the periodic nature of the slab, and the fact that the positions of atoms in the bottom two layers of the slab were held fixed during geometry optimization. It could also be related to the constraints on the slab geometry imposed by the fixed size of the simulation cell, which makes expansion of the slab in the direction normal to the surface possible, but prevents expansion and contraction in directions tangential to the surface.

The formation of bonds is indicated both by the distances between the platinum and oxygen atoms, and by the deformation to the density that can be seen in Figures 4.22, 4.23 and 4.24. With a few exceptions, the lengths of the Pt-O bonds are largely independent of nanoparticle size, and generally vary by less than 0.05 Å. The Pt-O bond lengths found in the calculations of chemisorption of atomic oxygen on a Pt(111) slab are also very similar in size to those seen in nanoparticles ($\sim$ 2.1 Å). It is interesting to note that simulations of atomic oxygen chemisorbed on the (100) facet of the Pt_{13} and Pt_{147} nanoparticles predict formation of four Pt-O bonds of similar length ($\sim$2.2 Å). However, the simulation of atomic oxygen chemisorbed on the Pt_{55} indicated that only 3 Pt-O bonds are formed, and that one of these bonds was significantly shorter than the others (the bond lengths are 2.18 Å, 2.19 Å and 1.93 Å). Furthermore, the shortest of these bonds is between the oxygen atom and the well co-ordinated platinum atom at the centre of the (100) facet, whilst the oxygen atom does not bond at all with the relatively under co-ordinated platinum atom on the vertex of the nanoparticle (see Figures 4.18 and 4.23).

The deformation densities depicted in Figures 4.22, 4.23 and 4.24 provide an indication of the fraction of the nanoparticle with which the oxygen atom interacts most strongly. If the density deformation within a given region is small,

then it suggests that the charge density in that region is relatively unaffected by chemisorption of the oxygen, and does not significantly influence the bonding of the oxygen to the surface[3]. This is consistent with the isosurfaces depicted in Figures 4.22, 4.23 and 4.24, which show that the most extensive deformation is along the Pt-O bonds. Furthermore, it was noted that the shape of the density deformation in the Pt-O bond region resembles an isosurface of the probability densities of atomic orbitals associated with large principal quantum numbers n, i.e. the shape of the density deformation seems to resemble those atomic orbitals thought to be most involved in Pt-O bonding.

The deformation to the charge density resulting from chemisorption of oxygen on Pt_{147} is reasonably well localized within the region surrounding the chemisorption site. Furthermore, the deformation to the density on the far side of the Pt_{147} nanoparticle, opposite to the chemisorption site, is roughly 20 times smaller than that observed at the site (i.e. an isovalue of ~ 0.001 must be used for the plot in order to see a similarly extensive isosurface). This suggests that larger nanoparticles might not yield significantly different values for the chemisorption of a single atomic oxygen atom, which would be consistent with the findings of Li et al [79]. However, such predictions should be made very tentatively, as the nature of O-Pt bonding has many complexities not revealed by the density deformation. Nonetheless, given the extent of the deformation to the density, chemisorption of one oxygen on Pt_{147} could be expected to affect the binding of the nanoparticle to any futher oxygen atoms, even if these oxygen atoms were to be chemisorbed on opposite facets.

[3]It should be noted that this is a very qualitative measure, and that there will be some slight deformation to the density at all points in the system, and that all parts of the system will play some role in the chemisorption process.

The deformation to the charge density resulting from chemisorption of atomic oxygen at the FCC site on the (111) facet of Pt_{147} extended further through the nanoparticle than it did when the atomic oxygen was chemisorbed in the hollow site of the (100) facet (see Figure 4.24). However, the oxygen bound significantly less strongly to the (111) facet (see Table 4.10), and despite the greater spatial extent of the deformation, there was not a notable increase in the charge transfer between the oxygen and platinum. This suggests that when atomic oxygen is chemisorbed on the (111) facet, it interacts more weakly with the orbitals associated with individual Pt atoms, but with a greater number of them.

An unexpected feature of the results is lack of correlation between the amount of charge transferred and the chemisorption energy. It is clear from Tables 4.8, 4.9 and 4.10 that there is not a link between the magnitude of the platinum-oxygen charge transfer and the chemisorption energy (as might have been expected). However, given that the platinum-oxygen charge transfer does not vary significantly with chemisorption site, and the qualitative nature of Hirschfeld analysis, this lack of correlation does not indicate significant inaccuracy in the results.

The total D.O.S. of the isolated Pt_{147} and OPt_{147} complex are very similar (see Figure 4.15); there is no noticeable shift in the Fermi-level, and the states surrounding the Fermi-level are largely unchanged. One noticeable difference is the presence of a peak at around -23 eV, which is present in all D.O.S. plots of the isolated oxygen atom, as well as the L.D.O.S. plots of the OPt_N complexes (Figures 4.13, 4.14 and 4.15). This is almost certainly associated with the 2s orbitals on the oxygen atom. These states are not expected to play a significant role in bonding [93], and so are present both when the oxygen is isolated, and when it is in the complex. The same cannot be said of the higher energy peak found in the

D.O.S. for the isolated oxygen. This peak is probably associated with the 2p orbitals of the oxygen atom. In the OPt_N complex, this peak is effectively replaced by a low flat smear. Initially it was thought that this was due to difficulties in reading relatively small contribution of the oxygen to the L.D.O.S.. Consequently, L.D.O.S. were calculated for just the chemisorbed oxygen atom, and the three platinum atoms to which it was bonded. However, even with focusing only on the D.O.S. associated with these atoms, no clear bonding orbitals were observed. This suggests that there are not a few specific molecular orbitals which correspond to the Pt-O bonds, but rather the p-orbitals have interacted and combined with a large number of molecular orbitals which are delocalized about the entire OPt_N complex. This is consistent with plots of probability densities associated with several of the molecular orbitals near the Fermi-level. These plots showed molecular orbitals delocalized about the entire platinum cluster. It was noted that the plots of the HOMO (highest occupied molecular orbital) and LUMO (lowest unoccupied molecular orbital) for the OPt_{147} complexes clearly resemble a plot of several d-orbitals centred on different atoms in the nanoparticle. This is interesting considering that molecular orbitals within the d-band are known to play important an important role in Pt-O bonding [93].

In ONETEP it is possible to analyze the angular momentum character of the optimized NGWFs, i.e. see to what extent the NGWFs on a given atom resemble s, p, d and f orbitals. This is determined from the projection of an NGWF into a set of spherical waves which have the desired angular momentum character. The NGWFs are initialized as pseudo-atomic orbitals with a given angular momentum, but are optimized during the calculation, and may change substantially. Preliminary calculations were performed in which the NGWFs were not optimized. These calculations were slow to converge, and yielded results which seemed unphysical;

the Pt-Pt bonds expanded to $\sim$3.5Å (an expansion of $\sim$0.8Å). Therefore, optimization of the NGWFs is necessary if the system is to be well described, and it is interesting to investigate the effect of this optimization. A brief investigation revealed that most of the NGWFs did not change substantially following optimization; with the exception of those NGWFs centred on platinum atoms bound directly to the oxygen, the angular momentum character of the NGWFs changed by $<1\%$ over the course of the calculations on OPt_{55} and OPt_{147}. However, the change was more pronounced in those NGWFs centred on the platinum atoms with which the oxygen atom was bound. Following optimization, these NGWFs exhibited a slight shift of 2-3% towards higher angular momentum, i.e. an NGWF which was initialiazed as a d-orbital, became marginally more f-like in character following optimization.

Chapter 6

Conclusions

The work reported in this dissertation shows that it is possible to use ONETEP to perform simulations of oxygen atoms chemisorbed on platinum cuboctohedrals, Pt_N, in the range N=13-147. It was observed that the magnitude of the chemisorption energy of atomic oxygen decreases with increasing sizes of nanoparticle. There are two probable causes of this 1) Variation in the electronic structure with the size of the platinum nanoparticle 2) The platinum atoms in small nanoparticles are less well coordinated, and atomic oxygen binds more tightly to less well coordinated atoms. To determine the relative significance of these factors, it could be useful to investigate how the proximity of a chemisorption site to the edge of the nanoparticle facet affects the chemisorption energy at that site. It may also prove useful to investigate binding to other, typically less stable sites, such as the top and bridge sites. Given the importance of deformation of the platinum nanoparticles in determining the chemisorption energy of atomic oxygen, any extensive investigation into the chemisorption energy of oxygen at different sites should make use of full geometry optimization calculations.

That oxygen binds more strongly to smaller nanoparticles could be a reason why they are generally less effective as catalysts. The second stage of the ORR is the formation of OH, which occurs when a hydrogen atom binds to the chemisorbed oxygen atom. Therefore, if the oxygen is bound strongly to the platinum surface, it is likely the hydroxyl molecule will also bind strongly [99]. If the hydroxyl molecule is too strongly bound to the platinum surface, then the final stage of the ORR, during which the hydroxyl molecule combines with another hydrogen atom to form water and leave the platinum surface[1], may occur infrequently, or not happen at all. Therefore, excessively strong O-Pt binding can indicate that the nanoparticle would make a poor catalyst.

It is difficult to determine the relationship between the chemisorption energy of atomic oxygen and the chemisorption energy of OH without performing calculations on $OHPt_N$ complexes. One possible future direction of research, would be to investigate chemisorption of OH, and other possible intermediates of the ORR, on the surface of the platinum nanoparticle. This could provide an insight into how the chemisorption energy of OH is related to the chemisorption energy of atomic oxygen, as well as how this relationship varies with increasing nanoparticle size.

It was observed that the proximity of a chemisorption site to the edge of a facet affected the chemisorption energy of atomic oxygen at that site. It is thought that the low coordination number of platinum atoms at such sites, as well as the associated ability of the platinum atoms to move so as to accommodate the chemisorbed

[1] i.e. The transition from $OHPt_N + H^+ + e^- \rightarrow H_2O + Pt_N$

oxygen, are the main causes of this effect. Nanoparticles with stepped facets (and hence a large number of potential chemisorption sites involving under-coordinated platinum atoms, to which atomic oxygen will bind strongly) could be investigated. Such systems have already been prepared and investigated in experimental studies, such as that described in reference [100], in which a rotating disk electrode technique is used to discover that the activity of platinum concave nanocubes compares favourably with the activity of platinum cuboctohedrals. That platinum nanoparticles with stepped facets are effective catalysts seems to run contrary to the earlier hypothesis that it was the overbinding of atomic oxygen to small platinum nanoparticles which caused small nanoparticles to be inefficient catalysts. It is possible that the geometry of stepped facets (i.e. the positions of chemisorption sites relative to one another) makes them particularly well suited for the formation of the other intermediates in the ORR (e.g. OH and H_2O), and the dissociation of molecular oxygen. Further investigation of such surfaces could be interesting in determining what physical properties of these surfaces make them so effective.

The optimized structures of the platinum cuboctohedrals differed significantly from those structures cut directly from bulk. Significant deformation of the nanoparticle following chemisorption of atomic oxygen was also observed. Extensive deformation following chemisorption of atomic oxygen indicates that chemisorption of oxygen into the subsurface of the nanoparticle may be possible. Subsurface chemisorption of oxygen is known to reduce the catalytic activity of a platinum slab [101], and it alters both the geometry and electronic structure of the platinum slab. These effects will likely be more pronounced in smaller systems, where a relatively high fraction of the atoms are near the surface. An investigation as to the impact of subsurface chemisorption of oxygen in platinum nanoparticles, and

how this affects the electronic structure and the stability of different facets, could prove useful.

In this work, it was found that chemisorption of atomic oxygen to Pt_{13}, Pt_{55} and Pt_{147} changed the electron density. The deformation to the density was greatest in the region immediately surrounding the chemisorption site. However, even for the large Pt_{147} nanoparticle, slight deformation to the density occurred on all facets, including facets far from that upon which the oxygen atom was chemisorbed. This suggests that chemisorption of an oxygen atom on one facet would have an effect on the chemisorption of second oxygen atom, regardless of which facet this oxygen atom was chemisorbed upon. One possible avenue of investigation would be to see if there is any correlation between the chemisorption energy of atomic oxygen at higher coverages, and the overlap in the deformation densities associated with these individual oxygen atoms.

Plots of the L.D.O.S. indicated that the 2s orbitals on oxygen did not play a major role in Pt-O bonding, but that the 2p orbitals do. The differences between the D.O.S. of Pt_{55} and OPt_{55}, and between the D.O.S. of Pt_{147} and OPt_{147}, were relatively minor. This indicates that chemisorption of a single oxygen atom did not significantly change the overall electronic structure of these nanoparticles. However, it is clear from the deformation densities plotted in Figures 4.21, 4.22 and 4.23, that the electronic structure in the vicinity of the chemisorption site was seriously affected. Furthermore, Hansen et al have used calculations with the plane-wave DFT code Dacapo [102] to show that chemisorption of multiples oxygen atoms can actually improve the reactivity of a platinum surface [103]. One way of

gaining more insight into how the chemisorption of oxygen affects the electronic structure of the platinum nanoparticle would be to calculate the L.D.O.S. associated with platinum atoms at unoccupied chemisorption sites in the vicinity of the site at which the oxygen is chemisorbed.

It would be particularly interesting to investigate the angular momentum projected density of states (P.D.O.S.). This is the density of states calculated from the KS-orbitals projected onto a set of functions of a certain angular momentum type. For example, the P.D.O.S. of the d-band could be calculated by first projecting the KS-orbitals onto all the atomic orbitals in the system with an angular momentum quantum number of 2 (the d-orbitals). The D.O.S. calculated from these projected KS-orbitals is the projected density of states (P.D.O.S.) for the d-band. The proximity of the centre of the d-band (i.e. population weighted average energy of states in the d-band) to the Fermi level, has been shown to correlate with the catalytic activity of a nanoparticle [104]. This is because the d-band centre provides an indication of the energies of the bonding and anti-bonding orbitals associated with Pt-O bonding [93].

It would also be useful to investigate the dissociation of O_2 molecules into two separate oxygen atoms, each of which is bound to a separate site on the platinum surface. It is important that the oxygen molecule dissociates into two separate oxygen atoms, as this reduces the probability that H_2O_2 will form[2]. It is shown in reference [99] that the requirement for the oxygen molecule to dissociate, is important in determining which sites are best for chemisorption of molecular oxy-

[2]Hydrogen peroxide is known to have a detrimental effect on the functioning of PEMFCs [10].

gen. Furthermore, the two dissociated oxygen atoms will likely be in close proximity to one another, and this can have a significant effect on the chemisorption energy. Therefore, in order to accurately determine which sites are most desirable for increasing the activity of platinum nanoparticle catalysts, it may be necessary to simulate chemisorption and dissociation of complete oxygen molecules.

Higher coverages of atomic and molecular oxygen, as well as higher coverages of other intermediates of the ORR, could also be investigated. Oxygen coverages of a quarter monolayer and a half monolayer are similar to those found in PEMFCs. The lateral interactions between different species which occur at such coverages may affect which sites are most favorable for different stages of the ORR [97] [98]. Increased coverages could also have an effect on the stability of the surfaces of the platinum nanoparticles, and also may serve to stabilize oxygen atoms chemisorbed at sites which would otherwise be unstable.

The impact that variations in the electronic temperature have on calculations should also be investigated. All the calculations in this report were carried out at an electronic temperature of over 1000 K, which is significantly higher than standard PEMFC operating temperatures of $\sim$300-350 K [10]. This high temperature was used as it eased convergence of the calculations. A brief investigation in this work was performed (consisting only of a calculation on Pt_{13} at 116.4 K), and suggested that the change in temperature had little impact on the chemisorption energies or geometries. Furthermore, other computational DFT studies make use of similarly high temperatures [79]. However, a more thorough investigation of the effect of high electronic temperatures may be prudent before more extensive studies in-

volving other aspects of the ORR are embarked upon.

The support upon which the platinum nanoparticles are secured can have an impact on their reactivity. Computational DFT has been used to investigate the chemisorption of atomic and molecular oxygen on small nanoparticles ($<$14 platinum atoms) on different carbon supports [5][87]. However, larger nanoparticles, of the sizes most commonly used in fuel cells, have yet to be investigated. In PEMFCs, the electrodes are typically immersed in a solvent, and this has also been shown to have an impact on the catalytic activity of platinum catalysts [105] [106]. Therefore, investigation of the effect of different solvents could be useful in development of more efficient fuel cell catalysts. This could be achieved through use computational methods, such as the implicit solvent model implemented in ONETEP [107].

Bibliography

[1] C.-K. Skylaris, P.D. Haynes, A.A. Mostofi, and M.C. Payne. Introducing ONETEP: Linear-scaling density functional simulations on parallel computers. *J. Chem. Phys.*, 122:0841119–0841129, 2005.

[2] S. J. Clark, M. D. Segall, C. J. Pickard, P. J. Hasnip, M. I. J. Probert, K. Refson, and M. C. Payne. First principles methods using CASTEP. *Zeitschrift für Kristallographie*, 220(5-6):567–570, 2005.

[3] P. W. Atkins and J. de Paula. *Atkins' Physical Chemistry*, volume 8. Oxford University Press, Oxford, 2006.

[4] S. Litster and G. McLean. P. E. M. fuel cell electrodes. *Journal of Power Sources*, 130(1):61–76, 2004.

[5] E. Antolini. Carbon supports for low-temperature fuel cell catalysts. *Applied Catalysis B: Environmental*, 88(1):1–24, 2009.

[6] S. Gamburzev and A. J. Appleby. Recent progress in performance improvement of the proton exchange membrane fuel cell. *Journal of Power Sources*, 107(1):5–12, 2002.

[7] DuPont. *Teflon P.T.F.E. fluoropolymer resin properties handbook*, volume 1. DuPont, 2012.

[8] J. Zhang. *PEM fuel cell electrocatalysts and catalyst layers: fundamentals and applications*, pages 89–128. Springer, 2008.

[9] L. Carrette, K. A. Friedrich, and U. Stimming. Fuel cells–fundamentals and applications. *Fuel cells*, 1(1):5–39, 2001.

[10] V. S. Bagotsky. *Fuel cells: Problems and solutions*, pages 45–59. Wiley, Pennington, New Jersey, 3rd edition, 2009.

[11] J. K. Nørskov, J. Rossmeisl, A. Logadottir, L. Lindqvist, J. R. Kitchin, T. Bligaard, and H. Jonsson. Origin of the overpotential for oxygen reduction at a fuel-cell cathode. *The Journal of Physical Chemistry B*, 108(46):17886–17892, 2004.

[12] I. E. L. Stephens, A. S. Bondarenko, U. Grønbjerg, J. Rossmeisl, and I. Chorkendorff. Understanding the electrocatalysis of oxygen reduction on platinum and its alloys. *Energy & Environmental Science*, 5(5):6744–6762, 2012.

[13] J. Kleis, J. Greeley, N. Romero, V. Morozov, H. Falsig, A. Larsen, J. Lu, J. Mortensen, M. Dułak, K. Thygesen, J. Nørskov, and K. Jacobsen. Finite size effects in chemical bonding: From small clusters to solids. *Catalysis Letters*, 141:1067–1071, 2011.

[14] Y. Ding, N. Tian, Z. Zhou, S. Sun, and Z. L. Wang. Synthesis of tetrahexahedral platinum nanocrystals with high-index facets and high electro-oxidation activity. *Science*, 316(5825):732–735, 2007.

[15] F. Baletto and R. Ferrando. Structural properties of nanoclusters: Energetic, thermodynamic, and kinetic effects. *Reviews of Modern Physics*, 77(1):371–423, 2005.

[16] P. Valentini, T. E. Schwartzentruber, and I. Cozmuta. ReaxFF grand canonical Monte Carlo simulation of adsorption and dissociation of oxygen on platinum (111). *Surface Science*, 605(23):1941–1950, 2011.

[17] C. J. Cramer. *Essentials of Computational Chemistry*. Wiley, 2nd edition, 2006.

[18] S. Gasiorowicz. *Quantum Physics*. Wiley, 3rd edition, 2003.

[19] P. W. Atkins and R. S. Friedman. *Molecular quantum mechanics*. Oxford University Press, Oxford, 3rd edition, 1997.

[20] F. Mandl. *Quantum Mechanics*. Wiley, London, 1st edition, 1991.

[21] J. M. Ziman. *Principles of the Theory of Solids*. Cambridge University Press, Cambridge, 2nd edition, 1979.

[22] R. G. Parr and W. Yang. *Density-Functional Theory of Atoms and Molecules*, volume 16 of *International Series of Monographs on Chemistry*. Oxford University Press, Oxford, 1989.

[23] A. A. Mostofi. *On Linear-Scaling Methods for Quantum Mechanical First-Principles Calculations*. PhD thesis, University of Cambridge, 2003.

[24] W. Kohn and L. J. Sham. Self-consistent equations including exchange and correlation effects. *Phys. Rev.*, 140(4A):A1133–A1138.

[25] N. D. Mermin. Thermal properties of the inhomogeneous electron gas. *Phys. Rev.*, 137(5A):A1441–A1443, 1965.

[26] I. N. Levine. *Quantum chemistry*. Prentice Hall, Upper Saddle River, NJ, 5th edition, 2000.

[27] P. A. M. Dirac. Note on exchange phenomena in the Thomas atom. In *Proceedings of the Cambridge Philosophical Society*, volume 26, page 376, 1930.

[28] J. P. Perdew and A. Zunger. Self-interaction correction to density-functional approximations for many-electron systems. *Phys. Rev. B*, 23:5048–5079, 1981.

[29] S. H. Vosko, L. Wilk, and M. Nusair. Accurate spin-dependent electron liquid correlation energies for local spin density calculations: a critical analysis. *Canadian Journal of Physics*, 58:1200–1211, 1980.

[30] J. P. Perdew and Y. Wang. Accurate and simple analytic representation of the electron-gas correlation energy. *Phys. Rev. B*, 45:13244–13249, 1992.

[31] L. A. Cole and J. P. Perdew. Calculated electron affinities of the elements. *Phys. Rev. A*, 25:1265–1271, 1982.

[32] G. D. Barrera, D. Colognesi, P. C. H. Mitchell, and A. J. Ramirez-Cuesta. LDA or GGA? A combined experimental inelastic neutron scattering and ab initio lattice dynamics study of alkali metal hydrides. *Chemical physics*, 317(2):119–129, 2005.

[33] P. Ziesche and H. Eschrig. *Electronic structure of solids '91: proceedings of the 75. WE-Heraeus-Seminar and 21st Annual International Symposium on Electronic Structure of Solids*. Akademie Verlag, 1st edition, 1991.

[34] B. Hammer, L. B. Hansen, and J. K. Nørskov. Improved adsorption energetics within density-functional theory using revised Perdew-Burke-Ernzerhof functionals. *Phys. Rev. B*, 59:7413–7421, 1999.

[35] J. P. Perdew, K. Burke, and M. Ernzerhof. Generalized gradient approximation made simple. *Phys. Rev. Lett.*, 77:3865–3868, 1996.

[36] C. Lee, W. Yang, and R. G. Parr. Development of the Colle-Salvetti correlation-energy formula into a functional of the electron density. *Phys. Rev. B*, 37:785–789, 1988.

[37] Y. Zhao and D. G. Truhlar. The M06 suite of density functionals for main group thermochemistry, thermochemical kinetics, noncovalent interactions, excited states, and transition elements: two new functionals and systematic testing of four M06-class functionals and 12 other functionals. *Theo. Chem. Acc.*, 120(1-3):215–241, 2008.

[38] Y. Zhao and D. G. Truhlar. Density functional for spectroscopy: No long-range self-interaction error, good performance for Rydberg and charge-transfer states, and better performance on average than B3LYP for ground states. *J.Phys. Chem. A*, 110(49):13126–13130, 2006.

[39] E. H. Lieb and S. Oxford. Improved lower bound on the indirect Coulomb energy. *International Journal of Quantum Chemistry*, 19(3):427–439, 1981.

[40] F. Bloch. Über die Quantenmechanik der Elektronen in Kristallgittern. *Zeitschrift fur Physik*, 52:555–600, 1929.

[41] M. C. Payne, M. P. Teter, D. C. Allan, T. A. Arias, and J. D. Joannopoulos. Iterative minimization techniques for abinitio total-energy calculations: molecular-dynamics and conjugate gradients. *Rev. Mod. Phys.*, 64(4):1045–1097, 1992.

[42] R. M. Martin. *Electronic Structure*. Cambridge University Press, Cambridge, 1st edition, 2004.

[43] N. Troullier and J. L. Martins. Efficient pseudopotentials for plane-wave calculations. *Physical Review B*, 43(3):1993–2006, 1991.

[44] D. Vanderbilt. Soft self-consistent pseudopotentials in a generalized eigenvalue formalism. *Phys. Rev. B*, 41:7892–7895, 1990.

[45] L. Kleinman and D. M. Bylander. Efficacious form for model pseudopotentials. *Phys. Rev. Lett.*, 48:1425–1428, 1982.

[46] C.-K. Skylaris, A. A. Mostofi, P. D. Haynes, O. Dieguez, and M. C. Payne. Nonorthogonal generalized Wannier function pseudopotential plane-wave method. *Phys. Rev. B.*, 66(3):035119–035131, 2002.

[47] C.-K. Skylaris, P. D. Haynes, A. A. Mostofi, and M. C. Payne. Implementation of linear-scaling plane wave density functional theory on parallel computers. *Phys. Status Solidi B-Basic Solid State Physics*, 243(5):973–988, 2006.

[48] E. Prodan and W. Kohn. Nearsightedness of electronic matter. *Proc. Natl. Acad. Sci. USA*, 102(33):11635–11638, 2005.

[49] M. Valiev, E. J. Bylaska, N. Govind, K. Kowalski, T. P. Straatsma, H. J. J. Van Dam, D. Wang, J. Nieplocha, E. Apra, T. L. Windus, and W. A. de Jong. NWChem: A comprehensive and scalable open-source solution for large scale molecular simulations. *Computer Physics Communications*, 181(9):1477–1489, 2010.

[50] E. Anglada, J. M. Soler, J. Junquera, and E. Artacho. Systematic generation

of finite-range atomic basis sets for linear-scaling calculations. *Phys. Rev. B*, 66:205101–205105, 2002.

[51] N. M. D. Hine, M. Robinson, P. D. Haynes, C. K. Skylaris, M. C. Payne, and A. A. Mostofi. Accurate ionic forces and geometry optimisation in linear scaling density-functional theory with local orbitals. *Phys. Rev. B*, 83(19):195102–195112, 2010.

[52] A. H. Larsen. *Efficient electronic structure methods applied to electronic nanoparticles*. PhD thesis, Aarhus University, 2010.

[53] P. Pulay. Improved SCF convergence acceleration. *Journal of Computational Chemistry*, 3(4):556–560, 1982.

[54] N. Marzari, D. Vanderbilt, and M. C. Payne. Ensemble density-functional theory for ab initio molecular dynamics of metals and finite-temperature insulators. *Phys. Rev. Lett.*, 79(7):1337–1340, 1997.

[55] I. Grinberg, N. J. Ramer, and A. M. Rappe. Transferable relativistic Dirac-Slater pseudopotentials. *Phys. Rev. B*, 62:2311–2314, 2000.

[56] N. D. Mermin and N. W. Ashcroft. *Solid State Physics*. Saunders College, Philadelphia, 1st edition, 1976.

[57] T. E. Schwartzentruber P. Valentini and I. Cozmuta. Molecular dynamics simulation of O_2 sticking on Pt(111) using the ab initio based ReaxFF reactive force field. *The Journal of Chemical Physics*, 133(8):084703–084712, 2010.

[58] J. W. Arblaster. Crystallographic properties of platinum. *Platinum Metals Review*, 1(41):12–21, 1997.

[59] G. Kresse and J. Furthmüller. Efficient iterative schemes for ab initio total-energy calculations using a plane-wave basis set. *Physical Review B*, 54(16):11169–11186, 1996.

[60] P. Pulay. Convergence acceleration of iterative sequences - the case of SCF iteration. *Chem. Phys. Lett.*, 73(2):393–398, 1980.

[61] H. J. Monkhorst and J. D. Pack. Special points for Brillouin-zone integrations. *Phys. Rev. B*, 13(12):5188–5192, 1976.

[62] R. B. Getman, Y. Xu, and W. F. Schneider. Thermodynamics of environment-dependent oxygen chemisorption on Pt(111). *The Journal of Physical Chemistry C*, 112(26):9559–9572, 2008.

[63] J. F. Weaver, J.-J. Chen, and A. L. Gerrard. Oxidation of Pt (111) by gas-phase oxygen atoms. *Surface Science*, 592(1):83–103, 2005.

[64] Y. H. Fang and Z. P. Liu. Surface phase diagram and oxygen coupling kinetics on flat and stepped Pt surfaces under electrochemical potentials. *The Journal of Physical Chemistry C*, 113(22):9765–9772, 2009.

[65] J. M. Soler, E. Artacho, J. D. Gale, A. Garcia, J. Junquera, P. Ordejon, and D. Sanchez-Portal. The SIESTA method for ab initio order-N materials simulation. *J. Phys. Condens. Matter*, 14(11):2745–2779, 2002.

[66] A. Ruiz-Serrano, N. D. M. Hine, and C.-K. Skylaris. Pulay forces from localized orbitals optimized in situ using a psinc basis set. *The Journal of Chemical Physics*, 136(23):234101–234110, 2012.

[67] S. García-Gil, A. García, N. Lorente, and P. Ordejón. Optimal strictly localized basis sets for noble metal surfaces. *Phys. Rev. B*, 79:075441–075450,

2009.

[68] L. E. Ratcliff, Nicholas D. M. Hine, and P. D. Haynes. Calculating optical absorption spectra for large systems using linear-scaling density functional theory. *Phys. Rev. B*, 84:165131–165141, 2011.

[69] I. T. Todorov, W. Smith, K. Trachenko, and M. T. Dove. DL_POLY_3: new dimensions in molecular dynamics simulations via massive parallelism. *J. Mater. Chem.*, 16:1911–1918, 2006.

[70] A. A. Mostofi, P. D. Haynes, C.-K. Skylaris, and M. C. Payne. Preconditioned iterative minimization for linear-scaling electronic structure calculations. *The Journal of Chemical Physics*, 119:8842–8849, 2003.

[71] http://www.sas.upenn.edu/rappegroup/research/psp/pbegga/pt.html.

[72] http://opium.sourceforge.net/.

[73] W. A. Al-Saidi, E. J. Walter, and A. M. Rappe. Optimized norm-conserving Hartree-Fock pseudopotentials for plane-wave calculations. *Phys. Rev. B*, 77:075112–075122, 2008.

[74] E. Aprà and A. Fortunelli. Density-functional study of Pt13 and Pt55 cuboctahedral clusters. *Journal of Molecular Structure: TheoChem*, 501–502(0):251–259, 2000.

[75] W.-X. Xu, K. D. Schierbaum, and W. Goepel. Ab initio study of electronic structures of Ptn clusters (n = 2–12). *International Journal of Quantum Chemistry*, 62(4):427–436, 1997.

[76] W. Q. Tian, M. Ge, B. R. Sahu, D. Wang, T. Yamada, and S. Mashiko. Geometrical and electronic structure of the Pt7 cluster: A density functional

study. *The Journal of Physical Chemistry A*, 108(17):3806–3812, 2004.

[77] T. Jacob, R. P. Muller, and W. A. Goddard. Chemisorption of atomic oxygen on Pt(111) from DFT studies of Pt-clusters. *The Journal of Physical Chemistry B*, 107(35):9465–9476, 2003.

[78] E. Aprà and A. Fortunelli. Density-functional calculations on platinum nanoclusters: Pt13, Pt38, and Pt55. *The Journal of Physical Chemistry A*, 107(16):2934–2942, 2003.

[79] L. Li, A. H. Larsen, N. A. Romero, V. Morozov, C. Glinsvad, F. Abild-Pedersen, J. P. Greeley, K. W. Jacobsen, and J. K. Norskov. Investigation of catalytic finite-size-effects of platinum metal clusters. *The Journal of Physical Chemistry Letters*, 4(1):222–226, 2012.

[80] B. G. Pfrommer, M. Cote', S. G. Louie, and M. L. Cohen. Relaxation of crystals with the quasi-newton method. *Journal of Computational Physics*, 131(1):233–240, 1997.

[81] F. L. Hirshfeld. Bonded-atom fragments for describing molecular charge densities. *Theoretica Chimica Acta*, 44(2):129–138, 1977.

[82] J. Enkovaara, C. Rostgaard, J. J. Mortensen, J. Chen, M. Dułak, L. Ferrighi, J. Gavnholt, C. Glinsvad, V. Haikola, H. A. Hansen, et al. Electronic structure calculations with GPAW: a real-space implementation of the projector augmented-wave method. *Journal of Physics: Condensed Matter*, 22(25):253202–253226, 2010.

[83] Y. Takasu, N. Ohashi, X.-G. Zhang, Y. Murakami, H. Minagawa, S. Sato, and K. Yahikozawa. Size effects of platinum particles on the electroreduction of oxygen. *Electrochimica Acta*, 41(16):2595–2600, 1996.

[84] B. C. Han, C. R. Miranda, and G. Ceder. Effect of particle size and surface structure on adsorption of O and OH on platinum nanoparticles: A first-principles study. *Phys. Rev. B*, 77(7):75410–75410, 2008.

[85] G. Sun, J. Kurti, P. Rajczy, M. Kertesz, J. Hafner, and G. Kresse. Performance of the Vienna ab initio simulation package (VASP) in chemical applications. *Journal of Molecular Structure: THEOCHEM*, 624:37–45, 2003.

[86] C. Wang, H. Daimon, T. Onodera, T. Koda, and S. Sun. A general approach to the size-and shape-controlled synthesis of platinum nanoparticles and their catalytic reduction of oxygen. *Angewandte Chemie International Edition*, 47(19):3588–3591, 2008.

[87] D.-H. Lim and J. Wilcox. Mechanisms of the oxygen reduction reaction on defective graphene-supported Pt nanoparticles from first-principles. *The Journal of Physical Chemistry C*, 116(5):3653–3660, 2012.

[88] N. Markovic, H. Gasteiger, and P. N. Ross. Kinetics of oxygen reduction on Pt(hkl) electrodes: implications for the crystallite size effect with supported Pt electrocatalysts. *Journal of the Electrochemical Society*, 144(5):1591–1597, 1997.

[89] A. Panchenko, M. T. M. Koper, T. E. Shubina, S. J. Mitchell, and E. Roduner. Ab initio calculations of intermediates of oxygen reduction on low-index platinum surfaces. *Journal of the Electrochemical Society*, 151(12):2016–2027, 2004.

[90] M. J. Frisch and G. W. Trucks et al. *Gaussian 98*. Gaussian Inc., Pittsburgh, PA, 1998.

[91] W. Sheng, S. Chen, E. Vescovo, and Y. Shao-Horn. Size influence on the oxygen reduction reaction activity and instability of supported Pt nanoparticles. *Journal of The Electrochemical Society*, 159(2):B96–B103, 2011.

[92] M. T. M. Koper. Structure sensitivity and nanoscale effects in electrocatalysis. *Nanoscale*, 3(5):2054–2073, 2011.

[93] B. Hammer and J.K. Norskov. Theoretical surface science and catalysis-calculations and concepts. *Advances in catalysis*, 45:71–129, 2000.

[94] R. P. Gupta. Lattice relaxation at a metal surface. *Phys. Rev. B*, 23:6265–6270, 1981.

[95] W. J. Huang, R. Sun, J. Tao, L. D. Menard, R. G. Nuzzo, and J. M. Zuo. Coordination-dependent surface atomic contraction in nanocrystals revealed by coherent diffraction. *Nature materials*, 7(4):308–313, 2008.

[96] C.-Y. Lu and G. Henkelman. Role of geometric relaxation in oxygen binding to metal nanoparticles. *The Journal of Physical Chemistry Letters*, 2(11):1237–1240, 2011.

[97] H. Tang, A. Van Der Ven, and B. L. Trout. Lateral interactions between oxygen atoms adsorbed on platinum (111) by first principles. *Molecular Physics*, 102(3):273–279, 2004.

[98] P. Legare. Interaction of oxygen with the Pt (111) surface in wide conditions range. A DFT-based thermodynamical simulation. *Surface Science*, 580(1):137–144, 2005.

[99] H. Tang, A. Van der Ven, and B. L. Trout. Phase diagram of oxygen adsorbed on platinum (111) by first-principles investigation. *Phys. Rev. B*,

70(4):045420–045430, 2004.

[100] T. Yu, D. Y. Kim, H. Zhang, and Y. Xia. Platinum concave nanocubes with high-index facets and their enhanced activity for oxygen reduction reaction. *Angewandte Chemie International Edition*, 50(12):2773–2777, 2011.

[101] Z. Gu and P. B. Balbuena. Absorption of atomic oxygen into subsurfaces of Pt(100) and Pt(111): Density functional theory study. *The Journal of Physical Chemistry C*, 111(27):9877–9883, 2007.

[102] https://wiki.fysik.dtu.dk/dacapo.

[103] H. A. Hansen, J. Rossmeisl, and J. K. Nørskov. Surface Pourbaix diagrams and oxygen reduction activity of Pt, Ag and Ni (111) surfaces studied by DFT. *Physical Chemistry Chemical Physics*, 10(25):3722–3730, 2008.

[104] E. Toyoda, R. Jinnouchi, T. Hatanaka, Y. Morimoto, K. Mitsuhara, A. Visikovskiy, and Y. Kido. The d-band structure of Pt nanoclusters correlated with the catalytic activity for an oxygen reduction reaction. *The Journal of Physical Chemistry C*, 115(43):21236–21240, 2011.

[105] Y. Sha. *The mechanisms of the fuel cell oxygen reduction reaction on Pt and other 8–11 column metal surfaces*. PhD thesis, California Institute of Technology, 2011.

[106] Y. Sha, T. H. Yu, Y. Liu, B. V. Merinov, and W. A. Goddard III. Theoretical study of solvent effects on the platinum-catalyzed oxygen reduction reaction. *The Journal of Physical Chemistry Letters*, 1(5):856–861, 2010.

[107] J. Dziedzic, H. H. Helal, C.-K. Skylaris, A. A. Mostofi, and M. C. Payne. Minimal parameter implicit solvent model for ab initio electronic-structure

calculations. *EPL (Europhysics Letters)*, 95(4):43001–43007, 2011.